UNIVERSIDAD DE CHILE
FACULTAD DE CIENCIAS FÍSICAS Y MATEMÁTICAS
DEPARTAMENTO DE FÍSICA

STATISTICAL PROPERTIES OF A NON-POLARIZED ACTIVE TISSUE

TESIS PARA OPTAR AL GRADO DE
DOCTORA EN CIENCIAS, MENCIÓN FÍSICA

FERNANDA LAURA PÉREZ VERDUGO

PROFESOR GUÍA:
RODRIGO SOTO BERTRAN

MIEMBROS DE LA COMISIÓN:
MIGUEL CONCHA NORDEMANN
JACQUES DUMAIS
CLAUDIO FALCÓN BEAS
SILKE HENKES
JEAN-FRANÇOIS JOANNY

SANTIAGO DE CHILE
2021

RESUMEN DE LA MEMORIA PARA OPTAR
AL TÍTULO DE DOCTORA EN CIENCIAS, MENCIÓN FÍSICA
POR: FERNANDA LAURA PÉREZ VERDUGO
FECHA: 2021
PROF. GUÍA: RODRIGO SOTO BERTRAN

STATISTICAL PROPERTIES OF A NON-POLARIZED ACTIVE TISSUE

Esta tesis tiene como objetivo desarrollar un marco teórico para analizar las propiedades de tejido epiteliales, entendiéndolos como un ejemplo de materia activa. Comprender su comportamiento mecánico es de interés para biólogos, físicos, y otros. Varios trabajos han explotado la idea de actividad polarizada incorporando fuerzas internas que producen, por ejemplo, migración celular. Aquí, en cambio, utilizamos un sistema no polarizado, donde la dirección de los movimientos está dada por las interacciones entre los elementos, y donde se consideran nuevos términos escalares de actividad.

Utilizando el modelo de vértices, encontramos analíticamente inestabilidades caracterizadas por el acoplamiento de ciertos modos de deformación cuando incorporamos homogéneamente esfuerzos sobre el tejido, o actividad celular. Mostramos un excelente acuerdo con simulaciones numéricas donde la no convexidad celular es un representante geométrico de las inestabilidades. Cuando la actividad está localizada en una sola célula del sistema, imitando las contracciones apicales que se observan en distintos procesos biológicos, se observan distintas respuestas geométricas dependiendo de la zona celular que es activa: si es la zona medial, la célula activa toma forma anisotrópica, mientras que si es el perímetro entonces tiende a tomar una forma isotrópica. Aplicamos este análisis al estudio de pulsos de contracción apicales observados experimentalmente durante eventos de división celular frustrados en etapas tempranas del desarrollo del pez anual *Austrolebias nigripinnis*. A partir de un proceso de optimización de observables geométricos, somos capaces de discriminar el tipo de actividad que mejor describe la evolución del sistema, además de obtener el mejor ajuste de los parámetros del modelo, tanto globales como particulares de cada evento activo.

Para comparar entre micro y macro-escala, describimos un modelo continuo documentado en la literatura que nace a partir del modelo de vértices, obteniendo así un tensor de esfuerzos continuo. Incorporamos actividad celular tanto medial como perimetral en una zona activa definida por una función Gaussiana, y estudiamos los estados de equilibrio mecánico y la dinámica del sistema, mediante el modelo continuo y simulaciones numéricas del modelo de vértices. Evidenciamos excelentes acuerdos entre ambas descripciones al considerar reescalamientos de las escalas temporales y de la contractilidad activa perimetral.

Para analizar la auto-organización, realizamos simulaciones numéricas de un tejido no polarizado fluctuante, donde la actividad está inspirada en la continua regeneración del citoesqueleto. Calculamos diversos factores de estructura estáticos, encontrando una separación de escalas que permite discernir entre la escala microscópica y la macroscópica del modelo. Además, la respuesta muestra ondas de compresión en el régimen de gran longitud de onda y la aparición de una cascada de energía inversa.

Al final de la tesis se presentan las conclusiones generales y la perspectiva a futuro del tema de estudio.

RESUMEN DE LA MEMORIA PARA OPTAR
AL TÍTULO DE DOCTORA EN CIENCIAS, MENCIÓN FÍSICA
POR: FERNANDA LAURA PÉREZ VERDUGO
FECHA: 2021
PROF. GUÍA: RODRIGO SOTO BERTRAN

STATISTICAL PROPERTIES OF A NON-POLARIZED ACTIVE TISSUE

This thesis aims to develop a framework to analyze the properties of epithelial tissues, taking them as an example of active matter. Understanding their mechanical behavior is of interest for biologists, physicists, and others. Several works have exploited the idea of polarized activity as an internal force, producing, for example, cellular migration. Here, instead, we use a non-polarized system in which the interaction between the elements gives the direction of motion and where novel active scalar terms are considered.

By performing analytical calculations using the vertex model, we find instabilities characterized by the coupling of some particular deformation modes that appear when the system is under stress or when cellular activity is considered, both applied homogeneously. We show an excellent agreement with numerical simulation, where the non-convexity of the cells is a geometrical proxy of the instabilities. When we consider activity in a single cell of the system, mimicking apical constrictions observed in several biological processes, we observe different geometrical responses depending on which cellular region is the active one: if it is the medial region, the active cell takes an anisotropic shape; if it is the perimeter, then the active cell tends to get an isotropic shape. We apply this analysis to the study of apical contraction pulses observed experimentally on frustrated cellular divisions in the blastula stage of the annual killifish *Austrolebias nigripinnis*. From an optimization process of geometrical observables, we can discriminate the type of activity that better describes the evolution of the system and also obtain the best fit of all parameters of the vertex model, globals, and specific for each active event.

To compare the micro and macro-scale, we describe a continuum model reported in the literature, inspired by the vertex model, obtaining a continuum version of the stress tensor. We include the cellular activity in the model, both medial and perimeter, in an active Gaussian region and study the states in mechanical equilibrium and the dynamical evolution of the system, both with the continuum model and numerical simulations of the vertex model. We show an excellent agreement between both descriptions when rescaling the time-scales between them, and the active contractility of the perimeter.

To analyze the self-organization, we perform numerical simulations of a non-polarized-fluctuating tissue, in which activity is inspired in the continuum reconstruction of the cytoskeleton. We calculate several static structure factors and find a scale separation that differentiates between a micro and a macro-scale in the model. Also, the response shows compression waves in the long-wavelength regime and an inverse energy cascade.

In the end, we present the general conclusions of our work and its perspective in the future.

En memoria de Irma Troncoso

Acknowledgements

First, I would like to thank my supervising professor Rodrigo Soto, for all the time, effort, patience, and work dedicated to my growth. Thanks for always showing me the beauty behind the sciences.

Also, I would like to thank my friends from the bachelor and doctorate program for all the great times/teas/coffees/pizzas we spent together during these years. In particular, thanks to Leonardo Leiva, Eva Díaz, Juan Pablo Campos, Enrique Calisto, Guillermo Herrera, Juan Carlos Fernandez, and Mackarena Briceño.

Special thanks to my family for always encouraging me and believing in my abilities. Thanks to Daniela Mancilla for the guidance, constructive criticism, and continuous support.

I very much appreciate the valuable discussions in the Active Matter group.

Thanks to each member of my committee for the recommendations to improve this thesis.

Finally, I would like to acknowledge the financial support from the Fondecyt project number 1180791 and the Millennium Nucleus Physics of Active Matter.

Contents

Chapter 1

Introduction

1.1 Motivation

1.1.1 Active Matter

Recently, a new field in physics called *active matter* has attracted multidisciplinary scientists. The systems treated in this area are those composed of interacting units capable of using energy from the environment or stored energy, and turn it into motion [1, 2, 3, 4, 5]. In virtue of such an extensive definition, different kind of systems enter this field. Active Brownian particles, flagellated microswimmers, swimming bacteria, living cells, epithelial monolayers, self catalytic colloids, bird flocks, fish school, and even human crowds are part of the vast studied systems. This increases the importance of making advances in this field, since new frameworks and methods could be applied to a huge amount of systems.

The continuous energy consumption of the units turns these systems into prototypes of non-equilibrium problems, in which the energy input is local. Thus, it is necessary to go beyond the usual ideas of free-energy, detailed balance, and time-reversal symmetry. To study active systems, tools from non-equilibrium statistical mechanics, soft matter, and hydrodynamics are used [4].

These systems can be separated based on the nature of the activity, in vectorial or polar activity, and scalar activity. In the vectorial or polar activity, there is a privileged direction of self-propulsion at the unit level (e.g., cellular migration and swimming bacteria), generating in some cases a global polarization as in Vicsek's model [1]. On the other hand, in the scalar activity, the units move in a direction given by the interaction with the other units (e.g., isotropically covered active colloids). Most of the investigations in active matter deal with systems in which the activity enters as a vectorial quantity [1, 2, 6].

This thesis is written in the context of the Millennium Nucleus Physics of Active Matter, led by Rodrigo Soto, Maria Luisa Cordero, and Felipe Barra, where they propose several questions about developing active matter as a field in physics [7].

1.1.2 Epithelial tissues as active systems

Epithelial tissues, also called simply epithelia, are sheets made of epithelial cells tightly bounded, letting no space in between. They cover surfaces, separating two environments, hence generating a polarized organization perpendicular to the surfaces and also to the direction of motion of the cells. An epithelial cell can be schematized by a prism, with an apical surface (contact-free), a basal surface (in contact with a substrate), and a lateral surface (Figs. 1.1 and 1.2-A). In the border of the apical side, there are cell-cell linkages, called adherens junctions. They can be distributed continuously, creating a belt, or discretely (blue segments in Fig. 1.2-D)-E)-F). There is a 200nm thin structure, called actomyosin cortex, beneath the cell membranes. This structure, consisting of cross-linked actin filaments interacting with myosin motors, is responsible for generating active stresses [8, 5]. Due to the physical contact between cells through cell-cell junctions, these forces can propagate through the tissue, generating mechanical stress on larger scales. Other sources of stress are cellular elongation (on cellular divisions) and extrusions, external traction, and active cell rearrangements. It is important to consider that these systems are complex ones involving several time scales. The common time scales for the reconstruction of adhesion molecules are tens of minutes; for actin 1min; for actin cross-linkers and myosin motors seconds [9, 10, 11].

Some general functions of the epithelial tissues are protection, secretion, and absorption. They are involved in many biological processes. In particular, our interest is related to embryonic development and morphogenesis – the creation of structural form. Some examples of these kinds of tissues are the epidermis, the surfaces of the eyes, and the surfaces of the hollow tubes and sacs through digestive, respiratory, reproductive, and urinary tracts [12].

There are several types of epithelia. They are classified by cell shape and amount of layers. Regarding the number of layers, simple epithelia are the ones formed by a monolayer; stratified epithelia, being multilayered; pseudo-stratified epithelia, the ones whose cells are in contact with the basement membrane, but only some of them have an exposed apical side. The latter have just one layer, but due to the localization of their nuclei, they give the impression of being stratified (see Fig. 1.1).

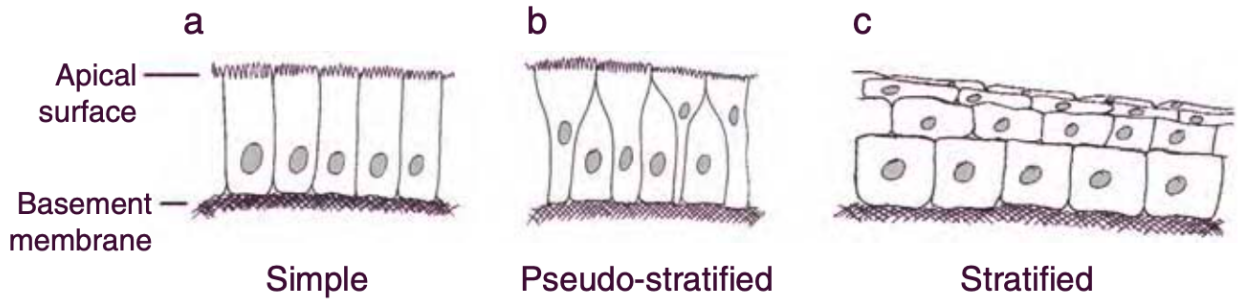

Figure 1.1: The three basic types of epithelia. In a) it is schematized the apical surface (free-contact side) and the basal membrane (in contact with a substrate), showing the polarity at a cellular level. Figure taken from Ref. [13, p. 201].

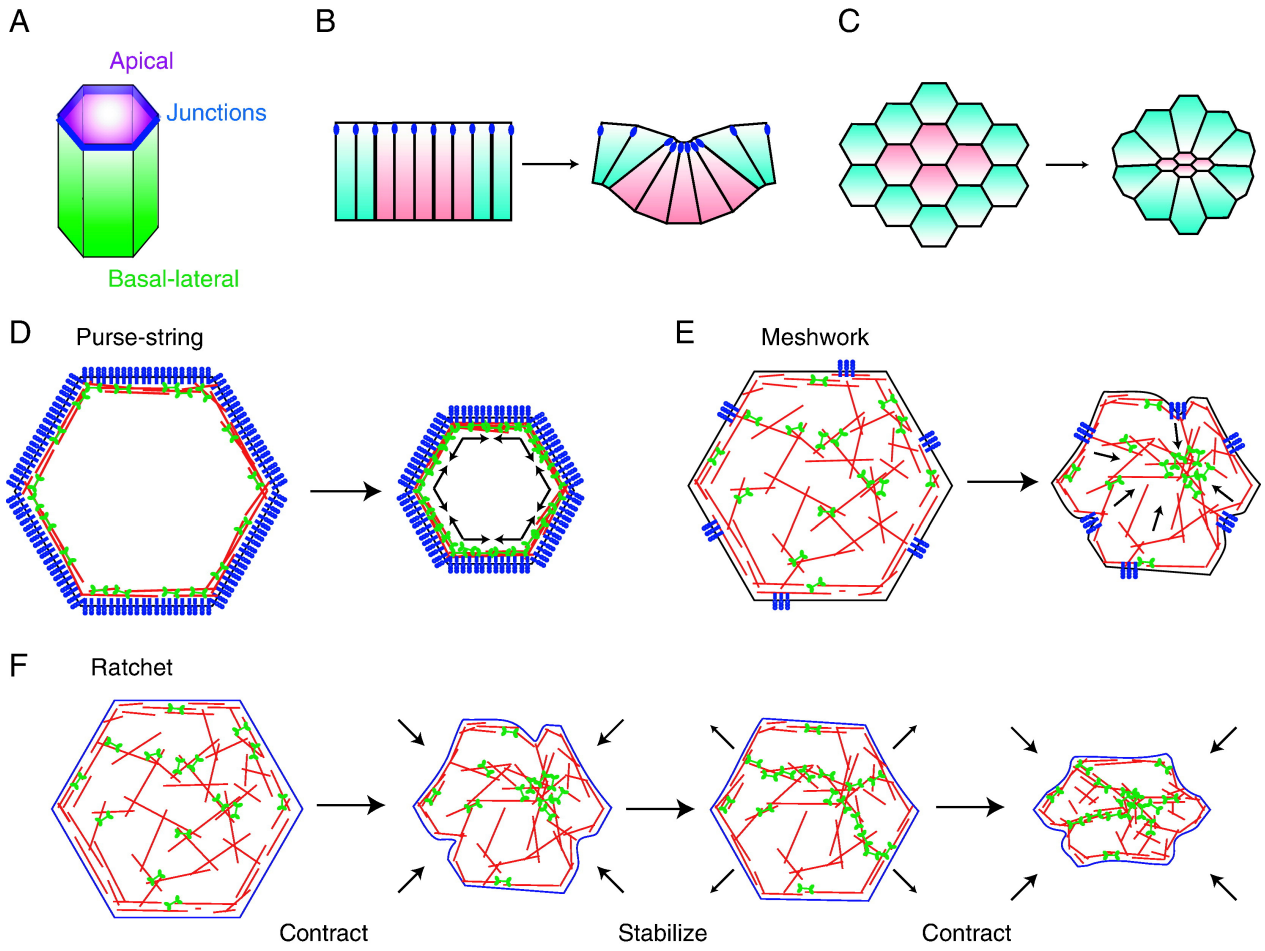

Figure 1.2: Models of apical constriction. (A) Scheme of an epithelial cell. (B) Apical–basal cross-section of cells undergoing apical constriction (pink). Apical constriction facilitates the bending/folding of epithelia. (C) Apical surface view of apical constriction. (D) The purse-string model of apical constriction. The actomyosin localized at the circumferential region generates contractile forces parallel to the cell surface. (E) The meshwork model of apical constriction. The actomyosin localized at the medial region generates contractile forces perpendicular to the cell surface, pulling discrete adherens junction sites inward to constrict the cell. (F) Ratchet model of apical constriction. Distinct phases of contraction and stabilization achieve an apical constriction. Figure taken from Ref. [14].

1.1.3 *Austrolebias nigripinnis*: early developmental stages

The LEO laboratory, led by Prof. Miguel Concha, at Faculty of Medicine of the Universidad de Chile [15, 16] has developed microscopy techniques to study the developmental stages of fish, in a controlled way, following the motion of each cell. Cellular motion in this system is slow, such that cell contractions and rearrangements take times in the scale of hours and hence can be observed with detail. A particular experiment carried out in LEO inspired this thesis.

In vivo observations using developing embryos of the annual killifish *Austrolebias nigripinnis* (A. nigripinnis) have uncovered a series of transient and apparently unsynchronized events, lasting 1.5-3.5h, (16 in the experiment) of apical constriction within the epithelial

enveloping cell layer (EVL) at the blastula stage (pre-epiboly) [17]. The active constrictions, that are normal in the development of these fish, are characterized by an initial phase of fast and short contraction followed by a relaxation period in which the original apical shape and size are recovered. As these apical constriction events are associated with a duplication of the number of nuclei per cell, it has been proposed they correspond to events of cytokinetic mitotic failures [17]. The same phenomenon is observed in other experiments, as well. One of such apical constriction events of EVL cells is shown in Fig. 1.3.

There is a biological concern in understanding how cells get into these active contractions related to frustrated cellular division. Mainly, there is interest in testing if the mechanics in the system, with possibly active terms, can reproduce the experimental data and then predict certain behaviors to test in the laboratory.

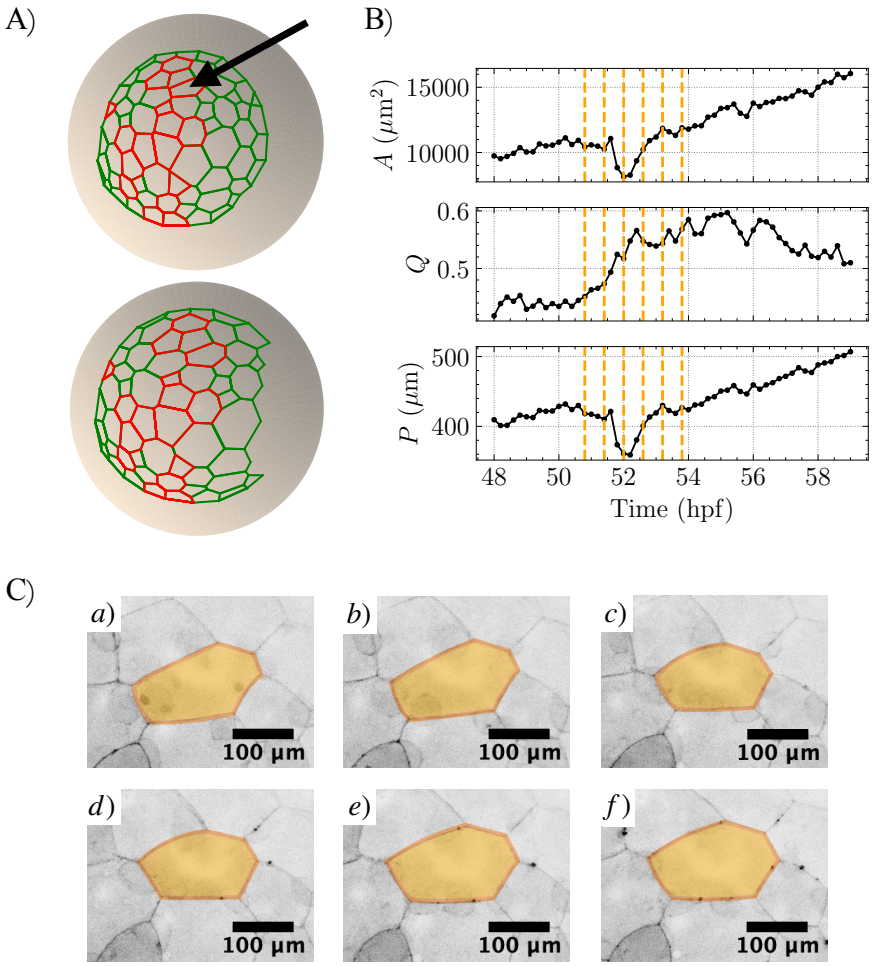

Figure 1.3: A) Temporal progression of epithelial cell shape changes during blastula stages of *Austrolebias nigripinnis* from 48 to 59 hpf (hours post fertilization). Epithelial polygonal EVL cells are denoted in green and those with notable constriction through the timescale considered are shown in red. B) Temporal evolution of cell shape changes referring to cell area (A, top), anisotropy (Q, middle) and perimeter (P, bottom) that characterize apical constriction in the target cell marked by a black arrow in A) and C). The parameter anisotropy was estimated as $Q = b/a$, where a and b (with $a > b$) are the principal semi-axes of the ellipse that better fit to the cell (for more details see Ch. 3). (C) Representative confocal microscopy-derived planar projections images of single EVL cells suffering transient events of apical constriction. The duration of the complete image sequence of cell shape changes is 3h and has been divided in three major steps including pre-constriction (a-b); active constriction (c-d) and relaxation period leading to shape recovery (e-f). A hallmark of the pre-constriction step is the accumulation of F-actin in nuclei (increase in nuclear fluorescence indicated by an arrow). Images shown in C) were captured using a representative A. nigripinnis embryo microinjected with lifeact-GFP [18].

1.1.4 Apical cellular contractions

Our view about epithelia has changed dramatically over the years from static and rigid cellular structures functioning as simple mechanical barriers to highly dynamic supra-cellular arrangements of polarized cells actively involved in morphogenetic processes [19, 20]. Examples of morphogenesis involving dynamic epithelia extend to many living organisms and include, among others, germ band elongation and gastrulation in *Drosophila* [21, 22], neural tube formation in *Xenopus laevis* [23], and convergent and extension movements in teleost fish [19]. Cells within epithelia are maintained in close contact with each other by cell-cell adhesion complexes, and the dynamic regulation of the cytoskeleton mold their shape and behavior in response to both external and internal biomechanical factors [24, 25]. Among the most relevant epithelial cell shape changes that promote tissue remodeling in a wide range of homeostatic and developmental contexts is apical constriction, the process by which the apical surface of the cell contracts, causing the cell to take on a wedged shape [26]. At the molecular level, apical constriction is regulated primarily by the contraction and flows of actomyosin networks present at the apical side of the cell. Though this mechanism is operating at a single cell level, it has been documented that events of apical constriction are highly coordinated at the supra-cellular level within epithelia. In accordance, forces generated by apical constriction are transmitted to surrounding cells through cell-cell adhesion complexes and contribute to significant macroscopic deformation of tissues [27]. Conversely, the mechanical environment imposed by neighbouring cells can regulate the dynamics of apical constriction [26]. Apical constriction can be continuous or pulsed [28, 29], and different force-dependent mechanisms have been proposed to drive this process, including the purse-string, meshwork, and ratchet models [14]. A brief description of each model is provided below.

Purse-string model

In this model, the contraction force is generated by an actomyosin ring localized in the internal perimeter of the cell – the junctional region – such that the resultant forces are aligned with the sides of the cell, (Fig. 1.2-D).

Meshwork model

In this model, the contraction force is generated by the actomyosin network localized in the central zone of the apical side – medial region. As this actin meshwork is connected to adhesion sites –adherens junction – localized in the borders of the cells, its contraction generates an inward force that pulls these sites into the cell, producing the apical constriction, (Fig. 1.2-E).

Ratchet model

In this model, the net apical constriction of a cell is achieved by discrete steps, each one consisting of an apical constriction phase of the medioapical actomyosin meshwork, followed by a stabilization phase, (Fig. 1.2-F).

The first and second models differ in the localization of the activity, i.e., which region generates the constriction. Both describe a continuum constriction. The third model, instead, describes a discrete behavior.

1.2 Computational models of epithelial tissues

There are two prominent families of modeling methods for epithelial tissues – cell-based or lattice-based, and off-lattice methods [30].

Cell-based models use meshes, in two or three dimensions, in which the units (cells), or part of them, are allowed to move following specific rules. Some of these models allow one cell per site – cellular automaton models – and others multiple cells per site – lattice gas cellular automaton. These systems are efficient for simulating large numbers of cells, but describing with adequate resolution the individual cell morphologies is beyond their scope. One on-lattice solution comes from the Cellular Potts models, which use several lattice sites to represent each cell.

Off-lattice methods, by contrast, do not follow a specific mesh for moving. There are the ones that focus on describing the cellular volume and others that describe the cell boundaries. Boundary-based models can achieve different resolutions, going from low – in Vertex models – to high resolution – in Front tracking models – increasing the computational cost in the process.

A description of the Vertex and Cellular Potts models is given in the following.

1.2.1 Vertex model

The vertex model is an off-lattice boundary-focused computational method, initially proposed to study foams and soap bubbles [31, 32], but already used extensively to describe tissues. Some recent applications include the study of tissue elongation and epithelial packing in the *Drosophila* wing epithelium [33, 34], neural tube closure in *Xenopus* [35] and also rigidity transitions in biological tissues [36].

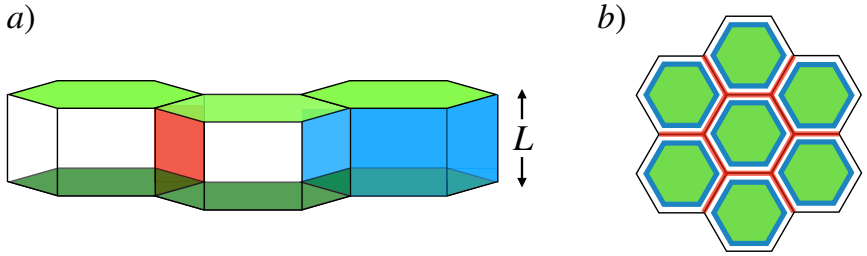

Figure 1.4: a) Diagram of three cells in three-dimensions, with height L. In green are the apical (up) and the basal (bottom) surfaces. In red, the shared faces between two cells. In blue, the entire lateral surface of one cell. b) Diagram of the apical side of a 7-cells planar tissue. In colors are represented the 3 interesting cellular regions, following the same representation as in a). Note that the red color is immediately in the interface between two cells, while the blue one corresponds at the inner cellular perimeter.

The three-dimensional model considers each cell as a polyhedron in which we can distinguish the apical and basal surface (in green in Fig. 1.4-a) from the lateral surface (in blue in Fig. 1.4-a). Surfaces in contact between cells play a particular role in cellular adhesion (in red in Fig. 1.4-a).

In this model, the position of the vertices evolves variationally, following a general energy functional given by [37, 38, 39, 40]

$$E_{3\mathrm{D}} = \sum_c \frac{K_V}{2} \left(V_c - V_{0c}\right)^2 + \sum_c K_L S_{L,c} + \sum_c K_B S_{B,c} + u^{\mathrm{apical}}, \tag{1.1}$$

where the first, second and third sums are over the c cells, and the fourth term accounts for an apical energy term

$$u_{apical} = \sum_c \frac{K_P}{2} \left(P_c - P_{0c}\right)^2 + \sum_{\mathrm{e}} K_{\mathrm{e}} l_{\mathrm{e}}. \tag{1.2}$$

V_c , $S_{l,c}$, $S_{b,c}$, and P_c, are the volume, lateral surface, basal surface, and apical perimeter of the c cell, respectively, while V_{0c} and P_{0c} are target values for the respective quantities. l_{e} is the length of the apical side e shared between two cells. The factors $1/2$ are commonly used to keep the typical form of elastic energies. Each term in Eqs. (1.1) and (1.2) has a biophysical interpretation. In Eq. (1.1), the first term, proportional to a volume elastic modulus K_V, represents the three-dimensional incompressibility; the second, proportional to the elastic modulus K_L, represents the surface tension on the lateral surface; the third, proportional to the elastic modulus K_B, represents the surface tension on the basal surface. In Eq. (1.2), the first term represents the elastic energy of a spring lying in the apical border of each cell, mimicking a contractile actomyosin ring, with elastic constant K_P ; the second, proportional to the elastic modulus K_{e}, also interpreted as a constant line tension, represents the adhesion energy cost. The elastic parameters K_V, K_L, K_B, K_P, and K_{e}, are usually considered uniform and constant (intensive parameters).

When the tissue under study has similar apical and basal surfaces and a height approximately constant L , as in Fig. 1.4-a), the apical side of the tissue can be studied by using the following energy functional

$$E_{2\mathrm{D}} = \sum_c \frac{K_V L^2}{2} \left(\frac{V_c}{L} - \frac{V_{0c}}{L}\right)^2 + \sum_c K_L \frac{S_{L,c}}{L} + u^{\mathrm{apical}}, \tag{1.3}$$

$$= \sum_c \frac{K_V L^2}{2} \left(\frac{A_c L}{L} - \frac{A_{0c} L}{L}\right)^2 + \sum_c K_L P_c + \sum_c \frac{K_P}{2} \left(P_c - P_{0c}\right)^2 + \sum_{\mathrm{e}} K_{\mathrm{e}} l_{\mathrm{e}}, \tag{1.4}$$

$$= \sum_c \frac{K_V L^2}{2} \left(A_c - A_{0c}\right)^2 + \sum_c \frac{K_P}{2} \left(P_c - P_{0c}\right)^2 + \sum_{\mathrm{e}} K_{\mathrm{e}} l_{\mathrm{e}} + \sum_c K_L P_c, \tag{1.5}$$

where now each cell is considered as a polygon with area A_c (target area A_{0c}) and perimeter P_c (target perimeter P_{0c}), in green and blue in Fig. 1.4-b), respectively. By defining $K_A = K_V L^2$ and joining the third and fourth sums as a single sum, we obtain the most usual form of the model, sum over the pair of adjacent vertices i and j with $J = K_{\mathrm{e}} + 2K_L$, we obtain the most usual form of the model,

$$E_{2\mathrm{D}} = \sum_c \frac{K_A}{2} \left(A_c - A_{0c}\right)^2 + \sum_c \frac{K_P}{2} \left(P_c - P_{0c}\right)^2 + J \sum_{\langle \mathrm{i},j \rangle} l_{\mathrm{i}j}, \tag{1.6}$$

where $J = K_e + 2K_L$, and l_{ij} is the apical cell edge shared by those vertices. With the new definitions, the first term, proportional to an area elastic modulus K_A, represents the three-dimensional incompressibility and the resistance to height fluctuations; K_P maintains its previous interpretation; J, represents the adhesion between two cells. In the literature, the parameters K_A and K_P are assumed to be positive, while there is no restriction on the sign of J [41, 42].

In Ref. [38] they do not restrict the cellular height L to be constant, and instead use a confinement energy of Gaussian polymers. They conclude that for tissues with low lateral adhesion, the two-dimensional apical vertex model is a valid approximation for squamous cells ($L \ll \langle l_{ij} \rangle$).

In most of what is published, the target parameters A_{0c} and P_{0c} are considered uniform quantities, defined as the average area and perimeter of all cells, respectively. With this consideration, it is convenient to write the energy functional by using the relative change in area and perimeter

$$\widetilde{E_{2D}} = \sum_c \frac{K_A A_0^2}{2} \left(\frac{A_c - A_0}{A_0} \right)^2 + \sum_c \frac{K_P P_0^2}{2} \left(\frac{P_c - P_0}{P_0} \right)^2 + J \sum_{\langle i,j \rangle} l_{ij}, \tag{1.7}$$

$$= \sum_c \frac{\widetilde{K_A}}{2} \left(\frac{A_c - A_0}{A_0} \right)^2 + \sum_c \frac{\widetilde{K_P}}{2} \left(\frac{P_c - P_0}{P_0} \right)^2 + J \sum_{\langle i,j \rangle} l_{ij}, \tag{1.8}$$

where now $\widetilde{K_A}$ and $\widetilde{K_P}$ are constant and uniform. In this simplified version, the first and second sum represent energy costs related to apical strain.

The position of the apical vertices $\mathbf{r}_i$, evolve as

$$\frac{d\mathbf{r}_i}{dt} = -\gamma \frac{\partial E}{\partial \mathbf{r}_i}, \tag{1.9}$$

where γ is a mobility that can be absorbed in K_A, K_P and J, setting them with units of relaxation rates times different powers of length. The direction of the velocities over a vertex i are shown in Fig. A.1. In the literature, not all the parameters of Eq. (1.5) are considered free. Since J can be absorbed in P_{0c} by redefining the perimeter of equilibrium as $\widetilde{P}_{0c} = P_{0c} - J/(2K_P)$, under some assumptions as periodic boundary conditions and constant values of the equilibrium parameters, some researchers consider $P_{0c} = 0$ [33, 41, 43] and others $J = 0$ [44]. There are also researchers that use A_{0c} and P_{0c} given by a certain relation.

In some cases, a good approximation results from considering the cells as Voronoi polygons characterized by the positions of their centers, which also evolve variationally [45, 46].

Extensions of the model are the non-planar [47] and the bubbly vertex model [48]. The latter allows to describe cells with curved sides.

Using the two-dimensional vertex model it has been found a rigidity transition (liquid-to-solid transition) in confluent tissues. In passive tissues (with no cellular motility) described

with homogenous target parameters [36], the order parameter is given by $p_0 = \widetilde{P_0}/\sqrt{A_0}$, called the *shape factor*. The transition occurs at $p_0 = p_0* \approx 3.81$, which correspond to the shape factor with $\widetilde{P_0}$ and A_0 given by the perimeter and area of a regular pentagon. For lower values the tissue behaves as a rigid material, while for higher values it behaves as a soft material. A *shape index* defined as $p_c = P_c/\sqrt{A_c}$ can be measured experimentally for each cell in a tissue. They also found that the mean value $\langle p_c \rangle_c = \bar{p}$ is also an order parameter: $\bar{p} = p_0* \approx 3.81$ for rigid (jammed) tissues, while $\bar{p}$ becomes larger than p_0* for soft (unjammed) tissues.

Some time before, Staple et al. [43] found an ordered-to-disordered transition at $p_0 \sim 3.72$, which correspond to the shape factor with $\widetilde{P_0}$ and A_0 given by the perimeter and area of a regular hexagon, by analyzing the ground states (the most relaxed network configurations) of the vertex model. They explained the transition by performing a linear stability analysis. Since biological tissues are usually very disordered, it was not clear that this transition was relevant.

1.2.2 Cellular Potts model

The cellular Potts model (CPM) is a computational method to simulate cells and tissues, initially proposed as a two-dimensional cell-based lattice model [49], inspired in the Ising model. Applications include the study of processes as wound healing [50], cell migration [51], and cell rearrangement [52]. It is also applied in other fields as foams [53].

In the classical two dimensional model, each cell is considered as a domain of the lattice defined by having the same value of the *spin* σ_{i} in each site. This value is updated for a random site probabilistically, following a Monte Carlo approach with an energy functional that in a general form is given by

$$E = \sum_c \frac{K_A}{2} \left(A_c - A_0\right)^2 + \frac{K_P}{2} \sum_c \left(P_c - P_0\right)^2 - \sum_{\langle \mathrm{i},j \rangle} J_{\sigma_{\mathrm{i}}\sigma_j} a \left(1 - \delta_{\sigma_{\mathrm{i}}\sigma_j}\right), \tag{1.10}$$

where the first and second sums are over the c cells; the third sum is over the adjacent sites i and j; $\delta_{\sigma_{\mathrm{i}}\sigma_j}$ is the Kronecker delta; and a is the size of the unit cell of the lattice. The parameters $K_A, K_P, A_c, P_c, A_{0c}$ and P_{0c} have the same representation as in the Vertex model described before. The presence of an external medium can be incorporated by assigning $\sigma_{\mathrm{i}} = 0$ in a region. This way, the term $J_{\sigma_{\mathrm{i}}\sigma_j}$ can represent the adhesion coefficient between different cells and between a cell and the medium.

In every simulation step, a random site is chosen. If it belongs to an interface between two cells, its *spin* changes from σ_{i} to σ_j (the value of the adjacent cell) with a probability which expression depends on an effective tissue temperature T related to the membrane fluctuations driven by the cytoskeleton [52]. For $T > 0$:

$$P_{\sigma_{\mathrm{i}} \to \sigma_j} = \begin{cases} \exp(-\Delta E/k_B T) & \text{, if } \Delta E > 0, \\ 1 & \text{, if } \Delta E \leq 0, \end{cases} \tag{1.11}$$

where k_B is the Boltzmann constant. In the limit of $T = 0$, it is usually used that $P_{\sigma_{\mathrm{i}} \to \sigma_j} = 0.5$ if $\Delta E = 0$.

1.3 Theoretical models

1.3.1 Vectorial activity

During development and wound healing, epithelial tissues are dynamically remodeled through cell division, growth, and cellular rearrangements. Also, cellular migration is a relevant phenomenon in these situations. Numerous works have focused on modeling these systems. Since these cellular processes impose privileged directions, they are included in the models as vectorial activities.

In Ref. [54], for example, they proposed an active vertex model (considers cellular motility), in which the cellular centers are the degrees of freedom, and the tissue is obtained by performing Delaunay and Voronoi tessellations. The essence of the model is the one we described before but now considering an extra term in the right hand side of Eq. 1.9, $v_0\hat{\mathbf{n}}_\mathrm{i}$, representing an active polarized self-propulsion. The magnitude v_0 is considered constant, and $\hat{\mathbf{n}}_\mathrm{i}$ is a polarity unit vector that undergoes random rotational diffusion. Keeping constant the rotational diffusion D_r, they find that the order parameter of the transition, varying p_0 and v_0, is given by $\bar{p}$, with $\bar{p} \approx 3.81$ in the solid phase and $\bar{p} > 3.81$. They analyze the transition for different values of D_r, obtaining that in all cases the limit with $v_0 \to 0$ (non motile cells) converges in $p_0* \approx 3.81$.

Other works with modified versions of the vertex model, including activity in a vectorial and polarized way, can be found in Refs. [55] and [56].

1.3.2 Active gels

Due to the active character of the epithelial tissues, given by their units (cells) capacity of consuming free-energy and transforming it into motion, several out-of-equilibrium properties can appear. Much interest has emerged in developing hydrodynamic theories for tissues to study these universal aspects at a large-scale.

Active gel is the term used to refer to a soft material in which detailed balance is broken locally [57]. The network of actomyosin of the cells, which plays an essential role in the mechanical behavior, is under continuous reconstruction at the expense of free-energy consumption, breaking the time-reversal symmetry, the reason why it can be studied under the formalisms developed in these kinds of models.

There are several ways of constructing a theory of gels. One is to identify the slow variables treated as fields at a mesoscopic scale and the conserved quantities and symmetries of the system. Then, one can perturb a given state keeping all the terms that respect the symmetries up to first order. This procedure is limited to small perturbations, which can be a huge limitation for a given system. Another way of developing these theories is to start with a microscopic theory and, by performing coarse-graining, obtain a large-scale set of equations. In Refs. [6] and [47], for example, they develop continuous theories for tissues motivated by the vertex model (discrete perspective) planar and non-planar, respectively. At a stress tensor level, the active gels acquire a new term called *active stress*, which characterizes the system's activity. An important note about these models is their universal character since any other system having the same symmetries should be described by the same hydrodynamic-like

equations.

A fascinating work is the one of Czajkowski (Ref. [58]), where they develop a hydrodynamic theory for tissues, coupling the cell shape and the cell motility and polarization. They find homogeneous and patterned states, like asters and banding, arising in the system due to different instabilities.

1.4 Research aims and objectives

As was described before, many works on epithelial tissues treat them as active systems in both discrete and continuum ways. These works have helped to understand the laws inside these biological systems and indirectly in other active matter systems. Nevertheless, most of them consider motile polarized tissues, where each cell has a privileged direction of motion, and there is a driving active force associated. Other kinds of activities usually studied are the cellular divisions and cellular rearrangements, both of vectorial characterization. We focus our attention on studying an active system that is non-polarized and where the activity is included in scalar variables. Also, following works in the literature, we propose including fluctuations in the system related to biophysical interpretations. Motivated by the experiment described before of the annual fish in which active contractile pulses are seen, we propose as the general objective (**GO**) of this thesis to develop and characterize a model for epithelial tissues that includes scalar cellular activity capable of generating apical constrictions.

The specific objectives are:

SO1. To model a discrete active fluctuating non-polarized tissue.

SO2. To characterize the response of a tissue under a localized active contraction pulse.

SO3. To characterize the collective fluctuations.

SO4. To model at macro-scales and perform a mapping between micro and macro-scales.

SO5. To apply the models to experimental observations in the annual fish.

1.5 Thesis overview

The present thesis consists of seven chapters. In the current chapter, we introduce the motivation of this work. Mainly, we present an overview of epithelial tissues as active systems; describe some computational models in use in the literature, and briefly explain several works in the field. Also, we describe a particular experiment realized in the Faculty of Medicine of the Universidad de Chile, which served as a motivation to our main objective.

Chapter 2 describes the general model for a discrete active fluctuating non-polarized tissue. We use the basic two-dimensional version of the vertex model, plus functions representing the fluctuations (mimicking the continuum reconstruction of the cytoskeleton) and the scalar activity on the system. Two particular active functions are described: i) proportional to Dirac delta functions (impulsive activity) and ii) contraction pulses.

Chapter 3 presents a theoretical and computational analysis of our model's stability, considering impulsive active functions, and also epithelial tissues subject to applied stresses.

This chapter corresponds to a published work, "Vertex model instabilities for tissues subject to cellular activity or applied stresses", Ref. [59]. The main conclusion is that when cells modify their equilibrium perimeter or are subject to external stresses, the tissue becomes unstable with deformations that couple pure-shear or deviatoric modes, with rotation and expansion modes. We find, from the results of numerical simulations, that at short times the instabilities cause an increase in the cellular ellipticity, and for longer times cells become non-convex.

Chapter 4 presents the study of apical contractions using our model, both entirely and up to first order in the activity (and hence deformation). The results suggest that medial activity generates anisotropic cell shapes, while inner perimeter activity tends to cause isotropic cell shapes. We also explore the consideration of plasticity in the model, and find that sufficiently slow processes of medial contractile activity, compared with the elasticity and plasticity characteristic times, can achieve cell shapes less elongated. Also, for sufficiently slow processes of perimeter contractile activity, the biggest level of contraction is reached. This chapter is part of a submitted article, "Modelling of active contraction pulses in epithelial cells using the vertex model", Ref. [60], and its new version "Geometrical characterisation of active contraction pulses in epithelial cells using the vertex model" (not submitted yet).

Chapter 5 presents the model's computational application to study the active apical contractile pulses observed during cellular mitotic events within the epithelial enveloping cell layer in the developing annual killifish *Austrolebias nigripinnis*, described in Chapter 1. We report a quantitative characterization of the pulses, using the analysis of Chapter 4. A global fit of all parameters of the vertex model is provided. This chapter is also part of the submitted article, "Modelling of active contraction pulses in epithelial cells using the vertex model", and its new version "Geometrical characterisation of active contraction pulses in epithelial cells using the vertex model" (not submitted yet).

Chapter 6 presents the mean stress of the tissue, starting from the vertex model, as usually done in literature, by defining pressure and tension terms. We show that this result corresponds to the zeroth order stress we derived in Chapter 3 (and Ref. [59]). Then, we review a continuum model which uses a 2×2 texture matrix M as a field. We incorporate an active region on the model by considering a Gaussian function that changes the equilibrium areas (medial activity) and the equilibrium perimeters (perimeter activity) of some cells. We compare the states obtained by the continuum model with those from numerical simulations using the vertex model. We also proposed a dynamical description of the continuum model and compare it with the simulations.

Chapter 7 describes the static structure factors for the velocity, contraction, change of anisotropy, and orientation angle for a fluctuating non-polarized tissue. We find a scale separation that informs us about the system's hydrodynamic scale from the analysis of the structure factors. We also report compression waves for the long-wavelength regime and inverse energy cascades. We obtain that the contraction and orientation are properties correlated in space, at a distance of 17 cells approximately. This chapter presents important information for choosing good candidates when writing a hydrodynamic theory for these systems.

Chapter 2

Our model: its ingredients

This chapter describes the discrete model of an active fluctuating non-polarized tissue. It explains the addition of fluctuations due to the cytoskeleton's continued regeneration, cellular activity, and memory or plasticity in the usual vertex model.

2.1 Vertex model for a two-dimensional planar tissue

One of our motivations is concerned with applying our results to experiments managing biological tissues. Currently used techniques allow manipulating exogenous genes to make the cell nuclei, membrane, or network fluorescent. In particular, it is possible to follow the evolution of the network formed by the tissue, understanding it as a set made of vertices and topology relations between them. With this focus, a cell-based boundary-focused model described by the vertices – the vertex model – is chosen. For simplicity, and as in many works, we assume that the tissue is a simple epithelia, planar and has resistance to height fluctuations, such that the planar version of the two-dimensional model, described before, is optime.

As described in Ch. 1, the energy functional is given by

$$E = \sum_c \frac{K_A}{2} \left(A_c - A_{0c}\right)^2 + \frac{K_P}{2} \sum_c \left(P_c - P_{0c}\right)^2 + J \sum_{\langle \mathrm{i},j \rangle} l_{\mathrm{i}j}. \tag{2.1}$$

To conserve the biophysical meaning of each term in Eq. (2.1), and since we will add memory or plasticity over the equilibrium parameters, we keep both J and P_0. We consider A_{0c} and P_{0c} given initially by the geometry in an initial instant. Then, our functional has three free parameters: K_A, K_P, and J.

Finally, the evolution of the position of each vertex, $\mathbf{r}_\mathrm{i}$, is given by

$$\frac{\mathrm{d}\mathbf{r}_\mathrm{i}}{\mathrm{d}t} = -\gamma \frac{\partial E}{\partial \mathbf{r}_\mathrm{i}}, \tag{2.2}$$

where γ represents a mobility that we absorb in the elastic parameters K_A, K_P and J. The explicit form of equations of motion given by (2.2) can be found in App. A.

2.2 Active and fluctuating vertex model, with plasticity or memory

For the purposes of this thesis, we consider only scalar activity, i.e., we do not treat cellular divisions nor cell rearrangements. We propose the inclusion of the cellular activity as rates of creation of actomyosin in different regions of the cells – medial and perimetral– represented in the terms f_{A_c} and f_{P_c} in the evolution equations of A_{0c} and P_{0c}, respectively. We also consider an internal memory (in tissues with periodic boundary conditions) or plasticity (in tissues with free boundary, as in the killifish experiment) by allowing the equilibrium parameters to relax in time. Considering these two ingredients, the equations look as follow

$$\frac{\mathrm{d}A_{0c}}{\mathrm{d}t} = (\text{medial memory/plasticity}) + f_{A_c}(t), \tag{2.3}$$

$$\frac{\mathrm{d}P_{0c}}{\mathrm{d}t} = (\text{perimeter memory/plasticity}) + f_{P_c}(t). \tag{2.4}$$

The memory terms used in tissues with periodic boundary condition in this thesis are inspired in the Kelvin model of viscoelasticity (see App. B). They are given by

$$\text{medial memory} = -\,\nu_A \left(A_{0c} - A_{00c}\right), \tag{2.5}$$
$$\text{perimeter memory} = -\,\nu_P \left(P_{0c} - P_{00c}\right), \tag{2.6}$$

where A_{00c} and P_{00c} are the initial values of the equilibrium area and perimeter, respectively. This means that after ending the cellular activity ($f_{A_c}(t) = f_{P_c}(t) = 0$), the target values will recover their initial values, ending their dynamical evolution (see App. B).

The plasticity terms, that are used when modeling the pre-epiboly of the Annual killifish (tissue with free boundary condition under expansion), are inspired in the Maxwell model of viscoelasticity (see App. B). They are given by

$$\text{medial plasticity} = -\,\nu_A \left(A_{0c} - A_c\right), \tag{2.7}$$
$$\text{perimeter plasticity} = -\,\nu_P \left(P_{0c} - P_c\right). \tag{2.8}$$

In this case, even if there is no cellular activity ($f_{A_c}(t) = f_{P_c}(t) = 0$), the target values A_{0c} and P_{0c} will continue relaxing toward the instantaneous values of area and perimeter, respectively. Also, if the force that produces the expansion of a plastic tissue (as in the pre-epiboly of the Annual killifish) is suddenly removed, the system will not recover the initial configuration, as observed in experiments using laser ablation.

Additionally, the continuum reconstruction of the cytoskeleton modifies the equilibrium parameters. We include these fluctuations by adding noise in the case of the tissues with memory, obtaining

$$\frac{\mathrm{d}A_{0c}}{\mathrm{d}t} = -\nu_A \left(A_{0c} - A_{00c}\right) + f_{A_c}(t) + \sqrt{2D_A}\xi_{A_c}(t), \tag{2.9}$$

$$\frac{\mathrm{d}P_{0c}}{\mathrm{d}t} = -\nu_P \left(P_{0c} - P_{00c}\right) + f_{P_c}(t) + \sqrt{2D_P}\xi_{P_c}(t), \tag{2.10}$$

where D_A and D_P are noise intensities, and ξ_{A_c} and ξ_{P_c} are gaussian white noises, i.e., $\langle \xi_{\alpha_c}(t) \rangle = 0, \forall t$, and $\langle \xi_{\alpha_c}(t)\xi_{\alpha'_{c'}}(t') \rangle = \delta_{\alpha,\alpha'}\delta_{c,c'}\delta(t-t')$, with $\alpha = \{A, P\}$.

When we include these kind of fluctuations in the plastic tissues, big cells tend to go bigger and small cells tend to go smaller, which make A_{0c} and P_{0c} to be increasing of decreasing all the time. Then, we do not study plastic fluctuating tissues, but only fluctuating tissues with memory.

2.3 Fluctuating tissues with memory and impulsive activity

One simple case of activity to consider when studying fluctuating tissues with memory (Kelvin model), is when the functions are proportional to Dirac delta functions as $f_{A_c}(t) = \lambda_A A_{00c}\delta(t)$ and $f_{P_c}(t) = \lambda_P P_{00c}\delta(t)$, which we call *impulsive activity*. Considering that near $t = 0$ nor the memory or the fluctuations al acting, from $t = 0^-$ to $t = 0^+$, we have

$$\frac{\mathrm{d}A_{0c}}{\mathrm{d}t} = \lambda_A A_{00c}\delta(t). \tag{2.11}$$

By integrating over the time, between $t = 0^-$ and $t = 0^+$, we obtain

$$\int_{0^-}^{0^+} \mathrm{d}A_{0c} = \lambda_A A_{00c} \int_{0^-}^{0^+} \delta(t)\mathrm{d}t,$$

$$A_{0c}(t = 0^+) - A_{0c}(t = 0^-) = \lambda_A A_{00c}. \tag{2.12}$$

$$\tag{2.13}$$

Then, this *impulsive activity* is exactly the same as considering an instantaneous change in the target values as

$$A_{0c}(t) = \begin{cases} A_{0c}(t=0^-) & \text{, if } t = 0^- \\ A_{0c}(t=0^-) + \lambda_A A_{00c} & \text{, if } t = 0^+ \end{cases} \tag{2.14}$$

and analogous for perimeter activity, where λ_A and λ_P define the amount of creation of target material in the medial and perimeter regions, respectively. Then, the equations for $t > 0^+$ are Ornstein-Uhlenbeck processes

$$\frac{\mathrm{d}A_{0c}}{\mathrm{d}t} = -\nu_A \left[A_{0c} + \lambda_A A_{00c} - A_{00c}\right] + \sqrt{2D_A}\xi_{A_c}(t), \tag{2.15}$$

$$\frac{\mathrm{d}P_{0c}}{\mathrm{d}t} = -\nu_P \left[P_{0c} + \lambda_P P_{00c} - P_{00c}\right] + \sqrt{2D_P}\xi_{P_c}(t), \tag{2.16}$$

whose numerical solutions are

$$A_{0c}(t+\Delta t) = A_{0c}(t) - \nu_A \left[A_{0c}(t) - A_{00c}\left(1-\lambda_A\right)\right]\Delta t + \sqrt{2D_A\Delta t}\mathcal{N}_{(0,1)}(t) \tag{2.17}$$

$$P_{0c}(t+\Delta t) = P_{0c}(t) - \nu_P \left[P_{0c}(t) - P_{00c}\left(1-\lambda_P\right)\right]\Delta t + \sqrt{2D_P\Delta t}\mathcal{N}_{(0,1)}(t) \tag{2.18}$$

where $\mathcal{N}_{(0,1)}(t)$ is an uncorrelated normal random variable, with zero mean and unitary variance.

Equations (2.17) and (2.18) are the most general ones. However, during this thesis we do not analyze fluctuations and *impulsive activity* at the same time.

This *impulsive activity* proportional to a delta function in time, is analogue to change directly the equilibrium parameters initially as $A_{0c} \to A_{0c}\left(1+\lambda_A\right)$ and $P_{0c} \to P_{0c}\left(1+\lambda_P\right)$. However, we choose the previous method because it can be later generalized as in the following section. Also, this redefinition of the target values can be translated to a redefinition in the shape index (described in 1.2.1), as

$$p_{0c} = \frac{\widetilde{P_{0c}}}{\sqrt{A_{0c}}} = \frac{P_{0c} - J/(2K_P)}{\sqrt{A_{0c}}} \to \frac{P_{0c}\left(1+\lambda_P\right) - J/(2K_P)}{\sqrt{A_{0c}}\sqrt{1+\lambda_A}}. \tag{2.19}$$

2.4 Active contraction pulses

To study active contraction pulses, as those seen in the pre-epibolia of the annual fish, we propose mixtures of sinusoidal functions for the active terms $f_A(t)$ and $f_P(t)$. For the general

case, we only ask for the functions to integrate zero in time. Going back to the meaning of these functions, they simulate rates of destruction of cellular structural material (that will cause the contraction) followed by a stage with a term of creation of cellular structural material (that will cause the expansion), recovering, in principle, the original size. However, the plasticity of the system may change that final size.

A general function $f_A(t)$ or $f_P(t)$ where t_0 is the starting time for the activity, and δ_1 and δ_2 are the duration of the destruction and creation phases, respectively, can be written as $f_A(t) = A_0(t=0)f(t)$ or $f_P(t) = P_0(t=0)f(t)$, with $f(t)$ a function that looks like Fig. 2.1.

$$f(t) = \begin{cases} 0 & , \text{if } t < t_0 \vee t > t_0 + \delta_1 + \delta_2 \\ -C_1 \sin\left(\pi\left(t - t_0\right)/\delta_1\right) & , \text{if } t > t_0 \wedge t < t_0 + \delta_1 \\ C_2 \sin\left(\pi\left(t - t_0 - \delta_1\right)/\delta_2\right) & , \text{if } t > t_0 + \delta_1 \wedge t < t_0 + \delta_1 + \delta_2 \end{cases} \tag{2.20}$$

By imposing the condition of conservation of the structural material, we obtain a relation between the amplitudes,

$$C_2 = C_1\delta_1/\delta_2. \tag{2.21}$$

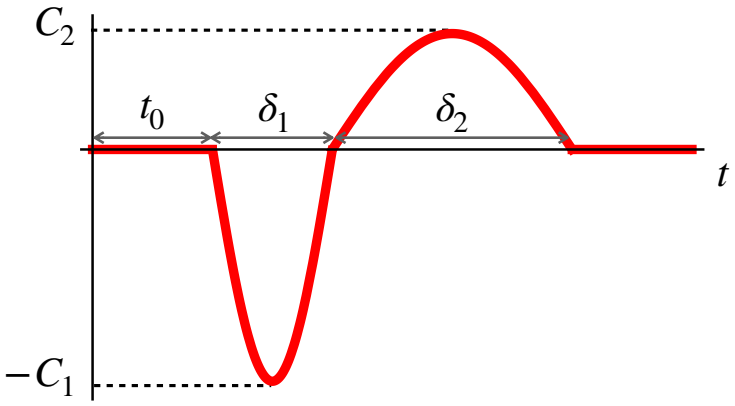

Figure 2.1: Scheme of the active function $f(t)$ for a contraction pulse. The starting time of the activity is given by t_0. The duration of the destruction and creation phases are δ_1 and δ_2, respectively. C_1 and C_2 are the amplitudes of the sinusoidal function in each phase, related by Eq. (2.21).

Chapter 3

Instabilities for tissues subject to cellular activity or applied stresses

In this chapter we show that quite generally, when cells modify their equilibrium perimeter due to their activity, or the tissue is subject to external stresses, the tissue becomes unstable with deformations that couple pure-shear or deviatoric modes, with rotation and expansion modes. For short times, these instabilities deform cells increasing their ellipticity while, at longer times, cells become non-convex, indicating that the vertex model ceases to be a valid description for tissues under these conditions. The agreement between the analytic calculations performed for a regular hexagonal tissue and the simulations of disordered tissues is excellent due to the homogenization of the tissue at long wavelengths.

In Refs. [33, 43], the vertex model was used to obtain the phase diagram of the ground state (the most relaxed network configuration) of a proliferating tissue, initially made of a regular hexagonal packing. They find a phase transition induced by cell division in the parameter space $[J/(K_A A_{0c}^{3/2}), K_P/(K_A A_{0c})]$. One phase corresponds to a single ground state, with regular hexagonal packing geometry, while the other phase corresponds to a network with many soft deformation modes, where the hexagonal packing looses stability.

Here, we develop a general framework to study the stability of tissues subject to cell activity and externally applied stresses. Neither cell division nor cell rearrangements are considered, as a matter of simplicity. This is the case of some experiments [61, 62, 17] and previous analytical calculations [43, 63, 44]. Also, topological events are non-linear and, therefore, they are not relevant to describe the emergence of the instabilities.

We use the vertex model, where the degrees of freedom are the positions of the vertices $\mathbf{r}_\mathrm{i}$, with the energy functional specified previously, Eq. (2.1), and A_{0c} and P_{0c} given by the initial geometry of each cell. The elastic coefficients K_A and K_P are assumed to be positive, and penalize deviations from the reference areas and perimeters, while there is no restriction on the sign of J, as has been discussed in the literature [41, 42]. The equation of motion of the vertices are given by Eq. (A.2).

3.1 Tissue under cell activity

We consider a regular tissue composed of N identical hexagonal cells of side a, for which $A_{0c} = 3\sqrt{3}a^2/2$ and $P_{0c} = 6a$, for all cells c. We consider cellular activity proportional to a delta function, as discussed in 2.3. Then, we let the equilibrium perimeter change as $P_{0c} \to (1+\lambda_P)\, P_{0c}$ (with $\lambda_P > 0$ for expansions and $\lambda_P < 0$ for contractions). Similarly, a change in the actomyosin activity in the medioapical side of the cells imply changes in the equilibrium cell areas, $A_{0c} \to (1+\lambda_A)\, A_{0c}$. As discussed in 2.3, this cellular activity changes the value of the shape factor $p_0 = \widetilde{P_{0c}}/\sqrt{A_{0c}}$, where $\widetilde{P_{0c}} = P_{0c} - ja/(2p)$, as

$$p_0 = \frac{P_{0c}}{\sqrt{A_{0c}}} - \frac{J}{2K_P\sqrt{A_{0c}}} \to \frac{P_{0c}}{\sqrt{A_{0c}}}\frac{(1+\lambda_P)}{\sqrt{1+\lambda_A}} - \frac{J}{2K_P\sqrt{A_{0c}}}\frac{1}{\sqrt{1+\lambda_A}}. \tag{3.1}$$

As a first case, we consider homogeneous modifications of the tissue (uniform λ_P and λ_A), modeling large portions of the tissue that change as in Ref. [62], and we investigate the stability and rigidity of this tissue, allowing it to fluctuate. The vertex positions are now given by $(I + \varepsilon U)\, \mathbf{r}_{\mathrm{i}}^{[0]}$, where $\varepsilon \ll 1$, and U is a general 2×2 matrix of components $u_{\mathrm{i}k}$, characterizing the fluctuations. Computing contributions up to $O(\varepsilon^2)$, the energy of the tissue may be written as

$$E = \sum_{\mathrm{i}=0}^{2} \varepsilon^{\mathrm{i}} \left(E_A^{(\mathrm{i})} + E_P^{(\mathrm{i})} + E_J^{(\mathrm{i})} \right), \tag{3.2}$$

where the superscripts represent the order of each term in the expansion, and E_A, E_P and E_J are the contributions proportional to K_A, K_P and J, respectively. The full expressions are given in App. C.1.

The stress tensor is $\sigma_{\mathrm{i}k} = \frac{\partial E}{\partial u_{\mathrm{i}k}}$. It has a zeroth order contribution derived from $E^{(1)}$,

$$\sigma_{\mathrm{i}k}^{(0)} = 2\sqrt{2}\hat{E}\left(\frac{2}{9}j - \lambda_A - \frac{8}{3}p\lambda_P\right)\delta_{\mathrm{i}k}, \tag{3.3}$$

that represents the total stress, with passive and active contributions, needed to maintain the deformed configuration. Here, we defined the energy scale $\hat{E} = NK_AA_0^2/2$ and the dimensionless parameters $p = K_P/(a^2K_A)$ and $j = J/(a^3K_A)$, which are the ratios between the characteristic time of the surface elasticity and the ones related to the perimeter and adhesion elasticity, respectively.

For general fluctuations, U can be expanded in Fourier modes. When computing the total energy of the tissue, the linear terms in ε cancel by spatial integration, leaving only the reference energy and the quadratic terms in the fluctuations. In physical terms, the linear contribution is eliminated by the application of a uniform external stress $\sigma_{\mathrm{i}k}^{(0)}$ by other tissues that act as a frame, imposing rigid boundary conditions. Furthermore, in the limit of small wavevectors $\mathbf{k}$, the dominant contribution comes from the case of homogeneous U, plus small corrections proportional to k^2, which we neglect henceforth. Hence, to analyze the stability of the tissue under long wavelength fluctuations, we have to determine whether the quadratic

form for homogeneous U is positive definite. Expressing U as a linear combination of four basic deformation modes,

$$U_1 = \frac{1}{\sqrt{2}}\begin{pmatrix}-1 & 0\\ 0 & 1\end{pmatrix}\text{[deviatoric]}, \qquad U_2 = \frac{1}{\sqrt{2}}\begin{pmatrix}0 & 1\\ 1 & 0\end{pmatrix}\text{[pure shear]}, \tag{3.4}$$
$$U_3 = \frac{1}{\sqrt{2}}\begin{pmatrix}0 & -1\\ 1 & 0\end{pmatrix}\text{[rotation]}, \qquad U_4 = \frac{1}{\sqrt{2}}\begin{pmatrix}1 & 0\\ 0 & 1\end{pmatrix}\text{[expansion]},$$

as $U = \sum_{\mathrm{i}=1}^{4} v_{\mathrm{i}} U_{\mathrm{i}}$, the energy can be expanded as $E^{(2)} = \hat{E}\sum_{\mathrm{i},j=1}^{4} \mu_{\mathrm{i}j} v_{\mathrm{i}} v_j$. In the case where the deformation is due to cell activity, the μ-matrix is diagonal with

$$\mu_{11} = \mu_{22} = \frac{j}{9} + \lambda_A - \frac{4p\lambda_P}{3}, \tag{3.5}$$
$$\mu_{33} = \frac{2j}{9} - \lambda_A - \frac{8p\lambda_P}{3}, \tag{3.6}$$
$$\mu_{44} = 2 + \frac{8p}{3} - \lambda_A, \tag{3.7}$$

where we used the expressions of App. C.1. It is important to recall that since we are analyzing the deformations of a planar hexagonal lattice, the elastic properties are isotropic, and the choice of the orientation of the hexagons does not change the previous results [64, p. 40].

The deformation modes U_1 and U_2 are both shears, although in different directions. Consequently, their eigenvalues, which are associated to the shear modulus, are equal. Negative values of the diagonal terms signal the development of an instability of the corresponding mode, in a single cell description. For example, large positive values of λ_A (cell expansion), would give rise to unstable rotation and expansion modes, while for large negative values of λ_A (cell compression), the deviatoric and pure shear modes become unstable.

At a tissue level, however, due to the confluent property, pure modes are not allowed. Indeed, consider for example the Fourier mode where the new vertex positions are given by $x' = x + \varepsilon \sin(2\pi x/L)\cos(2\pi y/L)$ and $y' = y - \varepsilon \sin(2\pi y/L)\cos(2\pi x/L)$, shown in Fig. 3.1-a. Depending on the position, some cells experience deviatoric deformations (in yellow), while others rotate (in red). Similarly, for the Fourier mode $x' = x + \varepsilon \cos(2\pi x/L)\sin(2\pi y/L)$ and $y' = y + \varepsilon \cos(2\pi y/L)\sin(2\pi x/L)$, shown in Fig. 3.1-b, pure shear modes (in green) coexist with expansion modes (in blue). Simple uniaxial deformations with a sinusoidal amplitudes also couple the deviatoric and expansion modes. Complementary to the long wavelength fluctuations, it is possible that the boundaries between neighboring cells move inside a supercell (analogous to optical phonons in solids) as shown in Figs. 3.1-c and d. Again, different modes coexist. The confluent property with the periodic boundary conditions frustrate the emergence of pure deformation modes. The use of fixed boundary conditions leads to the same frustration.

This unavoidable coexistence of modes implies that even though a deformation mode may seem to be unstable at the cell level, the total energy of the tissue should be computed as the sum of the different contributions that, at the end, may result to be positive definite. A detailed study of the stability of a tissue that considers the coexistence of modes is given in Section 3.4. We provide here a qualitative argument to obtain the stability limit from the

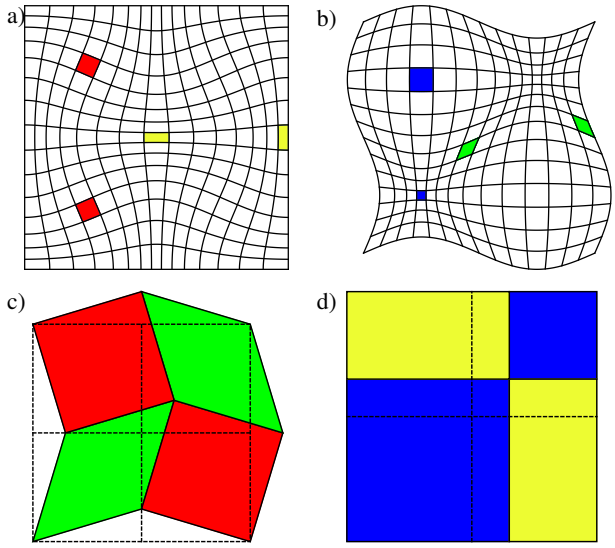

Figure 3.1: Representation of tissue fluctuations where cells subject to different deformation modes coexist. For simplicity, square cells are used in the presentation. Also, we show curved cells to make easier the observation of the fluctuation. Long wavelength fluctuations a) $x' = x + \varepsilon \sin(2\pi x/L)\cos(2\pi y/L)$ and $y' = y - \varepsilon \sin(2\pi y/L)\cos(2\pi x/L)$, and b) $x' = x + \varepsilon \cos(2\pi x/L)\sin(2\pi y/L)$ and $y' = y + \varepsilon \cos(2\pi y/L)\sin(2\pi x/L)$. Curved cells are shown to make easier the observation of the fluctuations. c) and d) fluctuations where the boundaries between neighbor cells move inside a supercell. Cells with well defined deformation modes are colored: yellow for deviatoric, green for pure shear, red for rotation, and blue for expansion.

behavior of individual cells. As the deviatoric and pure shear modes share the same value in the μ-matrix, the total energy of the tissue fluctuations shown in Figs. 3.1-a and c are equal, with a prefactor equal to $\mu_{11} + \mu_{33} = j/3 - 4p\lambda_P$. An instability is hence predicted to develop for $\lambda_P > j/(12p)$. Notably, when $\lambda_A = 0$, the shape factor is given by

$$p_0 \to \frac{P_{0c}}{\sqrt{A_{0c}}}(1+\lambda_P) - \frac{ja}{2p}\frac{1}{\sqrt{A_{0c}}}, \tag{3.8}$$

$$\to \frac{P_{0c}}{\sqrt{A_{0c}}}(1+\lambda_P) - \frac{j(6a)}{12p}\frac{1}{\sqrt{A_{0c}}}, \tag{3.9}$$

$$\to \frac{P_{0c}}{\sqrt{A_{0c}}}\left(1+\lambda_P - \frac{j}{12p}\right), \tag{3.10}$$

which is $p_0 = P_{0c}/\sqrt{A_{0c}} \approx 3.72$ (regular hexagon) at the predicted instability, and takes higher values toward the unstable predicted region. Then, the instability corresponds to the ordered-to-disordered transition reported by Staple et al. [43]. Interestingly, this instability is reached by passive tissues ($\lambda_A = \lambda_P = 0$) when considering negative values of j. Also, when $\lambda_A = 0$, the instability is predicted to take place when the shear modulus (i.e. μ_{11} or μ_{22}) vanishes, as was observed in Ref. [43]. However, when the target area has changed ($\lambda_A \neq 0$), the vanishing of the shear modulus does not signal the development of unstable modes.

To validate the predictions in actual situations, we simulate both regular and irregular tissues. Regular hexagonal tissues are made of $N = 3000$ cells arranged in a box of size

$L_x = 50\sqrt{3}a$ and $L_y = 90a$ with periodic boundary conditions. In order to avoid artificial effects due to the lattice perfections, a Gaussian noise is added to all the vertex positions in both directions, with standard deviation equals to $0.1a$. Irregular tissues are built as Voronoi cells, where the positions of $N = 3000$ center points are generated by a Monte Carlo simulation of hard disks in a box of equal size as for the regular tissue. The diameter of the disks govern the degree of dispersion of the cells. We consider an area fraction equals to 0.71, below the freezing transition, to obtain a reproducible disordered tessellation with moderate dispersion in cell sizes. The irregular tissues are made of polygons of different sizes and number of sides, implying variance in the equilibrium areas and perimeters, A_{0c} and P_{0c}. The deviatoric and pure shear modes manifest in the elongation of cells, which we characterize by the flattening parameter

$$f = (a - b)/(a + b), \tag{3.11}$$

computed for each cell in terms of its principal semi-axes a and b, calculated as the square root of the eigenvalues of the texture matrix

$$M_c = \frac{2}{n_c} \sum_{\mathrm{i} \in c} (\mathbf{r}_\mathrm{i} - \mathbf{r}_c) \otimes (\mathbf{r}_\mathrm{i} - \mathbf{r}_c) \,, \tag{3.12}$$

where the sum is over the n_c vertices conforming the cell with positions $\mathbf{r}_\mathrm{i}$, and $\mathbf{r}_c$ is the center of the cell. In Ref. [59] we use another expression that does not change any analysis. Simulations are performed solving numerically the equations of motion Eq. (A.2), which are worked out in the App. A [Eqs. (A.3), (A.13), (A.14), and (A.15)].

3.2 Short and long time scales

By performing a simple dimensional analysis we can obtain the relevant time scales of the dynamics, and define useful *short time* and *long time* values, τ_s and τ_l, respectively. The first one allows us to detect the beginning of the instability, while the second allows the non-linear terms, which saturate the eventual instabilities, to act.

We analyze the energy of a single hexagonal cell of equilibrium side a_0. At time $t = 0$ it is deformed isotropically such that the new side is $a = a_0 + a_1$, with $a_1 \ll a_0$. The area (equilibrium area) and perimeter (equilibrium perimeter) are $3\sqrt{3}a^2/2$ ($3\sqrt{3}a_0^2/2$) and $6a$ ($6a_0$), respectively. To simplify, we consider $J = 0$, in which case the energy of the cell is

$$E = \frac{K_A}{2} \frac{27}{4} \left(2a_0 a_1 + a_1^2\right)^2 + \frac{K_P}{2} \left(6a_1\right)^2 . \tag{3.13}$$

According to the dynamics of the vertex model, the cell side evolves as

$$\begin{aligned} \dot{a_1} \sim -\frac{\partial E}{\partial a_1} &= -\left[\frac{27}{4} K_A \left(2a_0 a_1 + a_1^2\right) (2a_0 + 2a_1) + 36 K_P a_1\right], \\ &= -\left[\left(\frac{27}{\tau_A} + \frac{36}{\tau_P}\right) a_1 + \frac{(81/2)}{\tau_A} \frac{a_1^2}{a_0} + \frac{(27/2)}{\tau_A} \frac{a_1^3}{a_0^2}\right], \end{aligned} \tag{3.14}$$

where we define $\tau_A = 1/(K_A a_0^2)$ and $\tau_P = 1/(K_P)$. With the selection of units such that $K_A = a_0 = 1$, we have that $\tau_A = 1$ and $\tau_P = 1/p$, which is of order 1. Hence,

$$\dot{a_1} \sim -\frac{a_1}{1/(27 + 36)} - \frac{a_1^2}{2/81} - \frac{a_1^3}{2/27}. \tag{3.15}$$

Obviously, for a confluent tissue, the linear and non-linear terms change, and there are parameters for which the coefficients change their sign and tissue is stable. Nevertheless, the present analysis allows us to extract the relaxation time scales. The shortest gives the linear evolution, $\tau_1 \approx 0.016$, and the other two describe the non-linear terms $\tau_2 \approx 0.025$ and $\tau_3 \approx 0.074$. If we consider the short time $\tau_s = 0.025$, the unstable modes will have grown exponentially, allowing us to identify their effect in the form of a change in ellipticity. For the long time $\tau_l = 0.5$, the non-linear terms have played a role and the system could have reach a steady state if the non-linear terms saturate the instability.

In the simulations, the differential equations are integrated using the Euler integration method, for various values of K_P and J, fixing units such that $K_A = 1$ and $a = 1$. The time step was fixed to $dt = 0.005$ and we study the system up to $t = 0.5$. We use values of $\lambda_{A,P}$ that are consistent in the order of magnitude with experiments using laser ablation and biochemical perturbations [33, 65, 62].

Figure 3.2 shows the results for disordered tissues, for fixed positive perimeter change $\lambda_P = 1/2$, considering $\lambda_A = \pm 1/2$. The change of the standard deviation of the flattening parameter after few time steps, displays an important increase precisely where the instability is predicted (Figs. 3.2-a and b). For larger times, an important fraction of the polygons become non-convex as a consequence of the instability (Figs. 3.2-e and f). The non-linear dynamics does not saturate the instability and, from a practical point of view, this implies that the vertex model ceases to be a valid description of tissues when these instabilities develop. Nevertheless, the non-convexity can be used as a proxy of the instability and, for a continuous quantification, one minus the mean value of the area of each cell divided by the area of the respective convex hull is presented in Figs. 3.2-c and d. For convex polygons, this order parameter vanishes, while positive values indicate that non-convex polygons appear. Importantly, the line at which the shear modulus vanishes —obtained when neglecting the coupling of modes— fails to predict the instability. For the cases shown in Figs. 3.1-b and d, the energy for the tissue has a prefactor that becomes negative when $p\lambda_P > 3/2 + 2p + j/12$, requiring an extremely large increase of the equilibrium perimeter, except if j is negative. Consequently, these modes are hardly seen and are hidden by other more unstable modes.

Figures 3.3 and 3.4 show the results for ordered tissues, for $\lambda_P = 1/2$ (predicted line: $j = 6p$) and $\lambda_P = -1/2$ (predicted line: $j = -6p$), respectively. Although the detailed geometry of the cells changes, the flattening parameter and the measure of non-convexity agree remarkable well between regular and irregular tissues, showing that the long wavelength approximation is valid. From Figs. 3.3-b and 3.4-b it is seen that $\lambda_P = -1/2$ achieves lower values for the standard deviation of the flattening parameter, which results in more rounded cells [Fig. 3.4-f-(II) versus Fig. 3.3-f-(II)].

The agreement with the analytical prediction is excellent, both when regular and irregular tissues are simulated. For cells of equal equilibrium area and complete contraction of the perimeter ($\lambda_P = -1$), the transition line in Refs. [33, 43] is reproduced. Two important differences with their work is i) the use of a fixed size box and ii) the constant topology in simulations, generating at long times non-convex polygons instead of soft networks.

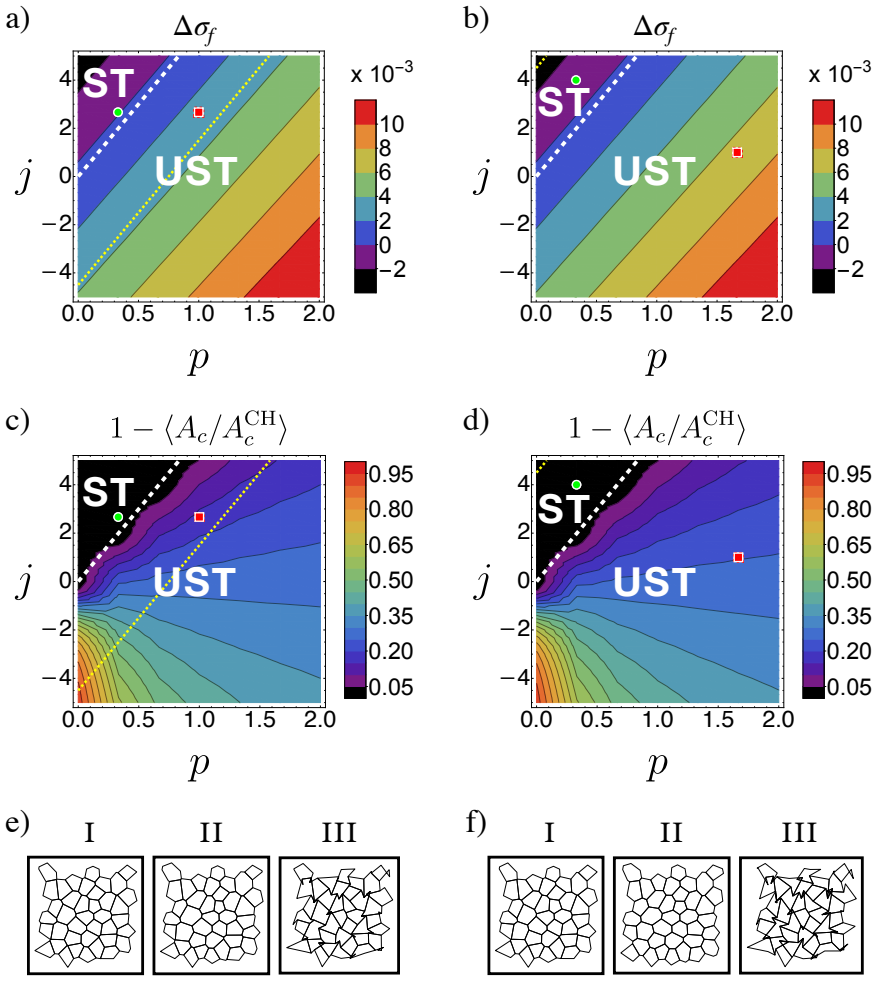

Figure 3.2: Tissue instabilities obtained in simulations of $N = 3000$ irregular cells under the action of cell activity: modification of the equilibrium perimeter with $\lambda_P = 1/2$ and the equilibrium area with $\lambda_A = 1/2$ (left) and $\lambda_A = -1/2$ (right). Top: change of the standard deviation of the flattening parameter after a short time, $t = 0.025$: $\Delta\sigma = \sigma_f(t = 0.025) - \sigma_f(t = 0)$. Negative values indicate cells become more uniform. Middle: $1-\langle A_c/A_c^{\mathrm{CH}}\rangle$, where A_c are the cell areas, A_c^{CH} the areas of the respective convex hulls, and the average is taken over all the cells, computed after a longer time, $t = 0.5$. Units are fixed such that $K_A = 1$ and $a = 1$. The thick white line and the thin yellow line are the analytical curves obtained when assuming or neglecting coupling of modes, respectively. Instabilities are predicted to the right of the lines. Note that in panels b) and d), the thin yellow line is close to the top-left corner. Stable and unstable regions, considering the coupling of modes, are labeled as ST and UST, respectively. Bottom (e) and f)): Examples of a section of an irregular tissue for each case of cell activity, indicating (I) the initial configuration at $t = 0$, and the final configurations at $t = 0.5$, for the cases of the (II) green-disk/stable and (III) red-square/unstable markers. The results are the average of six different irregular tissues, generated with the same parameters.

3.3 Tissue under pre-stress

In addition to cellular activity, the tissue can be subject to a pre-stress generated by the action of neighboring cells or tissues, fixed boundary conditions, an actomyosin network, or the drag

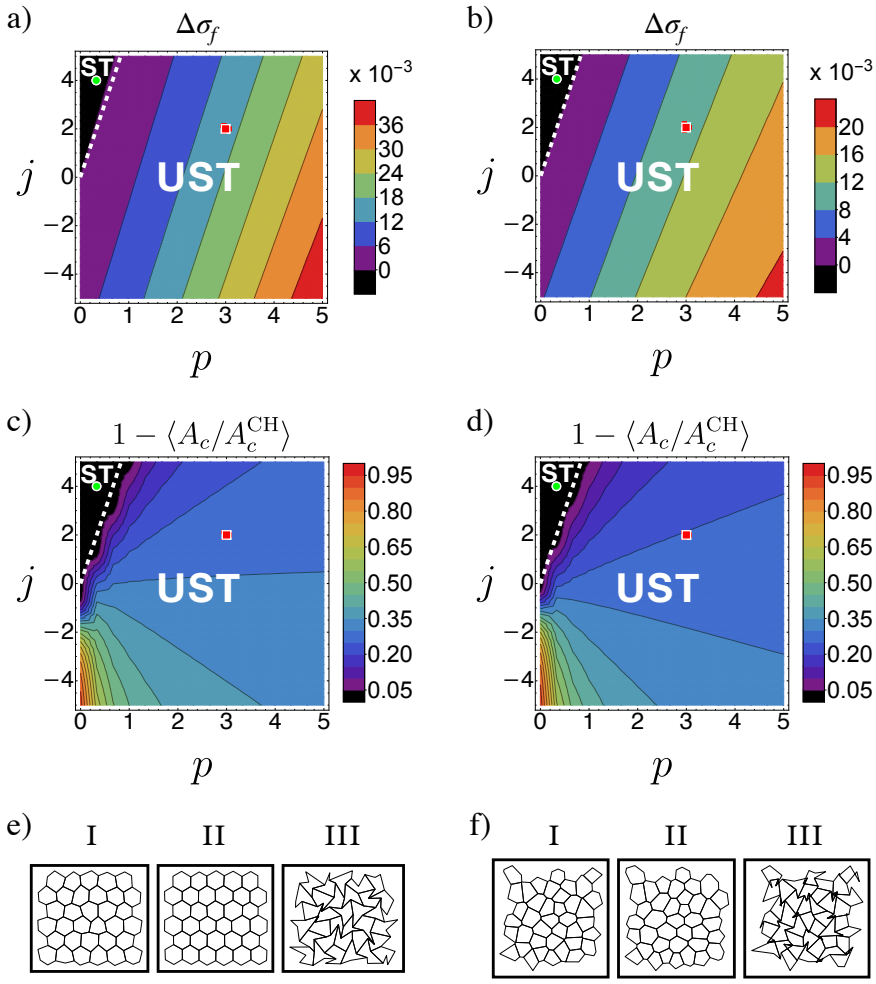

Figure 3.3: Tissue instabilities obtained in simulations of $N = 3000$ hexagonal cells with 10% of Gaussian noise over the regular positions (left) and irregular cells (right) (three different tissues considered), under cell target perimeter activity, with $\lambda_P = +1/2$ and $\lambda_A = 0$. Same representation as in Fig. 3.2.

by another expanding tissue located in an adjacent layer, causing it to get pre-deformed. To model a pre-stressed tissue, we perform an affine transformation by changing the vertices positions as $\mathbf{r}_{\rm i}^{[0]} \to \Lambda\mathbf{r}_{\rm i}^{[0]}$, where Λ is the 2×2 matrix associated to the pre-deformation. Adding fluctuations, the vertex positions are now given by $(I+\varepsilon U)\,\Lambda\mathbf{r}_{\rm i}^{[0]}$.

As for the cell activity, we consider homogeneous deformations of the tissue (uniform Λ) and perturbations U in the small wavevector limit, and we analyze first the different deformation modes independently, without dealing with their coupling. For an hexagonal cell, it is found that

$$E_A^{(2)} = \hat{E}\left[\det(\Lambda)^2\mathrm{tr}(U)^2 + 2\det(\Lambda)\left(\det(\Lambda)-1\right)\det(U)\right]. \tag{3.16}$$

The expressions for $E_P^{(2)}$ and $E_J^{(2)}$ are more involved but numerically it is found that they are always positive definite for all pre-deformations, when K_P and J are positive (see

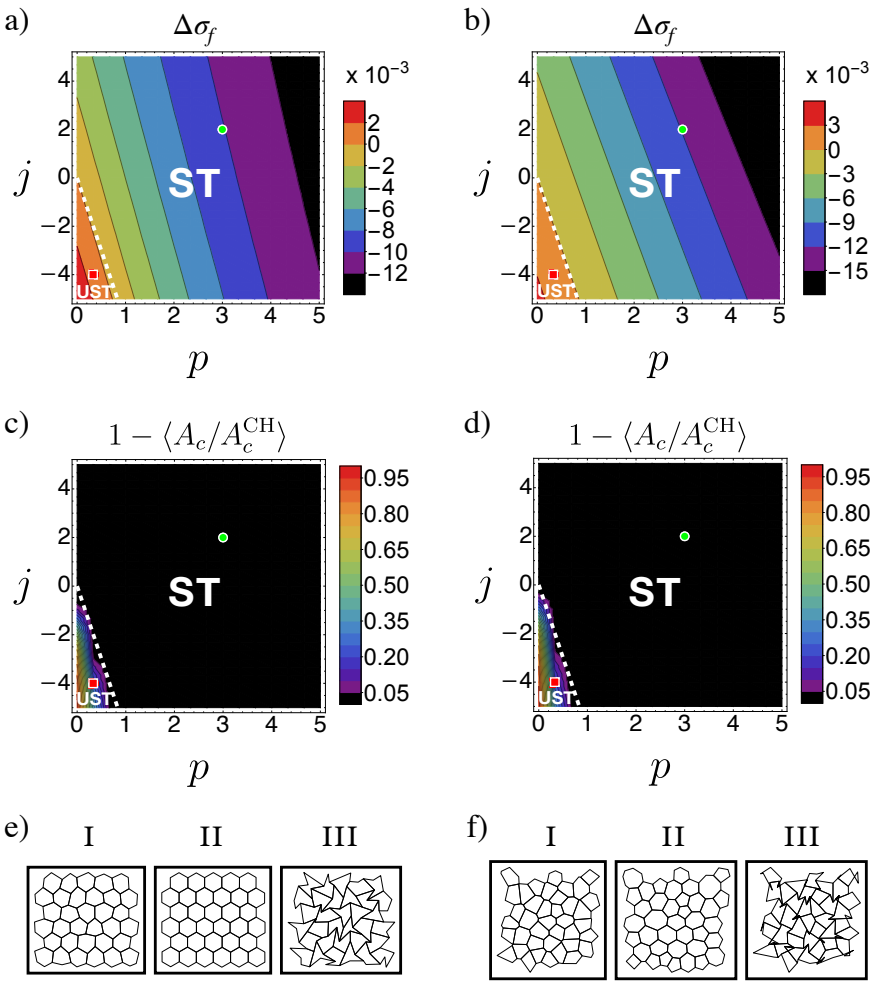

Figure 3.4: Tissue instabilities obtained in simulations of $N = 3000$ hexagonal cells with 10% of Gaussian noise over the regular positions (left) and irregular cells (right) (three different tissues considered), under cell target perimeter activity, with $\lambda_P = -1/2$ and $\lambda_A = 0$. Same representation as in Fig. 3.2.

App. C.2 for the full expressions). We conclude, then, that negative J could give rise to instabilities for any pre-strain. The case of $E_A^{(2)}$ requires more analysis. From the expression for $E_A^{(2)}$, it is found that fluctuations with $\det(U) = 0$ are always stable. Using the expansion $U = \sum_{\rm i=1}^{4} v_{\rm i} U_{\rm i}$, $E_A^{(2)}$ is diagonal with elements

$$\mu_{A11} = \mu_{A22} = -\mu_{A33} = -\bar{\lambda}, \tag{3.17}$$

$$\mu_{A44} = \frac{81}{8}\det(\Lambda)\left[\det(\Lambda) - 1/3\right], \tag{3.18}$$

with

$$\bar{\lambda} = \frac{27}{8}[\det(\Lambda) - 1]\det(\Lambda). \tag{3.19}$$

Note that whenever $\det(\Lambda) \neq 0$, either $\mu_{A11,A22}$ or μ_{A33} are negative, giving rise to possible unstable modes. When $\det(\Lambda) > 1$ (for example, under a pre-expansion), $\mu_{A11,A22}$ are negative

and the deviatoric and pure shear modes may be unstable. Also, when $0 < \det(\Lambda) < 1$ (for example, under a compression pre-deformation), μ_{A33} is negative and the rotation mode may be unstable. To fully determine the stability, we must consider the perimeter and edge contributions to the energy, as well as the mode couplings.

For isotropic pre-strain $\Lambda = (1+h)I$ ($h > 0$ for expansions and $-1 < h < 0$ for compressions), the complete μ-matrix is diagonal, with

$$\mu_{11} = \mu_{22} = (1+h)(-2h - 3h^2 - h^3 + 4hp/3 + j/9), \tag{3.20}$$
$$\mu_{33} = (1+h)(2h + 3h^2 + h^3 + 8hp/3 + 2j/9), \tag{3.21}$$
$$\mu_{44} = (1+h)(2 + 8h + 9h^2 + 3h^3 + 8p/3 + 8hp/3). \tag{3.22}$$

The stability of the relevant global mode is, therefore, described by $\mu_{11} + \mu_{33} = (1+h)(4hp + j/3)$, which can become negative for a wide range of parameters when the tissue is under compression. Simulations are performed, using the methods described in Sec. 3.1, for an isotropic compression of 50%. Fig. 3.5-left shows an excellent agreement with the analytical calculations that predict the instability line at $j = 6p$. Again, the instability manifests in an increase of the eccentricity and, at longer times, the appearance of non-convex polygons.

3.4 Anisotropic pre-stresses

Finally, *in vivo* or *in vitro* tissues are in general subject to anisotropic external deformations [66, 65, 67], causing the μ-matrix to be non-diagonal. The relevant global modes are obtained as follows. For an extended tissue, the fluctuation is expanded in Fourier modes:

$$\mathbf{r}' = \mathbf{r} + \sum_{\mathbf{k}} \boldsymbol{a}_{\mathbf{k}} \mathrm{e}^{\mathrm{i}\mathbf{k}\cdot\mathbf{r}}. \tag{3.23}$$

From the Jacobian of this transformation, the local deformation matrix is computed as $u_{\alpha\beta}(x,y) = \mathrm{i}k_\alpha a_{\mathbf{k}\beta} \mathrm{e}^{\mathrm{i}\mathbf{k}\cdot\mathbf{r}}$. Expanding it as $U(x,y) = \sum_{\mathrm{i}=1}^{4} v_{\mathrm{i}}(x,y) U_{\mathrm{i}}$, a local energy density is obtained,

$$\mathrm{e}(x,y) = (\hat{E}/L^2) \sum_{\mathrm{i},j=1}^{4} \mu_{\mathrm{i}j} v_{\mathrm{i}}(x,y) v_j(x,y). \tag{3.24}$$

Finally, the total energy of the tissue is

$$E = \int \mathrm{d}x\, \mathrm{d}y\, \mathrm{e}(x,y) = \sum_{\mathbf{k}} \sum_{\alpha,\beta=1}^{2} k^2 \mathrm{e}_{\alpha\beta}(\hat{\mathbf{k}}) a_{\mathbf{k}\alpha} a^*_{\mathbf{k}\beta}, \tag{3.25}$$

where we used that $v_{\mathrm{i}}(x,y)$ are linear combinations of the Fourier coefficients $\boldsymbol{a}_{\mathbf{k}}$ and that the Fourier modes decouple if the tissue is homogeneous on the large scale. The matrix $\mathrm{e}_{\alpha\beta}$

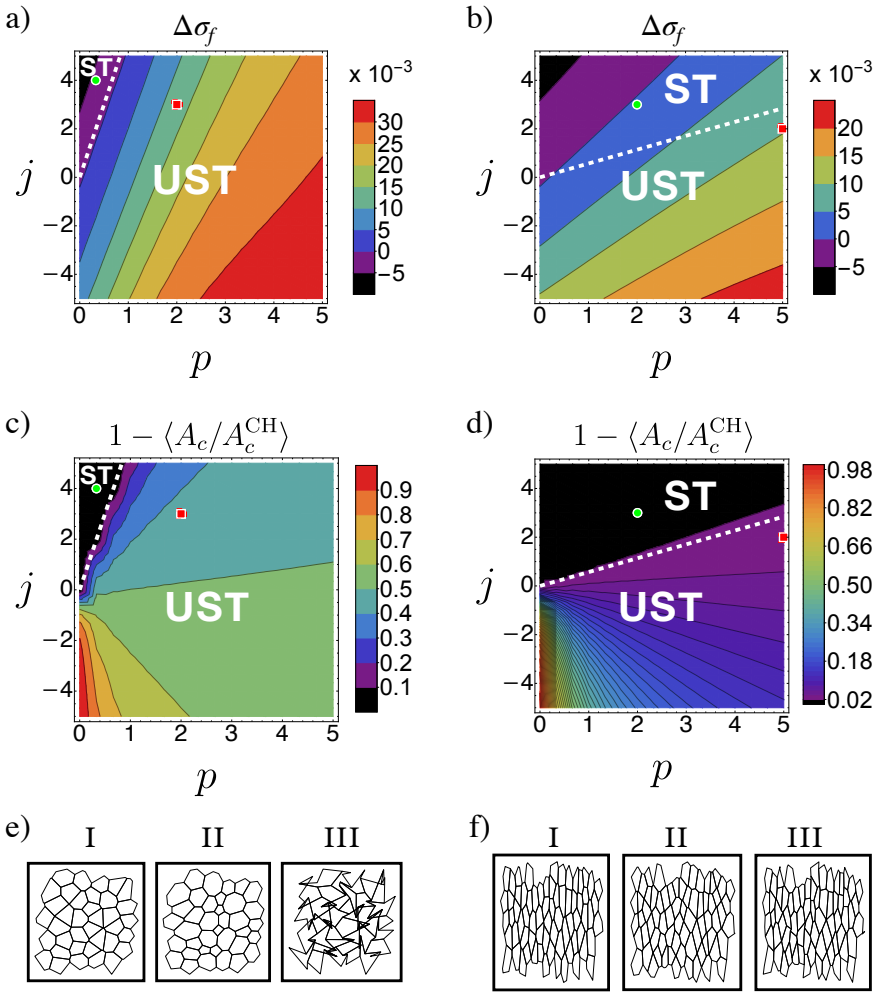

Figure 3.5: Tissue instabilities obtained in simulations of $N = 3000$ irregular cells in tissues under 50% isotropic contraction (left), and under 60% horizontal contraction plus 40% vertical expansion (right). Same representation as in Fig. 3.2.

is a 2×2 matrix with real coefficients.

$$\begin{aligned} \mathrm{e}_{11} =& \frac{1}{4}\big\{(\mu_{13}+\mu_{24})\sin 2\theta + (\mu_{11}-2\mu_{14}+\mu_{44})\cos^2\theta \\ &+ [(\mu_{22}-2\mu_{23}+\mu_{33})\sin\theta - 2(\mu_{12}+\mu_{34})\cos\theta]\sin\theta\big\}, \end{aligned} \tag{3.26}$$

$$\begin{aligned} \mathrm{e}_{12} =& \mathrm{e}_{21} = \frac{1}{8}\big\{2[-\mu_{13}+\mu_{24}+(-\mu_{12}+\mu_{34})\cos 2\theta] \\ &+ (-\mu_{11}+\mu_{22}-\mu_{33}+\mu_{44})\sin 2\theta\big\}, \end{aligned} \tag{3.27}$$

$$\begin{aligned} \mathrm{e}_{22} =& \frac{1}{4}\big\{(\mu_{22}+2\mu_{23}+\mu_{33})\cos^2\theta + (\mu_{11}+2\mu_{14}+\mu_{44})\sin^2\theta \\ &+ (\mu_{12}+\mu_{13}+\mu_{24}+\mu_{34})\sin 2\theta\big\}. \end{aligned} \tag{3.28}$$

where we used that the μ-matrix is symmetric. The stability of the tissue, considering the confluent and periodic conditions, is then obtained from the eigenvalues of the e-matrix, which depend only on the direction $\hat{\mathbf{k}}$ of the wavevector. If at least one eigenvalue is negative, the tissue develop long wavelength instabilities. When the μ-matrix is diagonal, and using that

$\mu_{11} = \mu_{22}$, it is found that the eigenvalues of $\mathrm{e}_{\alpha\beta}$ do not depend on θ and they are given by $\frac{1}{4}(\mu_{11} + \mu_{33})$ and $\frac{1}{4}(\mu_{11} + \mu_{44})$, which corroborates the simple analysis for the coupling of modes described in Section 3.1.

3.5 Examples of non-diagonal μ-matrices

Anisotropic pre-deformations generate non-diagonal μ-matrices. Using the expressions in App. C it is possible to derive the μ-matrix for different cases. Here, we present some examples where the resulting matrix is non-diagonal, needing the analysis described in Sec. 3.4 to determine the unstable modes.

For an anisotropic deformation, characterized by a 60% horizontal contraction and 40% vertical expansion, $\Lambda = \begin{pmatrix} 0.4 & 0 \\ 0 & 1.4 \end{pmatrix}$, the μ-matrix $\mu_{60/40}$ is equal to

$$\begin{pmatrix} 0.246 + 0.019j + 1.090p & 0 & 0 & 1.632p \\ 0 & 0.246 + 0.193j - 0.110p & -0.143 + 0.081p & 0 \\ 0 & -0.143j + 0.081p & -0.246 + 0.212j - 0.121p & 0 \\ 1.632p & 0 & 0 & 0.381 + 2.420p \end{pmatrix}. \tag{3.29}$$

The transition line is given by $j = 0.569p$. Simulation results for irregular tissues can be seen in Fig. 3.5-right. The agreement is again excellent when the non-convexity proxy is used. The flattening parameter does not signal the instability because, for this case there is no manifestation in the change of ellipticity as a result of the coupling of all modes.

For a tissue under a pure deviatoric deformation, $\Lambda = \begin{pmatrix} 0.5 & 0 \\ 0 & 1.5 \end{pmatrix}$, the μ-matrix μ_{dev} is equal to

$$\begin{pmatrix} 0.188 + 0.027j + 1.150p & 0 & 0 & 1.824p \\ 0 & 0.188 + 0.206j + 0.120p & -0.145j - 0.085p & 0 \\ 0 & -0.145j - 0.085p & -0.188 + 0.233j + 0.136p & 0 \\ 1.824p & 0 & 0 & 0.938 + 2.932p \end{pmatrix}. \tag{3.30}$$

The associated matrix $\mathrm{e}_{\mathrm{dev}}$ is obtained [Eqs. (3.26), (3.27), and (3.28)] and we compute the curve in parameter space where the minimum eigenvalue of $\mathrm{e}_{\mathrm{dev}}$ changes its sign. Equivalently we search when the determinant vanishes, finding the linear relation $j = -0.583p$. Note that, although the Λ and μ matrices are similar to the previous case, the transition line is radically different. Simulation results for irregular tissues can be seen in Fig. 3.6.

Finally, for a tissue subject to a pure shear pre-deformation, $\Lambda = \begin{pmatrix} 1 & 0.5 \\ 0.5 & 1 \end{pmatrix}$, the μ-matrix μ_{ps} is

$$\begin{pmatrix} 0.19 + 0.16j + 0.13p & 0.03j + 0.15p & 0.16j + 0.12p & 0.18p \\ 0.03j + 0.15p & 0.19 + 0.08j + 1.48p & -0.01j - 0.01p & 2.07p \\ 0.16j + 0.12p & -0.01j - 0.01p & -0.19 + 0.24j + 0.18p & 0 \\ 0.18p & 2.07p & 0 & 0.94 + 3.02p \end{pmatrix}. \tag{3.31}$$

The line at which the minimum eigenvalue of e_{ps} changes its sign is given by $j = -0.769p$. Simulation results for irregular tissues can be seen in Fig. 3.6.

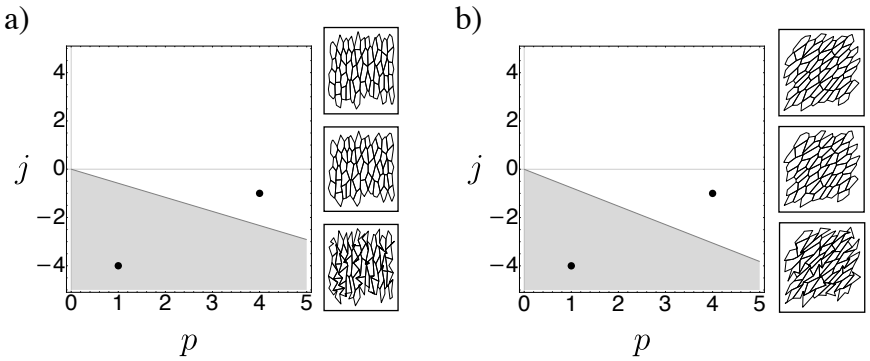

Figure 3.6: Transition line at which the minimum eigenvalue of the associated e-matrix changes its sign, for a tissue under a) 50% deviatoric pre-stress and b) 50% pure shear pre-stress. The gray areas correspond to the unstable part of the parameter space. Sections of an irregular tissue are shown for each case, indicating the initial configuration (top), at $t = 0$, and the final configurations, at $t = 0.5$, for the cases of the marked black dots, one stable (middle) and other unstable (bottom).

Our analysis from this chapter shows that stressed tissues described by the two-dimensional vertex model present instabilities in which the cells deform to increase their ellipticity, to later become non-convex. These stresses can be generated by the cellular activity when the actin ring on the perimeter of the cells changes its size or they can be external, when the tissue is pre-stressed. In any of these cases the tissue is unstable for a wide range of the model parameters.

The presence of the predicted instabilities is a stringent test of the vertex model to describe biological tissues, which under many conditions are subject to internal and external stresses. For example, in developing tissues, processes like invaginations, cell extrusion and division generate stresses. Uniaxial pulling can be generated by other tissues [68] or driven experimentally [69, 44, 62]. Also, biochemical signals can alter in large regions the activity of the tissue [62]. These and other configurations, with different external stresses, should be investigated to verify if the predicted instabilities take place and if they can act as seeds to instabilities in developing tissues. In the mechanobiological approach, forces and instabilities launch the tissue transformations during development that are necessary to generate structures and organs [70, 71]. If the vertex or similar models correctly describe the tissue dynamics, internal or external stresses can trigger the instabilities described in this chapter, which can initiate tissue transformation processes.

In this work we restricted the analysis to two-dimensional planar dynamics. Further studies are needed to analyze how the deformation modes couple with motion in the third dimension when the planar restriction is removed. For example, buckling instabilities generating wrinkles, could relax stresses instead of generating non-convex polygons.

This chapter corresponds to a published work, "Vertex model instabilities for tissues subject to cellular activity or applied stresses", Ref. [59].

Chapter 4

Geometrical characterization of active contraction pulses in epithelial cells using the vertex model

Several models have been proposed to describe the dynamics of epithelial tissues undergoing morphogenetic changes driven by apical constriction pulses, which differ in where the constriction is applied, either at the perimeter or medial regions. To help discriminate between these models, using the vertex model for epithelial dynamics, we analyzed the impact of where the constriction is applied on the final geometry of the active cell that is reducing its apical size. We find that medial activity, characterized by a reduction in the reference area in the vertex model, induces symmetry breaking and generates anisotropic cell shapes, while isotropic cell shapes occur when the reference perimeter in the model is reduced. Larger contractions are achieved when the elasticity of the active region dominates. When plasticity is included, sufficiently slow processes of medial contractile activity, compared with the elasticity and plasticity characteristic times, can achieve cell shapes less elongated. Also, for sufficiently slow processes of perimeter contractile activity, the biggest level of contraction is reached. Finally, we apply the model to describe the active apical contractile pulses observed during cellular mitotic events within the epithelial enveloping cell layer in the developing annual killifish Austrolebias nigripinnis, being able to quantitatively describe the temporal evolution of cell shape changes when perimeter activity and area plasticity are included. A global fit of all parameters of the vertex model is provided.

To describe the tissue dynamics we use the vertex model with the energy functional specified previously, Eq. (2.1), under the same considerations that in Ch. 3. Throughout this chapter, the cell contractile activity is included by incorporating variations of the reference quantities of a target cell, such that $A_{0c} \to (1 - \lambda_A)\, A_{0c}$ or $P_{0c} \to (1 - \lambda_P)\, P_{0c}$, while for the rest of the cells A_{0c} and P_{0c} keep their initial value. The dimensionless parameters λ_A and λ_P represent the activity in the medial and perimeter cellular regions, respectively. This model allows us to characterize the final shape of active cell in terms of the net achieved contraction and anisotropy. We do not study the case of contractions achieved by the ratchet model.

Because of the peripheral and medial localization of the purse string and meshwork mech-

anisms, it has been proposed that they might be most effective at generating isotropic and anisotropic tensile forces, respectively [14]. In Ref. [39], they have developed a 3D vertex model with two apical energy terms mimicking a belt and a mesh, finding different characterizations in the simulations of epithelial tubes that they relate to different anisotropic deformability: belt preserves isotropic apical cell shapes, while the mesh does not. However, there is no complete characterization of the possible scenarios for the evolution of tissues when the different models are incorporated as active cellular processes to describe the apical constriction events. Here, we show that analyzing the evolution of the cell geometry, it is possible to determine if the constriction is applied in the perimeter or medial region.

To describe and compare the apical constriction events produced either by perimeter or medial activity, we characterize the geometry of the active cell before and in the middle of the pulse, which is easily accessible in experiments.

4.1 Isolated active hexagonal cell

As the first case of study, we consider a single hexagonal cell of side a, initially in its regular shape, with the vertices positions given by $\mathbf{r}^{[0]}$, and for which its equilibrium area and perimeter are given by $A_0 = 3\sqrt{3}a^2/2$ and $P_0 = 6a$, respectively. We use the dimensionless parameters, $p = K_P/(a^2 K_A)$ and $j = J/(a^3 K_A)$. We analyze the cases of cell activity with $\lambda_A = 0.5$ or $\lambda_P = 0.5$, and characterize the response when we allow the cell to deform. These activity values are consistent in the order of magnitude with experiments that measure the changes of actin and myosin during pulsed contractions [72, 73, 74].

To obtain the area and perimeter of the deformed cell, we perform an affine transformation with respect to the centre of the cell by changing the vertex positions as $\mathbf{r}_{\mathrm{i}}^{[0]} \to (I + U)\,\mathbf{r}_{\mathrm{i}}^{[0]}$, where U is a general 2×2 matrix of components $u_{\mathrm{i}k}$, characterizing the deformation. Expressing U as a linear combination of four deformation modes,

$$U_1 = \frac{1}{\sqrt{2}}\begin{pmatrix} -1 & 0 \\ 0 & 1 \end{pmatrix} \text{[deviatoric]}, \qquad U_2 = \frac{1}{\sqrt{2}}\begin{pmatrix} 0 & 1 \\ 1 & 0 \end{pmatrix} \text{[pure shear]}, \tag{4.1}$$
$$U_3 = \frac{1}{\sqrt{2}}\begin{pmatrix} 0 & -1 \\ 1 & 0 \end{pmatrix} \text{[rotation]}, \qquad U_4 = \frac{1}{\sqrt{2}}\begin{pmatrix} -1 & 0 \\ 0 & -1 \end{pmatrix} \text{[contraction]},$$

as $U = \sum_{\mathrm{i}=1}^{4} \nu_{\mathrm{i}} U_{\mathrm{i}}$, the new area, A_f, and perimeter, P_f, can be written as functions of the four amplitudes ν_{i}. Then, the variation of the energy between the initial geometrical state and the deformed one, can be written as $\Delta E = \hat{E}\mathrm{e}(\nu_1, \nu_2, \nu_3, \nu_4)$, where $\hat{E} = K_A A_0^2/2$ is the energy scale and e is a nonlinear but analytic function (see App. D for the expressions). Fig. 4.1 shows geometrical representations of the effect of different deformations over a regular hexagonal cell. The rotation mode produces a global rotation of the cell and, for large amplitudes, an increase in size. As the model is isotropic, the energy does not depend on the global rotation and the change in size can be absorbed in the amplitude of mode U_4. Hence, without loss of generality, we can consider $\nu_3 = 0$ in what follows.

We calculate the set of amplitudes $(\nu_1^*, \nu_2^*, \nu_4^*)$ that minimizes the energy variation. Figure 4.2 shows the amplitude of each deformation mode as a response to cell activity, for the cases $\lambda_A = 0.5$ (with $\lambda_P = 0$) and $\lambda_P = 0.5$ (with $\lambda_A = 0$), respectively. Each plot considers p and

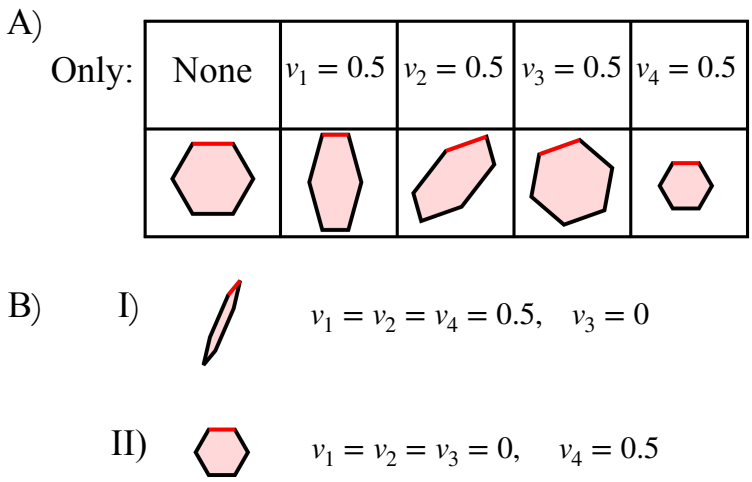

Figure 4.1: A) Scheme of a regular hexagonal cell under different deformations when considering just one mode (none, deviatoric, pure shear, rotation and contraction), with amplitude values v_i equal to 0.5. B) Scheme of a regular hexagonal cell under two different deformations combining different modes. B-I) Typical deformation of Fig. 4.2-left. B-II) Typical deformation of Fig. 4.2-right.

$j \in [0.01, 1]$ in logarithmic scales, such that the adhesion effect is never dominant and, in the left half of each plot ($p \in [0.01, 0.1]$), the medial elasticity dominates, while in the right half ($p \in [0.1, 1]$), the perimeter elasticity dominates, as explained in detail in App. D.

The amplitude of the deviatoric and pure shear modes, which are responsible for breaking the isotropy of the system, are null in the case of activity in the perimeter. Hence, cell activity in the inner cellular border might generate isotropic cell shapes, while cell activity in the medial region might generate anisotropic cell shapes. This geometrical result is expected for an isolated cell that begins with a regular shape and responds to the decrease in A_0 or P_0. To evolve toward the new preferred area (under medial activity) without changing considerably the perimeter, the cell has to break the symmetry and elongate in a given direction. On the other hand, to evolve toward the new preferred perimeter (under perimeter activity) minimizing the change in area, the cell has to keep the isotropic shape. The amplitude of the contraction modes are similar for the medial and perimeter activity. For each case, the contraction response is higher in the region of parameters in which the dominant elasticity is the one of the medial region (left half of each plot in Fig. 4.2) and of the perimeter (right half of each plot in Fig. 4.2), respectively. These observations suggest that the net contraction and the degree of anisotropy of the final shape are significant observables for characterizing a cell under this kind of cellular activity.

4.2 Active cell embedded in a tissue

At a tissue level, due to the confluent property, competition between cells takes place. To study the response of a tissue when one of the cells in the tissue actively contracts, and to determine if the perimeter and medial activities produce different geometrical responses, we consider three numerical approaches. First, in the case of small contractions, we look for the steady solution of Eqs. (A.2), which correspond to minimizing the energy functional Eq. (A.1).

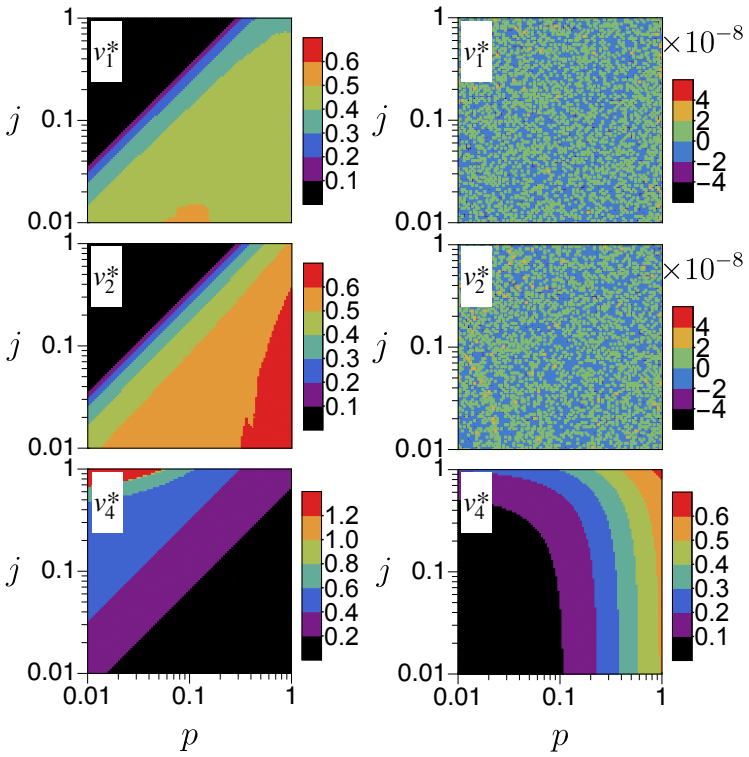

Figure 4.2: Amplitude of each deformation mode v_i^* that appear as a response of an isolated regular hexagonal cell under the modification of the equilibrium area, with $\lambda_A = 0.5$ and $\lambda_P = 0$ (left), and equilibrium perimeter, with $\lambda_A = 0$ and $\lambda_P = 0.5$ (right).

The linearized equations allow us to identify to main results, independently of the intensity of the contraction. Secondly, we solve the temporal evolution of the full non-linear equations Eqs. (A.2) for quite intense contractile activities, which gives besides the final state, the temporal scale needed to reach it. Finally, we consider plasticity in the dynamics, meaning that overstretched cells reconstruct their apical actomyosin network resulting in adaptation of the reference areas and perimeters A_{0c} and P_{0c}. In all cases, we use periodic boundary conditions. To gain statistical accuracy in the analysis of each numerical approach, we run n_s simulations, each time applying the contraction to a different cell, which is monitored to measure the change in its geometry. The amount n_s is given by $\{48, 25, 25\}$, for each numerical analysis, respectively. In the first one, the amount correspond to the total number of cells, while for the second and third one, to a 5% of the cells.

We analyze two geometrical variables: the net contraction R_c and the change on anisotropy Q_c, of the final state with respect to the relaxed state of the cell, defined as

$$R_c = \frac{A_c^{(\text{relax})} - A_c^{(\text{final})}}{A_c^{(\text{relax})}}, \tag{4.2}$$

$$Q_c = \frac{b_c^{(\text{relax})}}{a_c^{(\text{relax})}} - \frac{b_c^{(\text{final})}}{a_c^{(\text{final})}}, \tag{4.3}$$

where a_c and b_c correspond to the principal semi-axes of the ellipse that better fits the cell c, with $a > b$, calculated as in Ch. 3. Figure 4.3 shows geometrical representations of an hexagonal cell with different values of contraction R and change of anisotropy Q, when

considering that the relaxed shape corresponds to the regular hexagon (figure with values $R = 0$ and $Q = 0$).

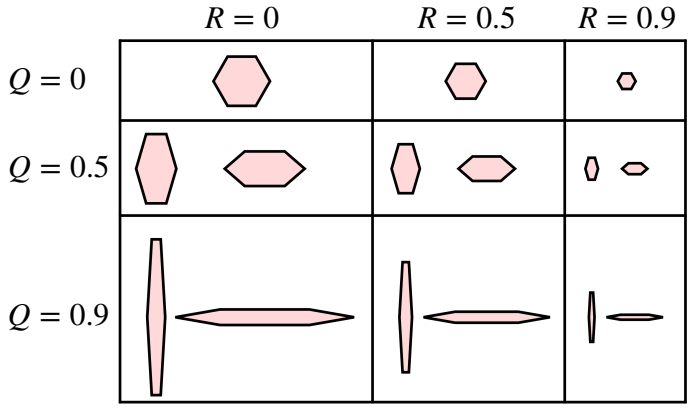

Figure 4.3: Scheme of a hexagonal cell, whose relaxed configuration corresponds to the regular hexagon, with different values of contraction R and change of anisotropy Q. Depending on the orientation of the principal axes of the texture matrix, different possibilities are obtained for a given value fo R and Q. For simplicity, two are presented, with the axes oriented horizontally or vertically.

Throughout this section, time is measured in the natural units $\hat{t} = 1/(a^2 K_A)$ and, whenever necessary, units are fixed such that $K_A = 1$ and $a = 1$. Finally, the time step used for the numerical integration of the dynamical equations is $dt = 0.01$.

4.2.1 Linear response

For this analysis, we consider tissues composed of 48 cells in a box of size $L_x = 6\sqrt{3}a$ and $L_y = 12a$ with periodic boundary conditions. The tissue is built as Voronoi cells, where the positions of 48 central points are generated by a Montecarlo simulation of hard disks. The diameter of the disks governs the degree of dispersion of the cells and we consider an area fraction equals 0.71, below the freezing transition, to obtain a disordered tessellation with moderate dispersion [59]. This irregular tissue presents a larger disorder, with variability in the number of sides, as well as in the reference areas and perimeters. The generated lattice is considered as the initial configuration from where we calculate the initial values of the reference areas and perimeters, A_{0c} and P_{0c}, used in the model. Finally, given the initial positions, we first solve Eqs. (A.2) without considering activity term for various values of K_P and J for a relaxation time $t_{\text{relax}} = 1$, to reach equilibrium (relaxed) configurations.

On the relaxed tissue, we modify the value of A_{0c} or P_{0c} to a randomly selected cell in each simulation and we write the set of linear equations $\frac{\partial E}{\partial \mathbf{r}_i} = 0$ that determine the equilibrium positions, which are linearized considering small values of $\lambda_{A/P}$ and small displacements. The linear order equations of the vertex model can be found in App. E. The resulting matrix is ill-conditioned, needing the use of the Singular Value Decomposition (SVD) method. Figures 4.4 and 4.5 show the results for the irregular tissue, with $\lambda_A = 0.1$ (and $\lambda_P = 0$) and $\lambda_P = 0.1$ (and $\lambda_A = 0$), respectively. Statistical values are calculated by alternately applying the contraction to the whole set of 48 cells (one at a time, in different simulations).

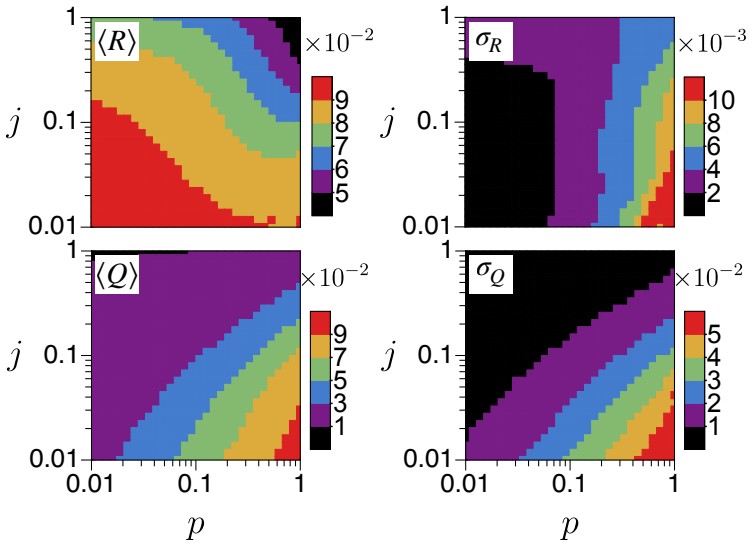

Figure 4.4: Analysis of the cellular linear response on a tissue composed of 48 irregular cells, where the averages and standard deviations are obtained by alternately applying a medial contraction with $\lambda_A = 0.1$ and $\lambda_P = 0$ over the 48 cells of the tissue. Mean values and standard deviations of the net contraction R (top) and change of anisotropy Q (bottom) of the cells with respect to the relaxed configuration ($t_{\text{relax}} = 1$), respectively.

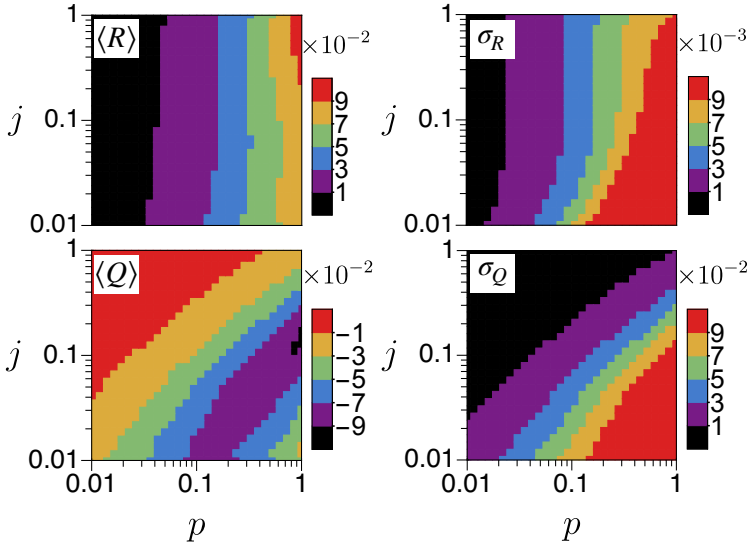

Figure 4.5: Same as in Fig. 4.4, when a perimeter contraction with $\lambda_A = 0$ and $\lambda_P = 0.1$ is applied.

We obtain a clear distinction in the linear response depending on the localization of the activity. We find that medial activity tends to elongate cells ($Q_c > 0$), while inner perimeter activity tends to make the cells more isotropic ($Q_c < 0$). Although the mean cellular contraction takes similar values with both activities, however the dependence with j is different. For medial activity it decreases for higher values of j, while for perimeter activity it is independent on the values of j. Interestingly, the standard deviation of change of anisotropy is of the same order as the mean value, while for the net contraction, it , is one order of magnitude smaller than the mean value. This reflects the high (low) dependence of

the initial geometrical condition on the change of anisotropy (net contraction).

4.2.2 Non-linear dynamic response

For larger deformations, we perform numerical simulations, solving Eqs. (A.2), using disordered tissues of 494 cells arranged in a box of size $L_x = 19\sqrt{3}a$ and $L_y = 39a$ with periodic boundary conditions. Again, irregular tissues are built as in Sect. 4.2.1.

We solve Eqs. (A.2) for various values of K_P and J. For all the simulations, we initially perform a relaxation phase, for $t_{\text{relax}} = 5$, to obtain the stationary configuration (relaxed state) of the tissue. This configuration depends on the values of j and p.Then, we apply the activity and study the system for a period $\Delta t_{\text{active}} = 10$. Figures 4.6-A and 4.7-A correspond to the disordered tissues, showing the mean values and standard deviations of R and Q at $t_{\text{final}} = 10$ (measured from the inclusion of activity). The medial and perimeter contractions, with $\lambda_A = 0.5$ (and $\lambda_P = 0$) and $\lambda_P = 0.5$ (and $\lambda_A = 0$), respectively are applied to a single cell in the tissue. The statistical properties are obtained by repeatedly changing the cell where the activity is applied, using $n_s = 25$ cells chosen at random (5% of the cells in the tissue).

Again, it is obtained that i) perimeter activities generate final cellular shapes that are more isotropic as compared to the medial activity, ii) the net contraction is higher in the region of parameters where the type of elasticity that dominates (i.e., medial or perimeter) is the same as that of the type of applied activity, and iii) the net average contraction achieved by perimeter activity is independent of j, confirming the results obtained with single cells and the linear dynamics. By fitting an exponential function to the temporal evolution of R_c and Q_c for each of cells, we obtain characteristic relaxation times τ_R and τ_Q, respectively, which are later averaged over the cells, for each point in the p-j parameter space (Figs. 4.6-A and 4.7-A). We find that, on average, for both activities, the relaxation of the change of anisotropy is slower than for the contraction. Also, the final net contraction (change of anisotropy) is achieved faster with perimeter (medial) activity than with medial (perimeter) activity, on average.

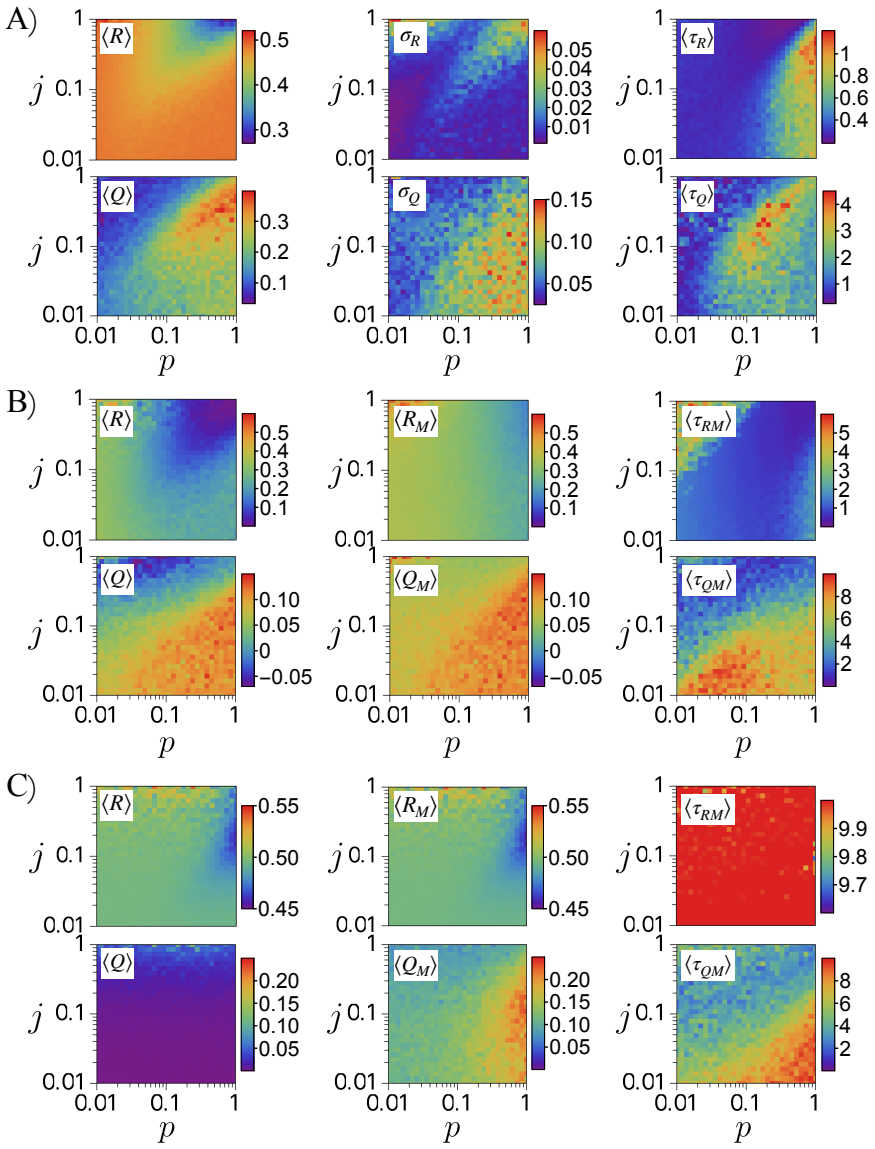

Figure 4.6: Analysis of the cellular response to medial contraction with $\lambda_A = 0.5$ and $\lambda_P = 0$ obtained by simulating tissues of 494 irregular cells up to $t_{\text{final}} = 10$. A) Mean value (left), standard deviation (middle), and characteristic time (right) of the net contraction R (up) and change of anisotropy Q (bottom) of the contractile cells, respectively. B) and C) Mean value (left), average of the maximum values (middle), and time to reach the maximum values (right) of the net contraction R (up) and change of anisotropy Q (bottom) of the contractile cells, respectively. For the statistical analysis, for each value of p and j, the contraction was applied to 25 cells chosen at random. Times are measured in units of $\hat{t} = 1/(a^2 K_a)$. The temporal evolution for selected values of parameters, shown with a grey circle and black square are shown in Fig. 4.8. In A) no plasticity is considered, while in B) $\nu_A = 1$ and $\nu_P = 0$, and in C) $\nu_A = 0$ and $\nu_P = 1$.

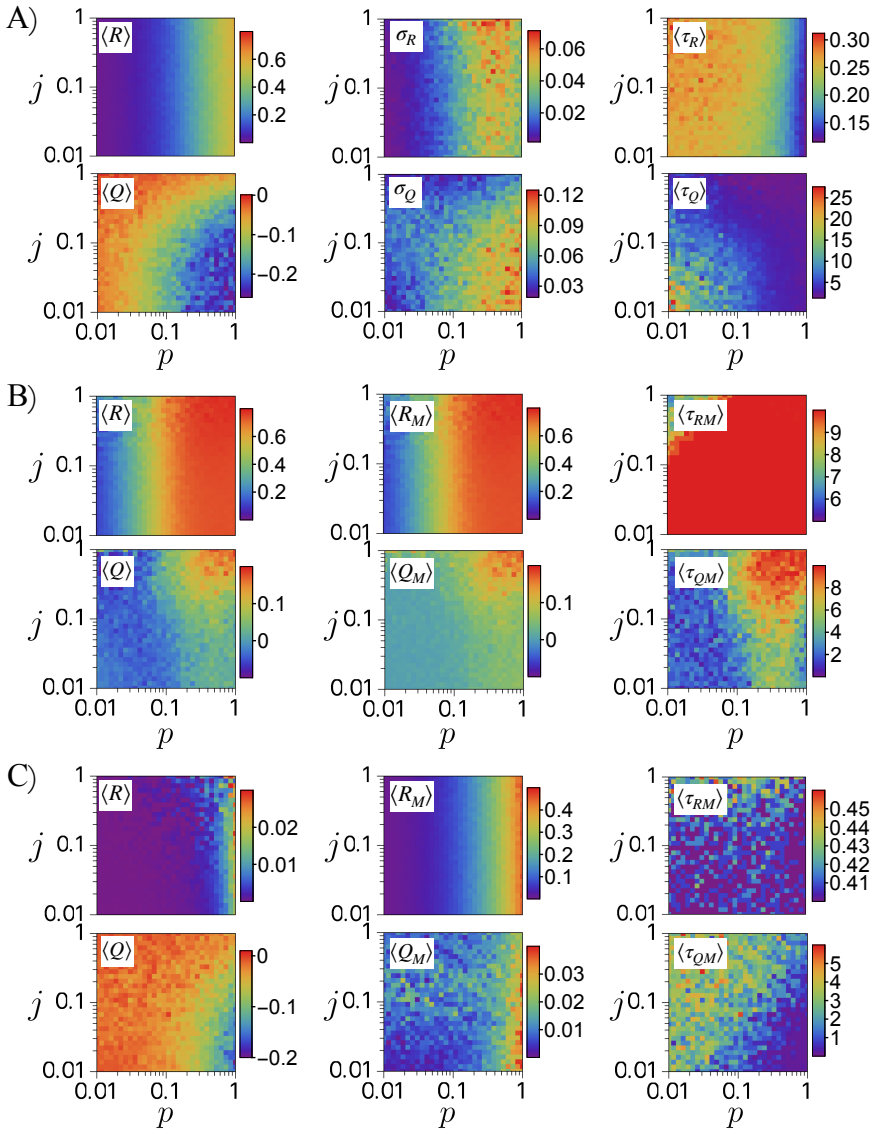

Figure 4.7: Same as in Fig. 4.6, when perimeter contractions with $\lambda_A = 0$ and $\lambda_P = 0.5$ are applied. The white noisy curve in $\langle Q \rangle$ is the contour at which $\langle Q \rangle = 0$; the black-dashed line corresponds to its linear approximation. The temporal evolution for selected values of parameters, shown with a grey circle and black square are shown in Fig. 4.9. In A) no plasticity is considered, while in B) $\nu_A = 1$ and $\nu_P = 0$, and in C) $\nu_A = 0$ and $\nu_P = 1$.

4.2.3 Plasticity

As mentioned, tissues present plastic behavior, where for a sustained applied stress, yielding takes place. At the macroscopic level, it is described with active gels models [75, 76], where viscoelastic terms are included. In the vertex model, we include plasticity by allowing the reference areas and perimeters to evolve, according the present value of the deformation. Namely, we add to the model the following dynamical equations

$$\frac{\mathrm{d}A_{0c}}{\mathrm{d}t} = -\nu_A \left(A_{0c} - A_c\right), \tag{4.4}$$

$$\frac{\mathrm{d}P_{0c}}{\mathrm{d}t} = -\nu_P \left(P_{0c} - P_c\right), \tag{4.5}$$

where ν_A and ν_P give the plastic relaxation rates, which are related to the reconstruction time of the actomyosin network. These equations are equivalent to the Maxwell model of viscoelasticity.

Again, we simulate for $t_{\text{final}} = 10$. Figures 4.8 and 4.9 show the temporal evolution of R_c and Q_c for a given cell in the irregular tissue when the plastic evolution of the area and perimeter are switched on or off. When plasticity is considered, the evolution can be non-monotonic, with R_c and Q_c decaying slowly to the initial values.

For a more systematic analysis, we perform a statistical analysis considering the temporal evolution for irregular tissues, where $n_s = 25$ cells are chosen at random to apply the contraction. Three quantities are computed: i) the mean value of the net contraction and change of anisotropy with respect to the relaxed configuration, both at $t_{\text{final}} = 10$, $\langle R \rangle$ and $\langle Q \rangle$, respectively; ii) the average maximum values of the two previous quantities, $\langle R_{\max} \rangle$ and $\langle Q_{\max} \rangle$; and iii) the average time at which the maximum values are achieved, $\langle \tau_{R\max} \rangle$ and $\langle \tau_{Q\max} \rangle$. The results are shown in Figs. 4.6-B ($\lambda_A = 0.5, \nu_A = 1$), 4.6-C ($\lambda_A = 0.5, \nu_P = 1$), 4.7-B ($\lambda_P = 0.5, \nu_A = 1$), and 4.7-C ($\lambda_P = 0.5, \nu_P = 1$).

We find that when plasticity is on the same variable as the activity (e.g., both on the perimeter), on average the evolution of the cellular contraction has a maximum at a short time ($t \sim 1$) and then decays (examples of these overshooting behaviors are seen in Figs. 4.8 and 4.9). Also, the maximum values are smaller than in the non-plastic model. On the contrary, if plasticity is on one variable and the activity on the other (e.g., plasticity on the area and activity on the perimeter), the evolution of the cellular contraction is on average a monotonically increasing function and reaches higher values with less variability than in the non-plastic case.

For the change of cellular anisotropy, in the case of medial activity, we obtain smaller values than in the non-plastic model, for both kinds of plasticities. There are even some points in the p-j space, when the medial region is plastic, with negative values, meaning that cells become more isotropic, contrary to the case without plasticity. In the case of perimeter activity, Q increases on average for both kinds of plasticities. When the plasticity is in the equilibrium area, most of the p-j space where the perimeter (medial) elasticity dominates has positive (negative) values of anisotropy, while when the plasticity is in the equilibrium perimeter, most of the p-j space has negative values of anisotropy, for both regimes of elasticity. In general, addition of plasticity in the perimeter region can generate a high degree of homogeneity in the geometrical response in the p-j space.

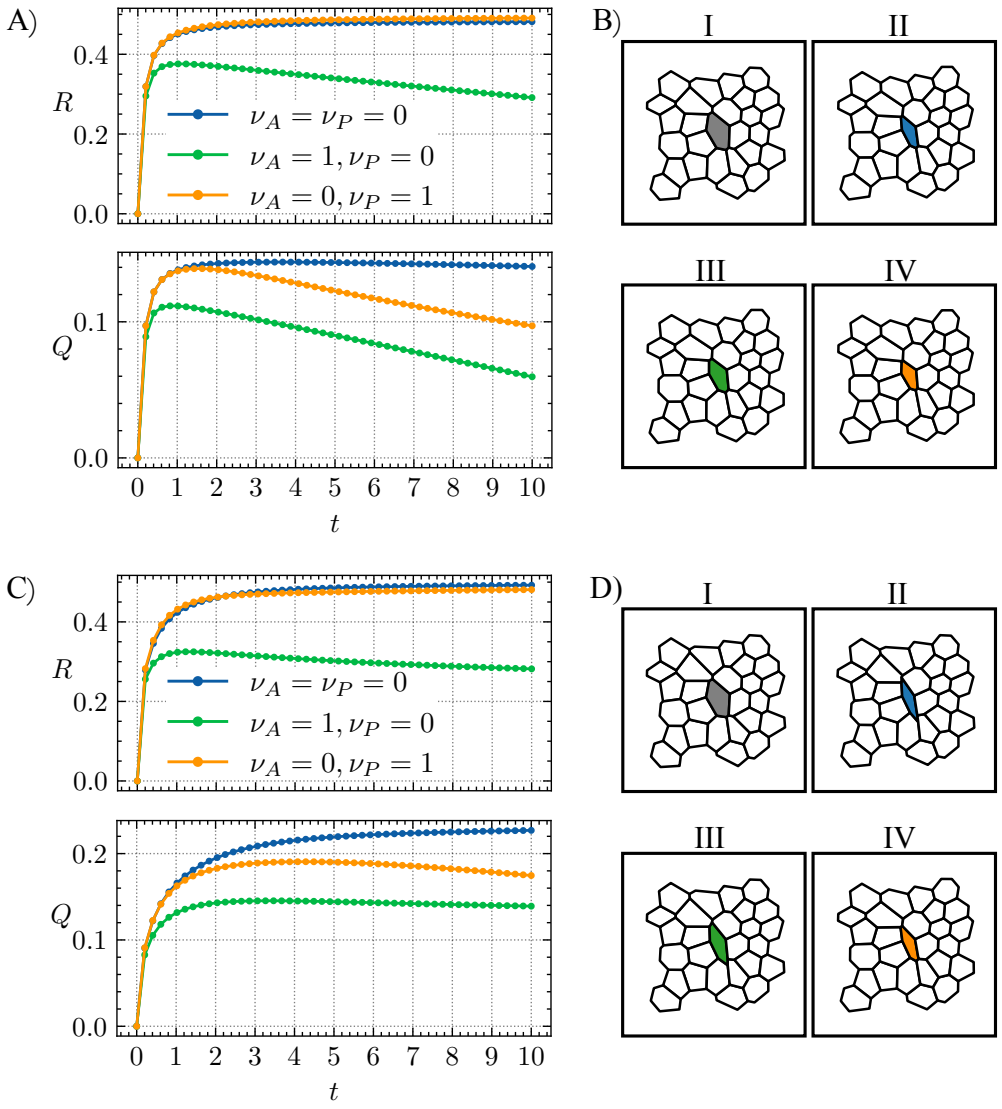

Figure 4.8: Temporal evolution of the geometrical variables for a selected cell in an irregular tissue, with parameters $(p = 0.02, j = 0.1)$ (up), and $(p = 0.5, j = 0.1)$ (bottom). A-C) Net contraction R (up) and change of anisotropy Q (bottom), both measured with respect to the relaxed configuration at $t_{\text{relax}} = 5$ after a medial contraction with $\lambda_A = 0.5$ and $\lambda_P = 0$. Three cases are considered: no plasticities (blue), with plasticity in the medial region (green), and with plasticity in the perimeter (orange). B-D) Section of the irregular tissue for each case of cell activity and plasticity, indicating (I) the relaxed configuration at $t_{\text{relax}} = 5$, and the finals configurations at $t = 10$, for the cases of (II) no plasticity, (III) medial plasticity only with $\nu_A = 0$, and (IV) perimeter plasticity only with $\nu_P = 0$.

In summary, the net contraction achieved with perimeter activity can be even larger if plasticity in the medial region is added in slow processes (compared with the characteristic times of elasticity and plasticity), at the expense of elongating slightly the cells. This combination (perimeter activity and medial plasticity) in the dynamics is the one that produces the maximum level of contraction.

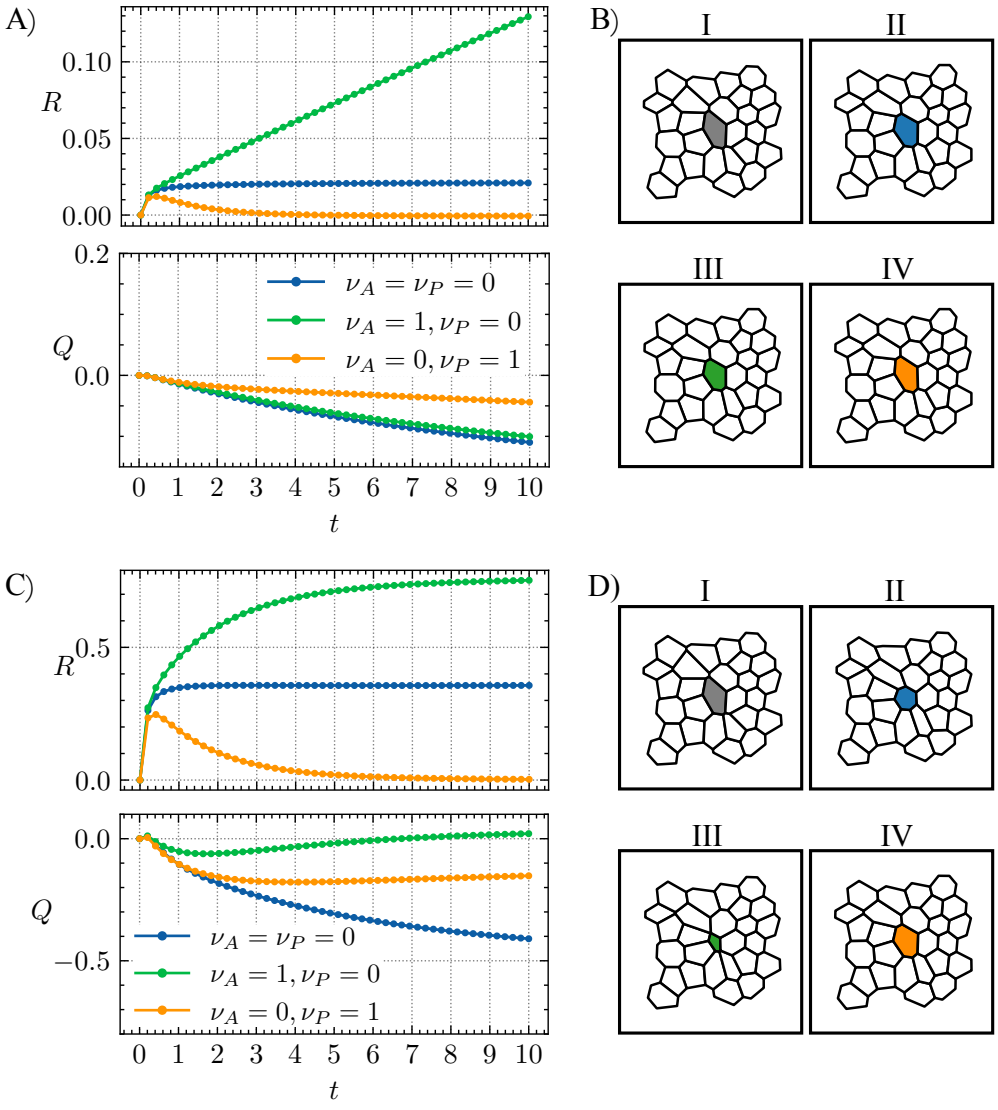

Figure 4.9: Same as in Fig. 4.8, where a perimeter contraction with $\lambda_A = 0$ and $\lambda_P = 0.5$ is applied.

Our successive analysis (one isolated active cell, an active cell embedded in a tissue with linear response and full non-linear dynamics) showed that apical constrictions described by the two-dimensional vertex model where the activity enter as modifications of the equilibrium parameters, present different geometrical characterization that depends on the cellular region taken as the active zone. For medial or perimeter activity, cells contract more efficiently when the elasticity is dominated by the active region. This feature is robust and maintained when plasticities are considered in the system. For the anisotropy, in the non-plastic case, when the inner perimeter of the cell is active, cells tend to achieve circular shapes with the contraction, while when the medial region of the cell is active they reached elongated shapes. This feature, in contrast, does not hold when the medial region is plastic, in which case an active perimeter can generate elongated shapes.

Chapter 5

Application: *Austrolebias nigripinnis* pre-epiboly stage

In this chapter we study the mechanical behavior of the cells that form the epithelial tissue present in the pre-epiboly stage in the experiment of the annual fish *Austrolebias nigripinnis* performed by the LEO laboratory, at the Faculty of Medicine of the Universidad de Chile, reported in Ref. [17]. In particular, we test if the mathematical model analyzed in Ch. 4 is accurate to study the active contractile pulses.

We are able to quantitatively fit the pulses of 15 cells with a reduced number of parameters (4 global parameters and 3 specific parameters per cell), of one experiment. Also, the analysis shows that the pulses, in which cells contract keeping roughly isotropic shapes, and thus reducing both their areas and perimeters, are better described with activity only in the perimeter of the cells and plasticity on the areas.

5.1 Experimental information

In the experiment carried out at the LEO laboratory, the pre-epiboly started 48 hours post fertilization (hpf), and finished at $56 - 58$ hpf. At the beginning of the pre-epiboly the system has an approximately spherical shape with radius $R = 590\mu$m. Inside of the sphere there is a yolk that contains nutritional components; over it, in the north pole, also called animal pole, there is an epithelial enveloping cell layer (EVL) composed of 68 cells, with mean side $l_0 \sim 50\mu\text{m} \sim 0.1R$, that covers a small part of the sphere (12%), whose thickness is $h \sim 5\mu$m. During the pre-epiboly the epithelial cells rearrange, decreasing their height and inducing an expansion of the epithelial tissue over the sphere, covering $\sim 15\%$ of the sphere. In this process, it is observed that 16 cells (in red, in Fig. 1.3) suffer active contractile pulses, in a non-correlated way, with lasting times between 1.5 and 3.5h. These constrictions are characterised by an initial phase of fast and short contraction followed by a relaxation period in which the original apical shape and size are recovered. As these apical constriction events are associated with a duplication of the number of nuclei per cell it has been proposed they correspond to events of cytokinetic mitotic failures [17]. Using the EVL of annual killifish at the blastula stage for modeling apical constriction has at least two major advantages in

comparison with other developing epithelia. First, at this phase the EVL is composed of a small and fixed number of cells of considerable size. Second, no major morphogenetic movements occur during the events of apical constriction. These apical constriction events are therefore suitable for the presented analysis in Ch. 4.

The LEO laboratory provided us the data of the position of the vertices of the cells in the tissue acquired every 0.2h. In the initial time of the experiment they are able to capture the information of all the vertices (Fig. 1.3-A-Up). Then, due to the motion of the system, some most external vertices get out of the microscopical view. By the end of the experiment the visible vertices are the ones shown in Fig. 1.3-A-Bottom.

In the pre-epiboly we have the complete data of 59 cells. Fig. 1.3 shows the three dimensional reconstruction of the experimental configuration of the tissue at the beginning (information of the entire tissue) and at the end of the pre-epiboly (information of 59 cells). Fig. 5.1 shows the polygon side distribution. This distribution does not change in time due to the lack of cellular divisions or cellular extrusions. Fig. 5.2 shows the distribution of the experimental cell areas and perimeters at $t = 48$ hpf and $t = 59$ hpf. The cell perimeters are calculated by taking the euclidian distances (not the geodesics) between the vertices, which is a good approximation (with lower computational cost) given that the mean side of the cells is $l_0 \sim 0.1R$. The areas are calculated using the triangularization method with respect to the center $\mathbf{R}_c$ of each c cell, computed as the mean position between all the vertices, and considering the normal vector as $\hat{\mathbf{n}}_c = \hat{\mathbf{R}}_c$. The anisotropies are calculated similar as in Ch. 3, by computing the eigenvalues of the texture matrix, Eq. (3.12). However, this time M_c is a 3×3 matrix, with eigenvalues a^2, b^2 and c^2. a, b and c are the respective principal semi-axes of and ellipsoid, with c, the minimum eigenvalues, representing the height of the cell, while a and b represent the two dimensional approximation of the apical surface to an ellipse. The anisotropy is finally defined as $Q_c = b/a$.

Figure 5.3 shows the evolution of the area A_c, anisotropy Q_c and perimeter P_c of four active cells, during the pre-epiboly. The curves of A_c and P_c show a passive linear behavior plus the contraction event, while Q_c has a more noisy linear behavior. On the other hand, Fig. 5.4 shows the evolution of these quantities of four non active cells, during the pre-epiboly. It is clearer the linear behavior of A_c and P_c and how noisy Q_c is. Some cells form the border show more complex behaviors. For example, cells in Fig. 5.5 seem to decrease the area and stop the increment of the perimeter at some time. Also, some experimental points escape from the expected behavior. Since the data is taken from a microscope located upside, there could be some errors in the measurement of the most external vertices. Then, we decide to fix the motion on the most external vertices of the tissue whose positions are measured during the entire experiment to the values given by the experiment. This procedure leaves us with an effective tissue, presented in Fig. 5.6, which border motion is known experimentally, every 0.2h. In the simulations we use a linear interpolation of the data to obtain the motion every Δt, which is the time step for the numerical integration of the vertex equations of motion.

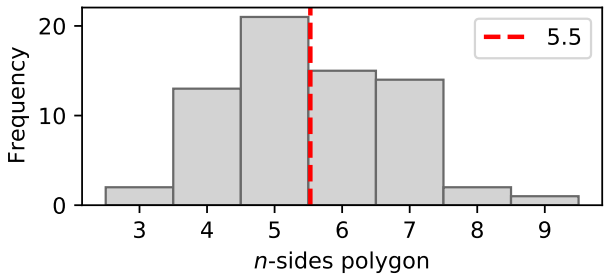

Figure 5.1: Polygons size distribution of the experimental tissue. Red dashed line (and legend) indicates the mean value.

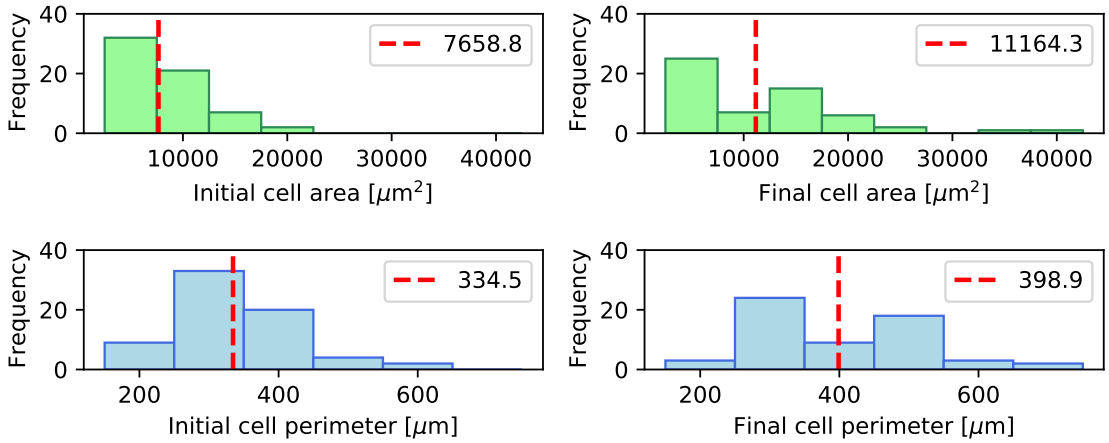

Figure 5.2: Up: experimental distribution of the cell areas at $t = 48$ hpf (left) and at $t = 58$ hpf (right). Bottom: experimental distribution of the cell perimeters at $t = 48$ hpf (left) and at $t = 58$ hpf (right). Red dashed lines (and legends) indicate the mean values of each quantity.

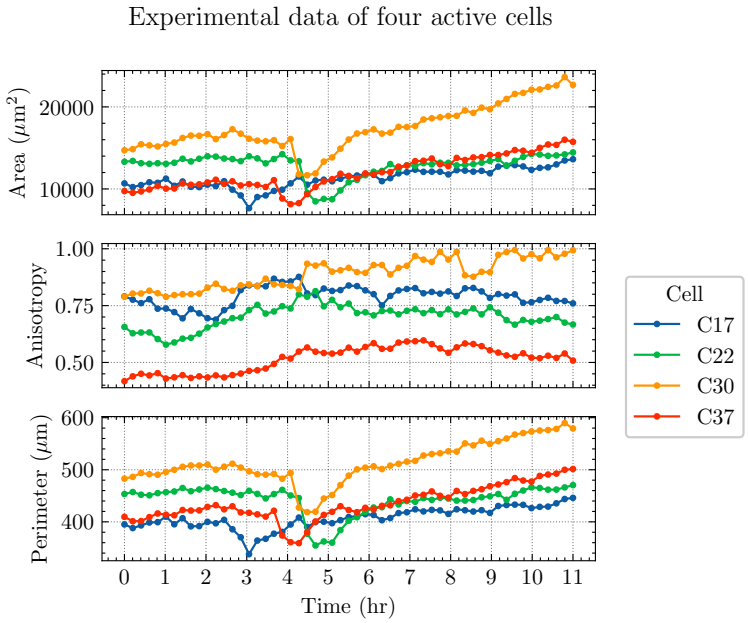

Figure 5.3: Experimental evolution of the area, anisotropy and perimeter of four cells that suffer active contraction during the pre-epiboly. Time 0 means the beginning of the experiment: 48 hpf.

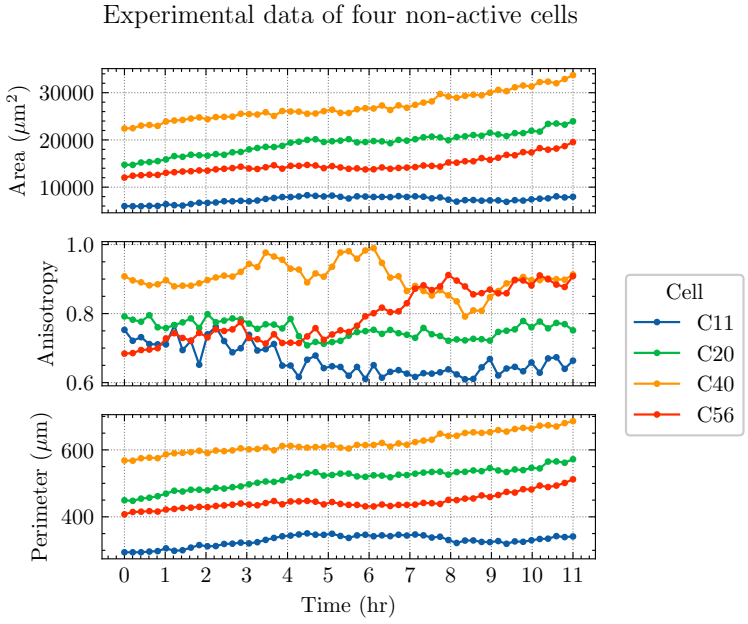

Figure 5.4: Experimental evolution of the area, anisotropy and perimeter of four cells that do not suffer active contraction during the pre-epiboly. Time 0 means the beginning of the experiment: 48 hpf.

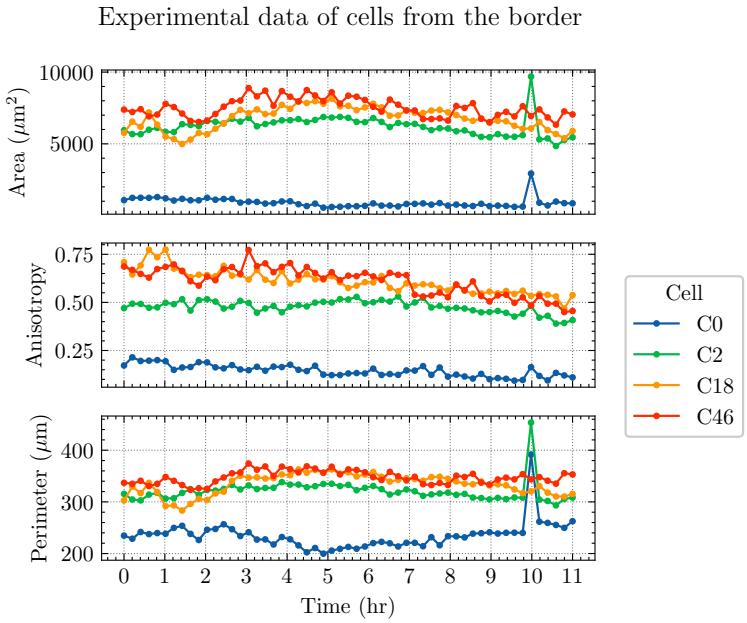

Figure 5.5: Experimental evolution of the area, anisotropy and perimeter of four cells at the border that do not suffer active contraction during the pre-epiboly. Time 0 means the beginning of the experiment: 48 hpf.

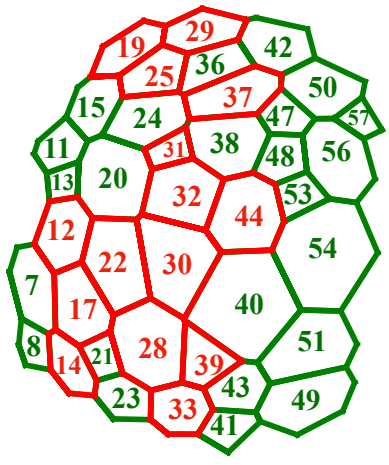

Figure 5.6: Effective tissue that we use in the numerical analysis, composed of 39 cells. 15 cells are active and 24 are non-active. Numbers correspond to the label of each cell in the numerical simulations. Red cells suffer contractile active events in the pre-epiboly stage.

5.2 Computational model

5.2.1 Vertex model geometrically constrained

Since the thickness of each cell is much less than the mean cell side, $h \ll l_0$, the apical two-dimensional vertex model is a good representation of the entire system. We consider the initial value of the equilibrium parameters given by the geometry in the initial time, i.e, $A_{0c}(t=0) = A_c(t=0)$ and $P_{0c}(t=0) = P_c(t=0)$. Since we want the initial configuration to be the one in equilibrium, we keep $J = 0$ (the adhesion term). Then, the energy functional that we use, for the effective tissue of 39 cells, is

$$E = \frac{K_A}{2}\sum_{c=1}^{39}(A_c - A_{0c})^2 + \frac{K_P}{2}\sum_{c=1}^{39}(P_c - P_{0c})^2, \tag{5.1}$$

where K_A and K_J play the roles already described in Ch. 1. The two term considers sums over all the cells.

The non-planar vertex model usually assume an extra bending energy cost given by

$$E_b = K_B \sum_{\langle c,c'\rangle} \left(1 - \hat{\mathbf{n}}_c \cdot \hat{\mathbf{n}}_{c'}\right), \tag{5.2}$$

where the sum run over all the adjacent cells c and c', with $\hat{\mathbf{n}}_c$ and $\hat{\mathbf{n}}_{c'}$ the respective normal vectors. However, we show a simple analysis that tells us $E_b \to 0$ in our system. The dot product between the normal vectors is equal to $\cos(\theta_{c,c'})$, with this angle being the one between the two center vectors $\mathbf{R}_c$ and $\mathbf{R}_{c'}$. Assuming the centers are at distance $\mathrm{d}_{c,c'} = 2l_0$, and hence $\mathrm{d}_{c,c'} \ll R$, the previous angle is small, $\theta_{c,c'} \ll 1$. Then, $\cos(\theta_{c,c'}) \approx 1 - \theta_{c,c'}^2/2$. Finally, since $\mathrm{d}_{c,c'} = R\theta_{c,c'}$ we obtain the following relation

$$\hat{\mathbf{n}}_c \cdot \hat{\mathbf{n}}_{c'} \approx 1 - \frac{1}{2}\left(\frac{\mathrm{d}_{c,c'}}{R}\right)^2 \to 1. \tag{5.3}$$

Then, going back to Eq. (5.2), we can see this extra term is negligible in our system.

The equations of motion are obtained variationally, using the positions of the apical vertices $\mathbf{r}_\mathrm{i}$. Since in this experiment the tissue is over a spherical surface with radius $R = 590\mu$m, we use the Lagrange method considering the restriction $c = R/|\mathbf{r}_\mathrm{i}| - 1 = R/r_\mathrm{i} - 1$, and λ as the Lagrange multiplier, such that

$$\frac{\mathrm{d}\mathbf{r}_\mathrm{i}}{\mathrm{d}t} = -\frac{\partial E}{\partial \mathbf{r}_\mathrm{i}} - \lambda\frac{\partial c}{\partial \mathbf{r}_\mathrm{i}}, \tag{5.4}$$

$$\frac{\mathrm{d}c}{\mathrm{d}t} = \frac{\partial c}{\partial t} + \frac{\partial c}{\partial \mathbf{r}_\mathrm{i}} \cdot \frac{\mathrm{d}\mathbf{r}_\mathrm{i}}{\mathrm{d}t} = 0, \tag{5.5}$$

$$\frac{\partial c}{\partial \mathbf{r}_\mathrm{i}} = -\frac{R}{r_\mathrm{i}^2}\hat{\mathbf{r}}_\mathrm{i}. \tag{5.6}$$

From Eq. (5.5) we can see $\frac{\partial c}{\partial \mathbf{r}_\mathrm{i}}$ and $\frac{\mathrm{d}\mathbf{r}_\mathrm{i}}{\mathrm{d}t}$ are orthogonal. Multiplying Eq. (5.4) by $\frac{\partial c}{\partial \mathbf{r}_\mathrm{i}}$, it follows that

$$0 = -\frac{\partial E}{\partial \mathbf{r}_\mathrm{i}} \cdot \frac{\partial c}{\partial \mathbf{r}_\mathrm{i}} - \lambda \left(\frac{\partial c}{\partial \mathbf{r}_\mathrm{i}} \right)^2, \tag{5.7}$$

$$\lambda = \frac{-\frac{\partial E}{\partial \mathbf{r}_\mathrm{i}} \cdot \frac{\partial c}{\partial \mathbf{r}_\mathrm{i}}}{\left(\frac{\partial c}{\partial \mathbf{r}_\mathrm{i}} \right)^2}. \tag{5.8}$$

Replacing Eq. (5.6) in Eq. (5.8), we obtain

$$\lambda = \frac{\frac{R}{r_\mathrm{i}^2} \frac{\partial E}{\partial \mathbf{r}_\mathrm{i}} \cdot \hat{\mathbf{r}}_\mathrm{i}}{\frac{R^2}{r_\mathrm{i}^4}} = \frac{r_\mathrm{i}^2}{R} \frac{\partial E}{\partial \mathbf{r}_\mathrm{i}} \cdot \hat{\mathbf{r}}_\mathrm{i}. \tag{5.9}$$

Finally, the equation of motions are given by

$$\frac{\mathrm{d}\mathbf{r}_\mathrm{i}}{\mathrm{d}t} = -\frac{\partial E}{\partial \mathbf{r}_\mathrm{i}} + \left(\frac{\partial E}{\partial \mathbf{r}_\mathrm{i}} \cdot \hat{\mathbf{r}}_\mathrm{i} \right) \hat{\mathbf{r}}_\mathrm{i}. \tag{5.10}$$

Considering the Euler method of integration in the numerical simulations, we obtain the positions in the step $N+1$ as a function of the position in the previous step N,

$$\mathbf{r}_\mathrm{i}^{(N+1)} = \mathbf{r}_\mathrm{i}^{(N)} - \frac{\partial E}{\partial \mathbf{r}_\mathrm{i}^{(N)}} \Delta t + \left(\frac{\partial E}{\partial \mathbf{r}_\mathrm{i}^{(N)}} \cdot \hat{\mathbf{r}}_\mathrm{i}^{(N)} \right) \hat{\mathbf{r}}_\mathrm{i}^{(N)} \Delta t, \tag{5.11}$$

where $\mathbf{r}_\mathrm{i}^{(N)} = R\hat{\mathbf{r}}_\mathrm{i}^{(N)}$ and $\mathbf{r}_\mathrm{i}^{(N+1)} = R\hat{\mathbf{r}}_\mathrm{i}^{(N+1)}$.

However, if we consider Eq. (5.11) up to $O(\Delta t)$, and define

$$\widetilde{\mathbf{r}}_\mathbf{i}^{(N+1)} = \mathbf{r}_\mathrm{i}^{(N)} - \frac{\partial E}{\partial \mathbf{r}_\mathrm{i}^{(N)}} \Delta t, \tag{5.12}$$

which corresponds to the solution using the Euler method without considering the Lagrange multiplier, we obtain

$$\mathbf{r}_\mathrm{i}^{(N+1)} = R \frac{\widetilde{\mathbf{r}}_\mathbf{i}^{(N+1)}}{\widetilde{r}_\mathrm{i}^{(N+1)}}, \tag{5.13}$$

which is the form implemented in the numerical simulations.

5.2.2 Pre-epiboly cellular rearrangements and active contraction pulses

Motivated on the evolution of the area and perimeter of some cells after the active contraction events, as for example cell C17 in Fig. 5.3, we include plasticity in the model. The plasticity and activity enters as discussed in Ch. 2. Then, the equilibrium parameters of each cell (A_{0c} and P_{0c}) relax plastically towards the instantaneous values (A_c and P_c).

From the experimental data we see that the evolution of the areas and perimeters is approximately linear (Fig. 5.4). Then, a natural guess for the evolution of the equilibrium parameters is also linear,

$$\begin{aligned} A_{0c}(t=0) &\approx A_{0c}(t=0)(1+m_A t), \\ P_{0c}(t=0) &\approx P_{0c}(t=0)(1+m_P t), \end{aligned} \tag{5.14}$$

where m_A and m_P account for the expansion due to the decrease of the cellular height.

Hence, the equations for the evolution of the equilibrium areas and perimeters are given by

$$\frac{\mathrm{d}A_{0c}}{\mathrm{d}t} = -\nu_A \left(A_{0c} - A_c\right) + f_{A_c}(t) + A_{0c}(t=0)m_A, \tag{5.15}$$

$$\frac{\mathrm{d}P_{0c}}{\mathrm{d}t} = -\nu_P \left(P_{0c} - P_c\right) + f_{P_c}(t) + P_{0c}(t=0)m_P, \tag{5.16}$$

with the active functions f_{A_c} and f_{P_c} as combinations of sinusoidal functions in the active time interval as described in Sec. 2.4:

$$f(t) = \begin{cases} 0 & , \text{if } t < t_0 \text{ and } t > t_0 + \delta_1 + \delta_2 \\ -C_1 \sin\left(\pi\left(t - t_0\right)/\delta_1\right) & , \text{if } t > t_0 \text{ and } t < t_0 + \delta_1 \\ C_2 \sin\left(\pi\left(t - t_0 - \delta_1\right)/\delta_2\right) & , \text{if } t > t_0 + \delta_1 \text{ and } t < t_0 + \delta_1 + \delta_2 \end{cases} \tag{5.17}$$

We choose to use the fraction $\delta = \delta_1/(\delta_1 + \delta_2)$, where δ_1 and δ_2 are the duration of the destruction and creation of cellular structural material phases, to describe an active pulse.

5.3 Fist stage of optimization: pseudo-passive system

First, we simulate the pre-epiboly of the tissue with the evolutiion of the vertices of the active cells and those on the border of the analyzed portion given by the experimental measures. Hence, only the black vertices in Fig. 5.7-A are free to move following the dynamic of the vertex model geometrically constrained. Then, in this first stage of the optimization we do not consider the active functions f_{A_c} and f_{P_c}; we treat the system as a pseudo-passive tissue (we do consider the expansion of the tissue due to the change in the cellular height). We perform an optimization that allows us to get first values for some parameters of the model, as will be explained in the following.

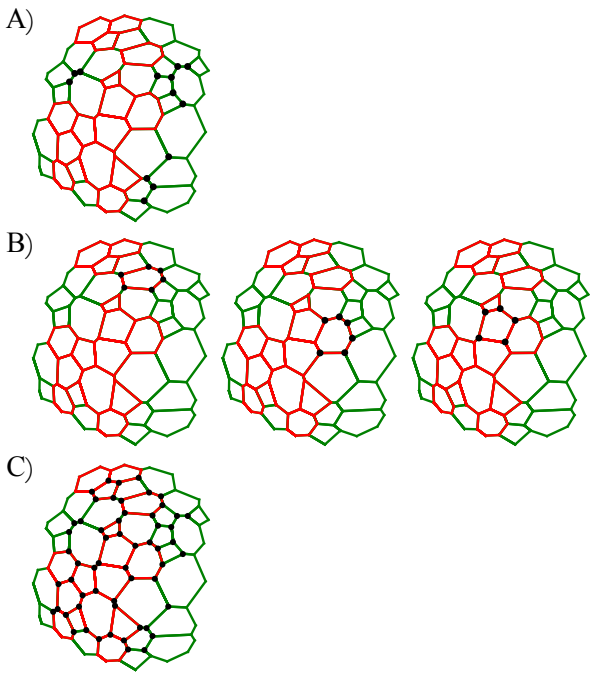

Figure 5.7: Effective tissue composed of 39 cells used in the optimisation process. In black color we show the vertices that are free to move following Eqs. (A.2), while the rest of the vertices move following the experimental data. A) First optimisation processes that helps to find an initial guess of the passive parameters. B) Active-cell-by-active-cell optimisations. C) Last optimisation considering the simplified model.

We define the dimensionless parameter $p = K_P/(K_A l_0^2)$, as in Ch. 3. Also, we consider $\tau_A = 1/(K_A l_0^2) \sim 1\text{h}$, with $l_0 = 50\mu\text{m}$, and $p \in [0, 5]$. In the simulations we let $1/\tau_A \in [0\text{h}^{-1}, 5\text{h}^{-1}]$, too. That way, the three relaxation rates associated to each elastic parameter have similar values, and we will be working on similar ranges that in previous chapters. For the plasticity parameters, we estimate values $\sim 1\text{h}^{-1}$, since the active events take times of the order of $\sim 1\text{h}$ (Fig. 5.3). Finally, for the seed values of the rearrangement parameters we choose 0.05h^{-1} and 0.1h^{-1} for m_A, and $m_P = m_A/2$, given that both areas and perimeters evolve in a linear way experimentally, and then m_P should be smaller than m_A.

More specifically, the seed values for the parameters of the model, all of them in h^{-1}, are

$$\begin{aligned} K_A l_0^2 &= [1, 2, 3, 4, 5]\,, \\ K_P &= [1, 2, 3, 4, 5]\,, \\ \nu_A &= [0.2, 0.7, 1.2]\,, \\ \nu_P &= [0.2, 0.7, 1.2]\,, \\ m_A &= [0.05, 0.1]\,, \\ m_P &= m_A/2. \end{aligned} \tag{5.18}$$

We use these seeds to create 450 different sets of parameters called *initial conditions*. We use each of these initial conditions as starter parameters to model the pre-epiboly following the procedure specified in the Sec. 5.2, using a time step $\Delta t = 0.01$, for the numerical integration. We have learned from previous chapters that the achieved cellular geometry (area, anisotropy)

varies depending on the localization of the cellular activity. In this particular case we use two observables: the cellular area and the cellular perimeter. We choose to use the perimeter instead of the anisotropy due to their smoother behavior (see Figs. 5.3, 5.4 and 5.5).

For each set of *initial conditions* we follow the next steps:

Step 1 We simulate the pre-epiboly using a set of *initial conditions* and save the geometrical information of the cells (areas and perimeters) every $20\Delta t$, to compare with the experimental data. For that, we define the functions

$$\Delta A = \sum_{t=1}^{n_t=55} \sum_{c=1}^{n_c=24} \frac{\left(A_c^{\text{sim}} - A_c^{\text{exp}}\right)^2}{n_t n_c \bar{A}^2}, \tag{5.19}$$

$$\Delta P = \sum_{t=1}^{n_t=55} \sum_{c=1}^{n_c=24} \frac{\left(P_c^{\text{sim}} - P_c^{\text{exp}}\right)^2}{n_t n_c \bar{P}^2}, \tag{5.20}$$

where the first sum, in both expressions, is over the amount of data times to compare ($n_t = 55$) and the second sum, in both expressions, is over the 24 non-active cells of the effective tissue. $\bar{A} = 7658.8\mu\text{m}^2$ is the initial experimental mean cell area, and $\bar{P} = 334.5\mu\text{m}$ is the initial experimental mean cell perimeter (see Fig. 5.2). In the optimization code we use the functional OPT $= \Delta A + 6\Delta P$, where the factor 6 was chosen such that both terms have similar importance.

Step 2 We vary the parameters $K_A l_0^2, K_P, \nu_A, \nu_P, m_A$ as $\gamma \to \gamma' = \gamma(1 + 0.1\xi)$, and m_P as $m_P \to m_A'(1 + 0.5\xi)$, with ξ a random number between -1 and 1, chosen from a uniform distribution. We simulate the pre-epiboly using the new set of parameters, and calculate the new value of OPT$\to$ OPT$'$. If OPT$' >$ OPT, situation called *failure*, we come back to the previous set of parameters; if OPT$' <$ OPT, situation called *success*, we save the new values.

Step 3 We repeat **Step 2** 200 times.

From all the simulations ($90450 = 450$ *initial conditions* $\times 201$ simulations of pre-epiboly characterized as *success* or *failure*), 2148 are *successes*. From Fig. 5.8 we can see there is no preference for a particular region of the parameter of space. It is important to note that we force the system to choose m_P always smaller than m_A; it is not a result from the optimization. From this analysis we do not get a meaningful best set of parameters, but we do obtain an initial set that will act as a seed to perform other optimizations. It is important to remember that the plasticity is specially observed in the cellular geometrical evolution during the active contractions, hence we expect ν_A and ν_P to change when studying the active events. The minimum value of OPT is obtained with

$$\left[K_A l_0^2, K_P, \nu_A, \nu_P, m_A, m_P\right] = \left[5.75, 5.16, 0.72, 1.14, 0.05, 0.01\right]. \tag{5.21}$$

5.4 Second stage of optimization: active events

In this stage we let free, as degrees of freedom, only the vertices that belong to one particular active cell (black vertices in Fig. 5.7-B) and the positions of all the other vertices are fixed

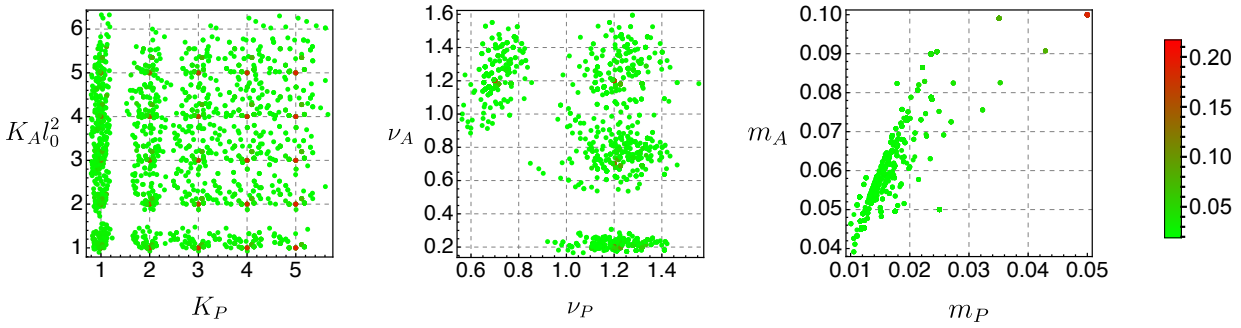

Figure 5.8: Results of the first stage of optimization. The color corresponds to the value of OPT for the 2148 successes (of 90450 total simulations).

to the experimental values. We search the best parameters that reproduce the active event when considering medial activity (f_{A_c} , but no f_{P_c}) or perimeter activity (f_{Pc} , but no f_{A_c}). In both cases, we fix initially, by looking at the experimental curves, the initial time t_0 of the active functions and the total duration of the pulse $\delta_T = \delta_1 + \delta_2$. We perform the procedure for c={C37, C44, C32}, which are the cases shown in Fig. 5.7-B. During this stage of optimization we keep fix $[K_A l_0^2, K_P, m_A, m_P] = [5.75, 5.16, 0.05, 0.01]$, and optimize ν_A and ν_P (global parameters), and $C_1^{\rm c}$ and $\delta^{\rm c}$ (for each cell from the set c).

5.4.1 Active cell C37

The cell C37 is the only active one surrounded entirely by non-active cells. That is the reason why we choose it as the first active cell to study. During these simulations the cell C37 is complete free, the cells C24, C36, C42, C50, C47, and C38 are half-free, and the rest follow the experimental evolution. We fix $t_0^{\rm C37} = 3.3$ and $\delta_1^{\rm C37} + \delta_2^{\rm C37} = 1.6$, by looking at the experimental curve of the cell C37 (Fig. 5.9).

We create 20 *initial conditions*, starting from $\left[\nu_A = 0.72, \nu_P = 1.14, C_1^{\rm C37} = 1, \delta^{\rm C37} = 0.5\right]$, varying each parameter 20 times as $\gamma \to \gamma(1 + 0.05\xi)$, where ξ is a random number between -1 and 1, chosen from a uniform distribution.

For each set of *initial conditions* we follow the next steps, first considering medial activity (f_{A_c} , but no f_{P_c}), and later considering perimeter activity (f_{Pc} , but no f_{A_c}):

Step 1 We simulate the pre-epiboly using the fix parameters described before and a set of *initial conditions*, and save the geometrical information of the cells (areas and perimeters) every $20\Delta t$, to compare with the experimental data. For that, we use the Eqs. (5.20), where now we use $n_c = 7$ (1 free cell + 6 half-free cells). Again, in the optimization code we use the functional OPT $= \Delta A + 6\Delta P$.

Step 2 We vary the parameters $\nu_A, \nu_P, C_1^{\rm C37}, \delta^{\rm C37}$ as $\gamma \to \gamma' = \gamma(1 + 0.05\xi)$, with ξ a random number between -1 and 1, chosen from a uniform distribution. We simulate the pre-epiboly using the new set of parameters, and calculate the new value of OPT$\to$ OPT$'$. If OPT$'$ > OPT, situation called *failure*, we come back to the previous set of parameters; if OPT$'$ < OPT, situation called *success*, we save the new values.

Step 3 We repeat **Step 2** 500 times.

The results of the numerical optimization for each case of activity (medial or inner perimeter) are presented in Fig. 5.10. We obtain that for both kind of activities, the minimum values of OPT are obtained with $\nu_A > \nu_P$. With respect to the amplitude C_1^{C37} and the fraction of time of destruction of material δ^{C37}, in average there is not relevant changes form the initial condition in the case of medial activity. Instead, for inner perimeter activity, the amplitud decrease $\sim 30\%$. The lowest value of OPT for each kind of activity are achieved with the following sets of parameters

$$\text{Medial activity:} \quad \left[\nu_A, \nu_P, C_1^{\mathrm{C37}}, \delta^{\mathrm{C37}}\right] = [1.02, 0.27, 1.02, 0.47]\,, \tag{5.22}$$

$$\text{Inner perimeter activity:} \quad \left[\nu_A, \nu_P, C_1^{\mathrm{C37}}, \delta^{\mathrm{C37}}\right] = [1.31, 0.26, 0.72, 0.46]\,. \tag{5.23}$$

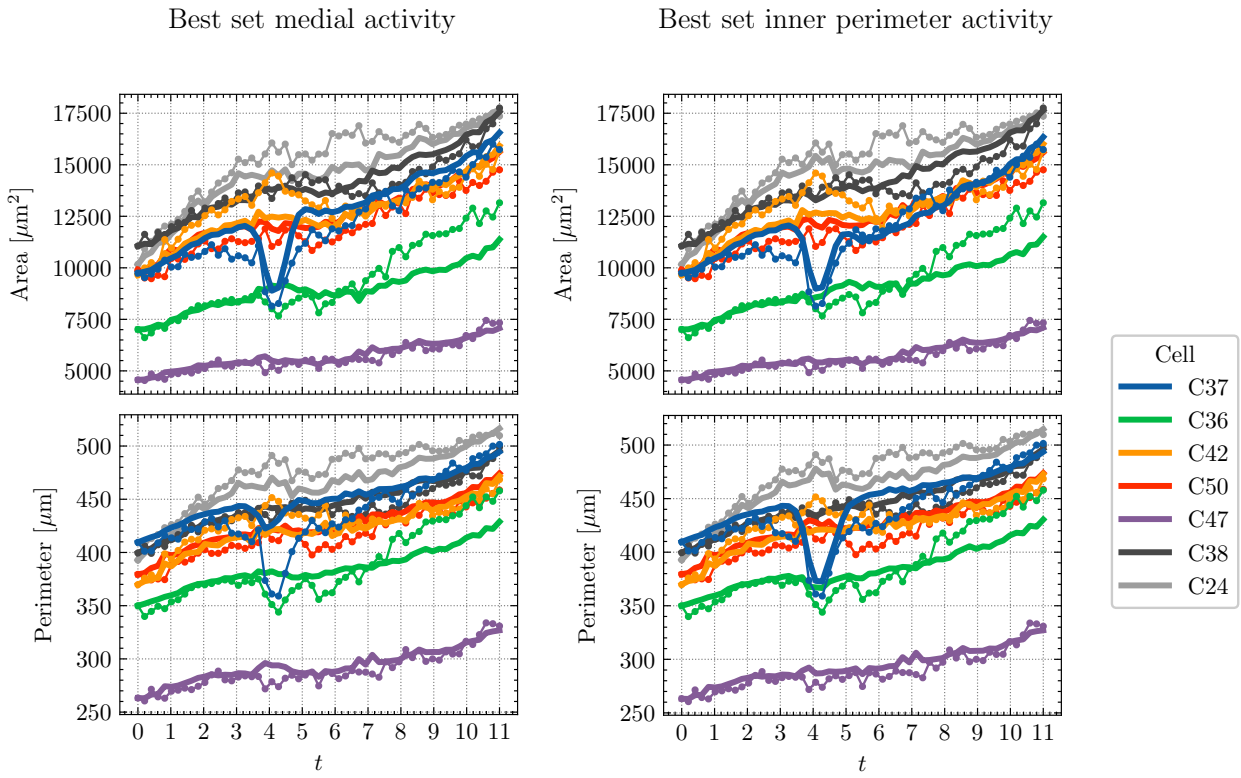

Figure 5.9: Evolution of the numerical (thick line) and experimental (thin line with points) area and perimeter of the active cell C37 and its neighbors C36, C42, C50, C47, C38, and C24, when simulating the pre-epiboly letting free, as degrees of freedom, only the vertices that belong to the cell C37. Left: medial activity (Eq. (5.22)). Right: inner perimeter activity (Eq. (5.23)).

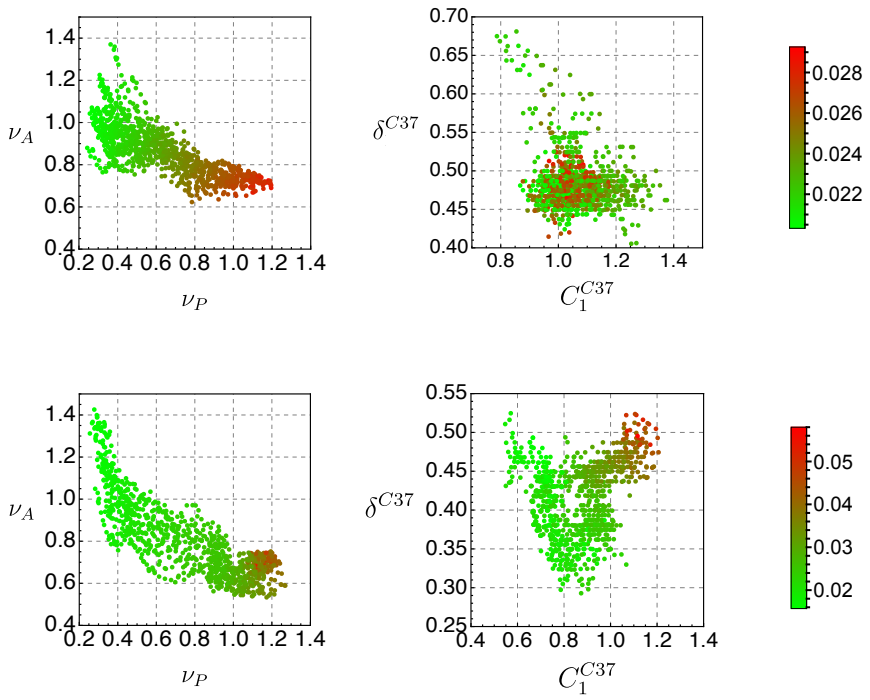

Figure 5.10: Results of the second stage of optimization for the active cell C37. Up: medial activity. Bottom: inner perimeter activity. The color corresponds to the value of OPT for the 1049 (up) and 964 (bottom) successes (of 10020 total simulations).

Figure 5.9 shows the numerical and experimental evolution of the area and perimeter of the cell C37 and its neighbors for both sets of parameters (Eqs. (5.22) and (5.23)). We obtain that inner perimeter activity produces a geometrical evolution of the active cell very close to the experimental data. Instead, medial activity is capable of achieving a similar area contraction, however the perimeter does not evolve as in the experiment. This observation is in direct relation with the results of Ch. 4, i.e., large enough amplitude C_1^{C37} may produce the expected area contraction accompanied by the increase of the anisotropy of the cellular shape. The fact that the best set is with inner perimeter activity, with ν_A one order of magnitude larger than ν_P, is also in concordance with the results of Ch. 4, since we showed that this combination is the one that achieves the major area contraction with the minor change of anisotropy.

5.4.2 Active cell C44

After the analysis of the only active cell surrounded by non-active ones, we proceed to analyze the active cell C44 because it is surrounded by five non-active cells and two active cells. However, the active contraction events of the cells C30 and C32 have already finished by the time C44 starts its own contraction, as can be seen in Fig. 5.11. We perform the same procedure already described for the study of the active event of C37. However, this time we consider two different seeds from where we create the 20 *initial conditions*, depending on the localization of the activity. The seeds for C_1^{C44} and δ^{C44} are chosen by a previous hand testing. For medial activity the seed is $\left[\nu_A = 1.02, \nu_P = 0.27, C_1^{\mathrm{C44}} = 1.75, \delta^{\mathrm{C37}} = 0.5\right]$. For inner perimeter activity the seed is $\left[\nu_A = 1.31, \nu_P = 0.26, C_1^{\mathrm{C44}} = 1.4, \delta^{\mathrm{C37}} = 0.5\right]$. We fix $t_0^{\mathrm{C44}} = 7.6$ and $\delta_1^{\mathrm{C44}} + \delta_2^{\mathrm{C44}} = 1.8$, by looking at the experimental curve of the cell C37

(Fig. 5.11).

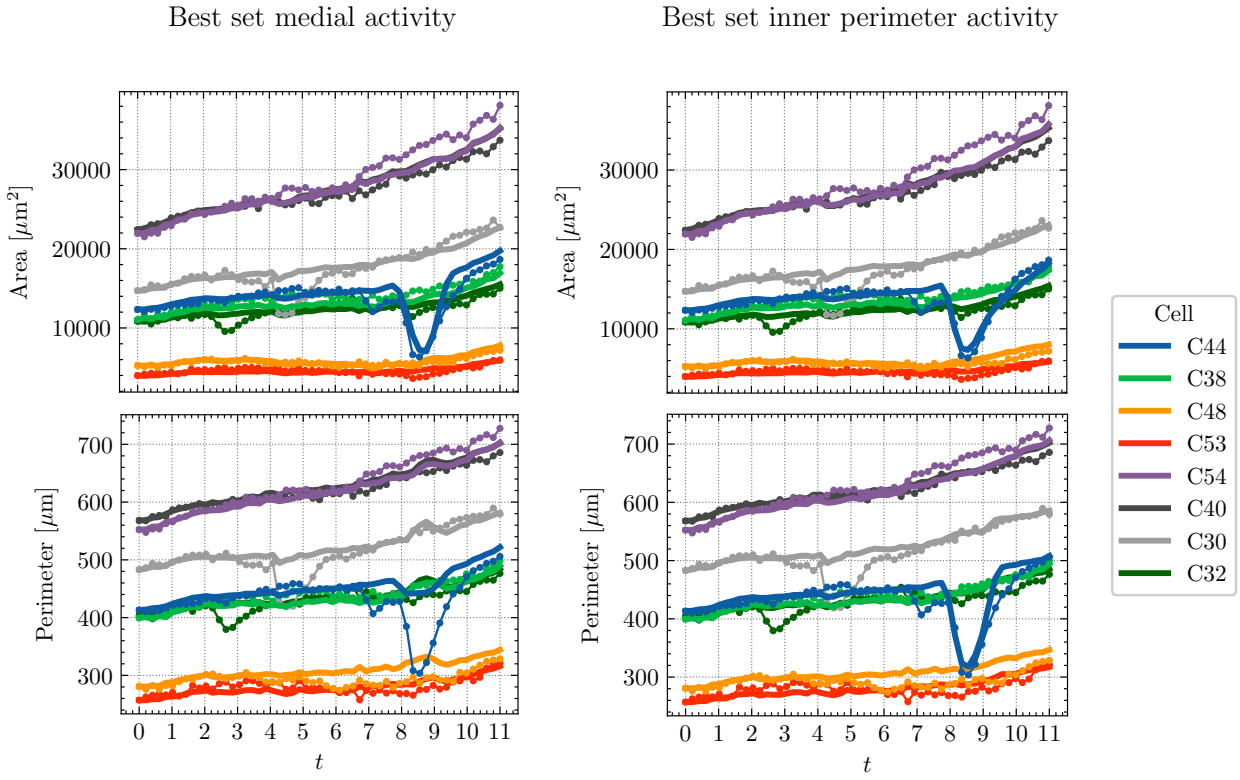

Figure 5.11: Evolution of the numerical (thick line) and experimental (thin line with points) area and perimeter of the active cell C44 and its neighbors C38, C48, C53, C54, C40 , C30, and C32, when simulating the pre-epiboly using the effective tissue with the motion of the vertices given by the experimental values except for the ones that form the cell C44. Left: medial activity (Eq. (5.24)). Right: inner perimeter activity (Eq. (5.25)).

Figure 5.12 shows the results of the optimizations. We obtain that for both kind of activities the plasticity parameters increase, maintaining the relation $\nu_A > \nu_P$. With respect to the amplitude C_1^{C44} and the time of destruction of material δ_1^{C44}, in average there is not relevant changes form the initial condition in the case of medial activity. Instead, for inner perimeter activity, C_1^{C44} increases while δ_1^{C44} decreases. The lowest value of OPT for each kind of activity are achieved with the following sets of parameters

$$\text{Medial activity:} \quad \left[\nu_A, \nu_P, C_1^{\mathrm{C44}}, \delta^{\mathrm{C44}}\right] = [2.16, 1.63, 1.54, 0.53]\,, \tag{5.24}$$

$$\text{Inner perimeter activity:} \quad \left[\nu_A, \nu_P, C_1^{\mathrm{C44}}, \delta^{\mathrm{C44}}\right] = [4.15, 0.82, 1.63, 0.31]\,. \tag{5.25}$$

Figure 5.11 shows the numerical and experimental evolution of the area and perimeter of the cell C44 and its neighbors for the both previous sets of parameters. Just as in the case

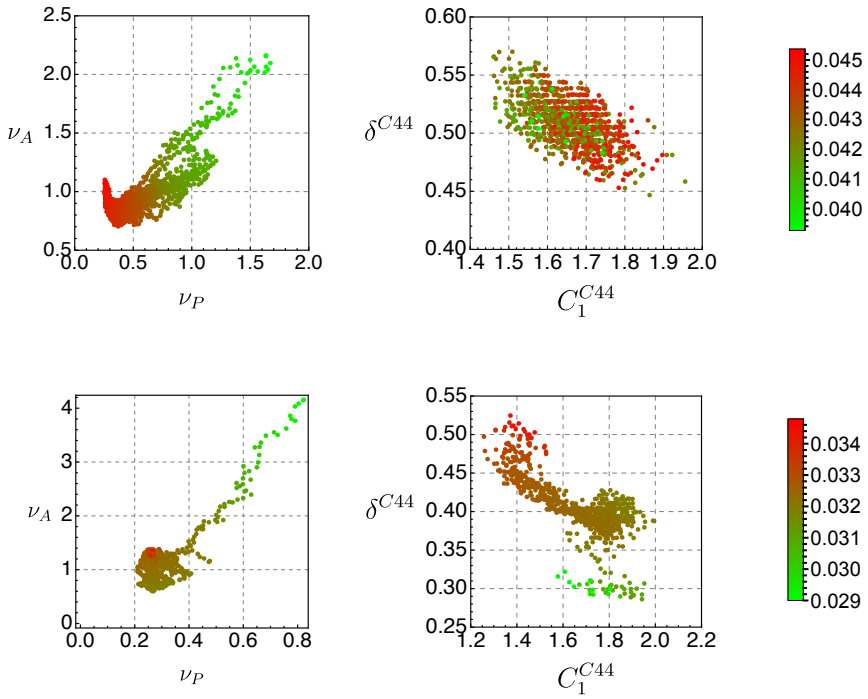

Figure 5.12: Results of the second stage of optimization for the active cell C44. Up: medial activity. Bottom: inner perimeter activity. The color corresponds to the value of OPT for the 1158 (up) and 670 (bottom) successes (of 10020 total simulations).

of C37, we obtain that inner perimeter activity generates good geometrical evolutions, both of area and perimeter, while medial activity is not capable of modeling the experimental behavior of the perimeter.

5.4.3 Active cell C32

We choose one more cell, C32, to compare both optimizations using medial and inner perimeter cellular activity. This time, the seeds are $\left[\nu_A = 2.16, \nu_P = 1.63, C_1^{\mathrm{C32}} = 0.8, \delta^{\mathrm{C32}} = 0.5\right]$, for medial activity, and $\left[\nu_A = 4.15, \nu_P = 0.82, C_1^{\mathrm{C32}} = 0.45, \delta^{\mathrm{C32}} = 0.5\right]$, for perimeter activity. We fix $t_0^{\mathrm{C32}} = 2.0$ and $\delta_1^{\mathrm{C32}} + \delta_2^{\mathrm{C32}} = 1.4$, by looking at the experimental curve of the cell C37 (Fig. 5.13).

Figure 5.14 shows the results of the optimizations. We obtain that for both kind of activities the plasticity parameters decrease, maintaining the relation $\nu_A > \nu_P$. With respect to the amplitude C_1^{C44} and the fraction of time of destruction of material δ^{C44}, in average there is not relevant changes form the initial condition in both cases. The lowest value of OPT for each kind of activity are achieved with the following sets of parameters

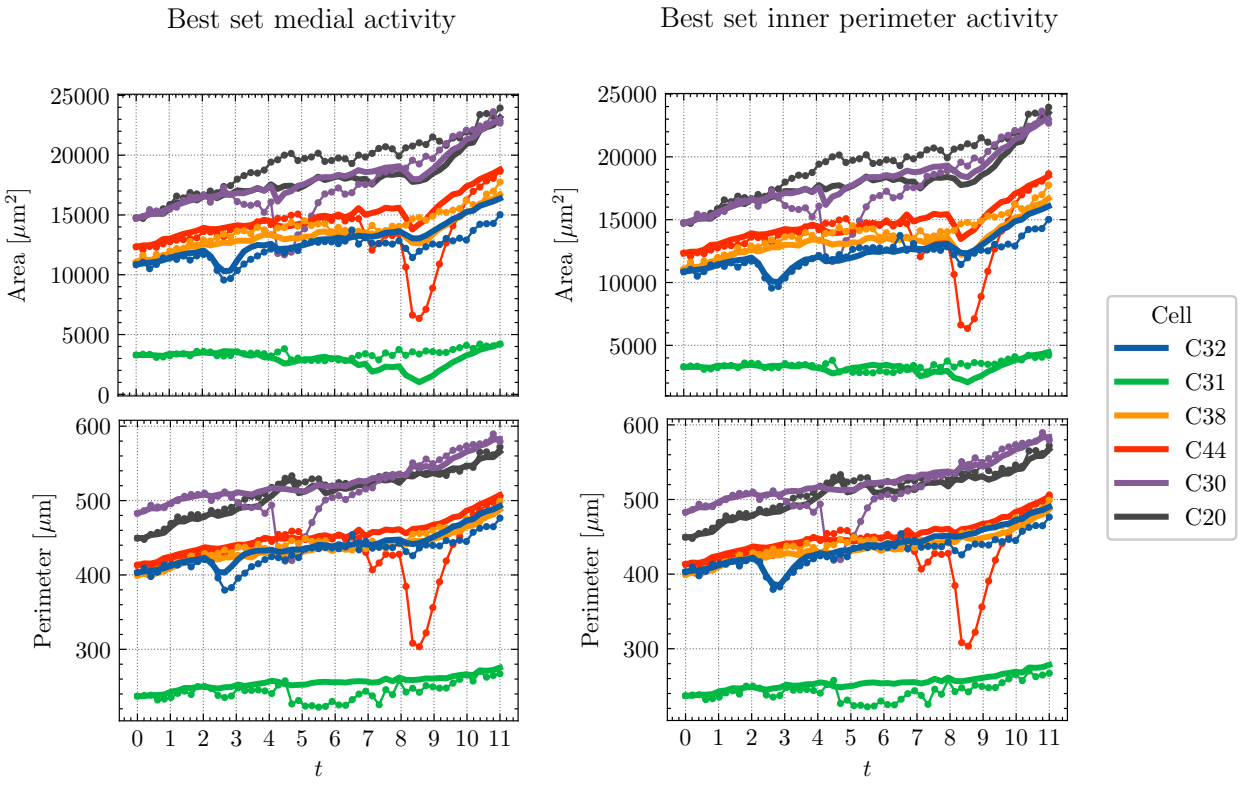

Figure 5.13: Evolution of the numerical (thick line) and experimental (thin line with points) area and perimeter of the active cell C32 and its neighbors C31, C38, C44, C30, and C20, when simulating the pre-epiboly using the effective tissue with the motion of the vertices given by the experimental values except for the ones that form the cell C44. Left: medial activity (Eq. (5.26)). Right: inner perimeter activity (Eq. (5.27)).

$$\text{Medial activity:} \quad \left[\nu_A, \nu_P, C_1^{\text{C32}}, \delta^{\text{C32}}\right] = [2.13, 0.97, 0.67, 0.46]\,, \tag{5.26}$$

$$\text{Inner perimeter activity:} \quad \left[\nu_A, \nu_P, C_1^{\text{C32}}, \delta^{\text{C32}}\right] = [4.08, 0.37, 0.37, 0.44]\,. \tag{5.27}$$

Figure 5.13 shows the numerical and experimental evolution of the area and perimeter of the cell C32 and its neighbors for the both previous sets of parameters. Just as in the case of C37 and C44, we obtain that inner perimeter activity generates good geometrical evolutions, both of area and perimeter, while medial activity is not capable of modeling the experimental behavior of the perimeter.

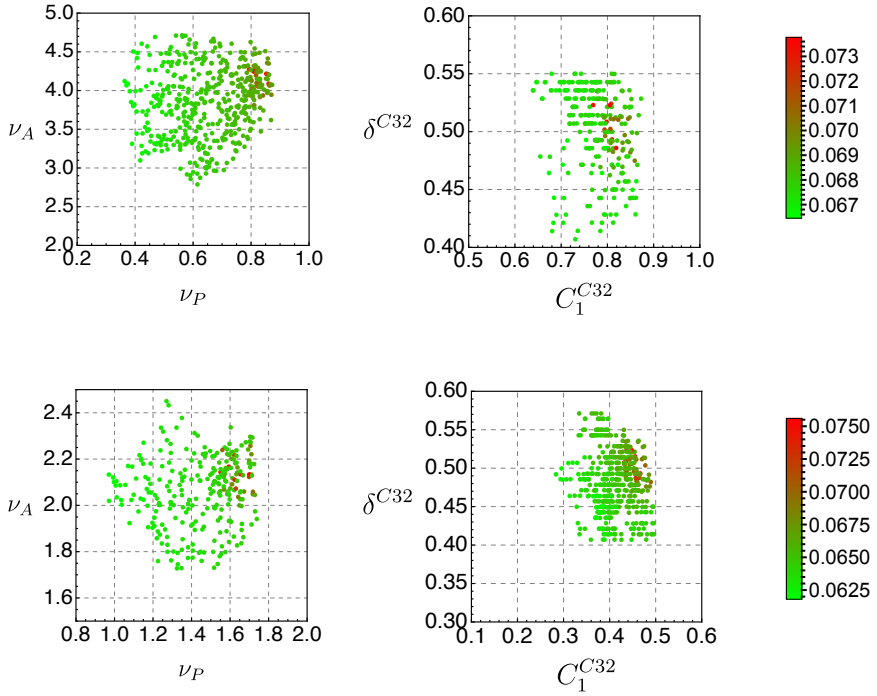

Figure 5.14: Results of the second stage of optimization for the active cell C32. Up: medial activity. Bottom: inner perimeter activity. The color corresponds to the value of OPT for the 273 (up) and 479 (bottom) successes (of 10020 total simulations).

5.4.4 All active cells

We have shown for three active cells C37, C44, and C32, that activity in the perimeter of equilibrium plus $\nu_A > \nu_P$ is needed in our model to achieve the experimental cellular geometry in the active events. We model the rest of the active cells following a similar procedure than before, just considering inner perimeter activity. We optimize several cells (adjacent) at the same time: (C19, C25, C19), (C12, C14, C17), (C28, C33, C39), (C22, C30) and (C31).

An important note is that cells C14, C39 and C31 take a long time in coming back to the size they had before the apical constriction. Given that experimental observation, the seed value for their fraction of time of destruction of perimeter material is set to 0.05.

We find that in almost all the cases the values of plasticity stay close to $\nu_A \sim 3.5$ and $\nu_P \sim 0.5$, except for the case of C31, in which the best values are 0.49 and 0.01, respectively.

Then, we simulate the pre-epiboly with the previously obtained parameters for all the active pulses, considering the vertices from the active cells as free ones (degrees of freedom), and using $\nu_A = 3.5$ and $\nu_P = 0.5$. In this simulation the cell C44, which performs the bigger constriction, suffers a big change of anisotropy making the polygon non-convex by the end of the active event. Others cells also go through non-convex shapes. This problem is solved by setting $\nu_P = 0$ and $m_P = 0$.

5.5 Third stage of optimization: Simplified model

All the previous considerations leave the dynamic equations of the equilibrium parameters as

$$\frac{\mathrm{d}A_{0c}}{\mathrm{d}t} = -\nu_A \left(A_{0c} - A_c\right) + A_{0c}(t=0)m_A, \tag{5.28}$$

$$\frac{\mathrm{d}P_{0c}}{\mathrm{d}t} = f_{P_c}(t). \tag{5.29}$$

Since by definition $f_{P_c}(t)$ is built to integrate zero, then this election satisfies no net variation of the perimeter of equilibrium.

Also, since most of the optimized values of δ are close to 0.5 (except for the tree cells C14, C39 and C31), we decide to fix $\delta = 0.5$ for all cells. Hence, f_{P_c} is modeled as a complete cycle of a unique sine function, allowing to reduce the number of parameters in the optimization.

Finally, we run a last optimization considering the above simplifications, and letting free all the inner vertices of the 39-cells effective tissue (black vertices in Fig. 5.7-C).

With the increment of the degrees of freedom and the changes described before, the previous active parameters are not the best ones one could use as seed. By inspection (modifying by hand) we obtain a set that generates a lower value of OPT. From this set, we create 10 initial conditions of the form $[K_A l_0^2, K_P, \nu_A, m_A]$, and perform an optimization process. We fix initially, by looking at the experimental curves, the initial time t_0 and the total duration $\delta_T = \delta_1 + \delta_2$, of each active event (see Tab. 5.1).

For each set of *initial conditions* we follow the next steps:

Step 1 We simulate the pre-epiboly using a set of *initial conditions* and save the geometrical information of the cells (areas and perimeters) every $20\Delta t$, to compare with the experimental data. For that, we use the Eqs. (5.20). Again, in the optimization code we use the functional $\mathrm{OPT} = \Delta A + 6\Delta P$.

Step 2 We vary the parameters $K_A l_0^2, K_P, m_A, \nu_A$ and all the amplitudes C_1, as $\gamma \to \gamma' = \gamma(1 + 0.1\xi)$, with ξ a random number between -1 and 1, chosen from a uniform distribution. We simulate the pre-epiboly using the new set of parameters, and calculate the new value of OPT$\to$ OPT$'$. If OPT$' >$ OPT, situation called *failure*, we come back to the previous set of parameters; if OPT$' <$ OPT, situation called *success*, we save the new values.

Step 3 We repeat **Step 2** 10000 times.

The global optimized parameters are $K_A l_0^2 = 6.25\,\mathrm{h}^{-1}$, $K_P = 4.82\,\mathrm{h}^{-1}$, $\nu_A = 3.20\,\mathrm{h}^{-1}$, and $m_A = 0.05\,\mathrm{h}^{-1}$, and the optimized amplitude C_1 for each pulse are given in Tab. 5.1. With the previous values we obtain $p = 0.77$, which correspond to a region in which the perimeter elasticity dominates. Also, the characteristic times of plasticity and elasticity are related by $\tau_{\nu_A} \sim 2\tau_{K_A} \sim 2\tau_{K_P} \sim 20\,\mathrm{min}$. Then, in this experiment the contractile events,

that have mean duration of 2.6 h, are considerable slow compared to the plastic and elastic characteristic times of the dynamic.

The geometrical evolution of the active cells are in Fig. 5.15.

Cell	t_0[h]	$(\delta_1 + \delta_2)$[h]	C_1[µm/h]
C12	0.40	3.00	0.19
C14	3.80	7.00	0.10
C17	2.00	2.00	0.44
C19	0.20	1.60	0.38
C22	3.60	2.10	0.53
C25	3.80	2.00	0.45
C28	0.00	2.00	0.33
C29	3.60	3.60	0.27
C30	3.50	1.80	0.62
C31	4.00	4.00	0.12
C32	2.00	1.20	0.43
C33	6.30	2.20	0.56
C37	3.20	1.60	0.75
C39	6.00	2.00	0.32
C44	6.80	2.50	0.67

Table 5.1: Parameters characterizing each pulse, where the perimeter active functions are given by $f_{P_c} = -C_1 \sin(2\pi(t - t_0)/\delta_T)$ for $0 \leq t - t_0 \leq \delta_T$. The start times t_0 and pulse durations δ_T are fixed by the experiments, while the pulse amplitudes C_1 are fitted to best reproduce the experimental evolution of the areas and perimeters.

The application of our modeling to the active contractile pulses extending through blastula stages of the annual killifish *A. nigripinnis* is highly illustrative. We were able to quantitatively fit the pulses of 15 cells with a reduced number of parameters (4 global parameters – K_A, K_P, ν_A, m_A – and 3 specifics parameters per cell – t_0, δ_T, C_1). It is important to recall that the values for t_0 and δ_T, for each active event, are fixed initially by looking at the experimental data, and are not optimized parameters. Also, the analysis showed that the pulses, in which cells contract keeping roughly isotropic shaped, and thus reducing both their areas and perimeters, are better described with activity only in the perimeter of the cells and plasticity on the areas. We recall that by comparing the cell areas and perimeters, which are simple geometrical observables that are easily accessible, it is possible to discriminate between the two possible sources of activity and, also, to fit all the relevant parameters. The presented methodology provides a practical and quantitative perspective of how apical constrictions occur in other systems. Also, offers a method to measure different parameter used in the vertex or similar models in many biological systems. It remains an interesting perspective to relate the measured parameters to the relevant biophysical processes taking place in the cells and tissues.

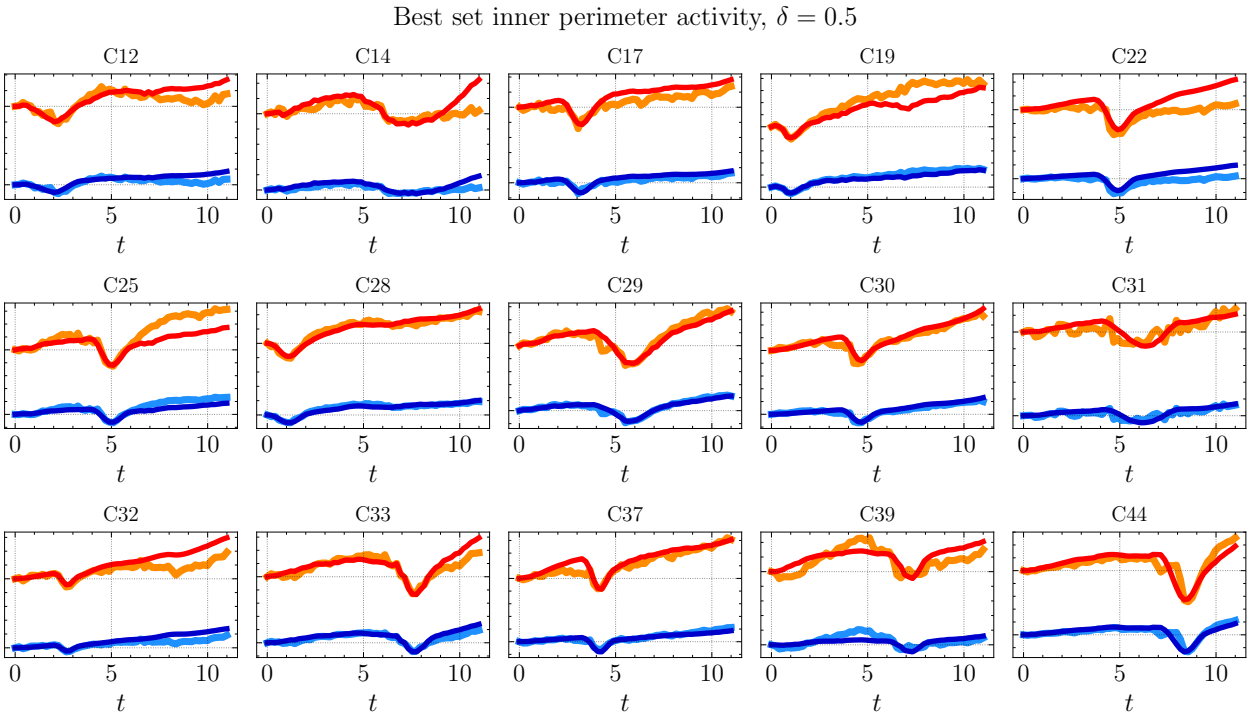

Figure 5.15: Geometrical evolution of the active cells in the pre-epiboly simulation using the active parameters from Tab. 5.1, with fix $\delta = 0.5, \nu_A = 3.20\text{h}^{-1}, \nu_P = 0\text{h}^{-1}, m_P = 0\text{h}^{-1}, m_A = 0.05\text{h}^{-1}, K_A l_0^2 = 6.25\text{h}^{-1}, K_P = 4.82\text{h}^{-1}$ for all the cells. For each cell, in red (orange) is shown the normalized numerical (experimental) area, and in blue (skyblue) is shown the normalized numerical (experimental) perimeter.

Chapter 6

From discrete to continuum

In this chapter we compare a discrete description using the vertex model, as in previous chapters, with a continuum one which use a texture tensor M as a field. In particular, we study the cases of an initially homogenous isotropic tissue with a Gaussian active region of different sizes. We compare some geometrical observables in the steady state between the continuum description and numerical simulations using ordered and low-disordered tissues. Also, we propose an equation to describe the temporal evolution of the system and show how it compares to the one obtained in the numerical simulations using the vertex model with an ordered tissue.

6.1 Discrete stress tensor

We begin by obtaining an expression for the mean stress of a tissue that is usually used in literature (see for example Ref. [77]). Starting from the functional energy of the vertex model

$$E = \sum_c \frac{K_A}{2} \left(A_c - A_{0c}\right)^2 + \frac{K_P}{2} \sum_c \left(P_c - P_{0c}\right)^2 + J \sum_{\langle \mathrm{i},j \rangle} l_{ij}, \tag{6.1}$$

one can obtain the equations of motion for a vertex with position $\mathbf{r}_\mathrm{i}$ (Eqs. (A.3), (A.13), (A.14), and (A.15)). This way, the force over a vertex i can be written as a sum of a force that appears due to each cell at which it belongs to, $\mathbf{f}_\mathrm{i} = \sum_c \mathbf{f}_\mathrm{i}^c$, with

$$\mathbf{f}_\mathrm{i}^c = \frac{K_A}{2} \left(A_c - A_{0c}\right) \left(\mathbf{r}_{\mathrm{i}_c-1,\mathrm{i}_c+1} \times \hat{\mathbf{z}}\right) + \left(K_P \left(P_c - P_{0c}\right) + \frac{J}{2}\right) \left(\frac{\mathbf{r}_{\mathrm{i}_c+1,\mathrm{i}}}{r_{\mathrm{i}_c+1,\mathrm{i}}} + \frac{\mathbf{r}_{\mathrm{i}_c-1,\mathrm{i}}}{r_{\mathrm{i}_c-1,\mathrm{i}}}\right), \tag{6.2}$$

where the vertices $\mathrm{i}_c + 1$ and $\mathrm{i}_c - 1$ correspond to the next and previous vertex to i, in clockwise counting, belonging to cell c. We can think the tissue as composed by two kind of particles – vertex-like and cellular-like particles – with no interaction between the vertices-like ones, and with $\mathbf{f}_\mathrm{i}^c$ being the force that the cellular-like particle c exerts on the vertex-like particle i. Then, noting that the evolution of the system relies entirely on the inter-particle

interactions, we can obtain an averaged in space single-cell stress tensor from kinetic theory (Ref. [78, p. 26]) given by

$$\sigma_c = -\frac{\sum_{\mathrm{i}} \mathbf{R}_{\mathrm{i}}{}^c \otimes \mathbf{f}_{\mathrm{i}}{}^c}{A_c}, \tag{6.3}$$

where the sum is over all the vertices that form the cell c, and $\mathbf{R}_{\mathrm{i}}{}^c = \mathbf{r}_{\mathrm{i}} - \mathbf{r}_c$. With this result for a single-cell, we can calculate a mean tissue stress tensor given by

$$\sigma_T = \frac{\sum_c \sigma_c A_c}{\sum_c A_c}. \tag{6.4}$$

Using Eqs. (6.2) and (6.3), one obtains

$$\sigma_c A_c = K_A \left(A_c - A_{0c}\right) A_c \mathbb{1} + \left(K_P \left(P_c - P_{0c}\right) + \frac{J}{2}\right) \sum_{\mathrm{i}} \frac{\mathbf{r}_{\mathrm{i}+1,\mathrm{i}} \otimes \mathbf{r}_{\mathrm{i}+1,\mathrm{i}}}{r_{\mathrm{i}+1,\mathrm{i}}}, \tag{6.5}$$

Then, the mean tissue stress is given by

$$\sigma_T = \frac{1}{\sum_c A_c} \left(\sum_c -S_c A_c \mathbb{1} + \sum_{\langle \mathrm{i},j \rangle} T_{\mathrm{i}j} \frac{\mathbf{r}_{\mathrm{i},j} \otimes \mathbf{r}_{\mathrm{i},j}}{r_{\mathrm{i},j}} \right), \tag{6.6}$$

where we have defined a pressure S_c and a tension $T_{\mathrm{i}j}$ by

$$S_c = -K_A \left(A_c - A_{c0}\right), \tag{6.7}$$

$$T_{\mathrm{i}j} = K_P \left(P_{\mathrm{i}j_{c,1}} + P_{\mathrm{i}j_{c,2}} - P_{\mathrm{i}j_{0c,1}} - P_{\mathrm{i}j_{0c,2}} \right) + J. \tag{6.8}$$

$P_{\mathrm{i}j_{c,1}}$ and $P_{\mathrm{i}j_{c,2}}$ are the perimeters of the two cells that share the border formed by the vertices i and j, and $P_{\mathrm{i}j_{0c,1}}$ and $P_{\mathrm{i}j_{0c,2}}$ are the equilibrium perimeters of those two cells. From here, we can see that if we consider a tissue made of regular hexagonal cells of side a, and if $A_c = A_{c0}$ and $P_c = P_{c0}$ for every c cell, then the stress tensor of a single-cell obeys $\sigma_{c0} A_{0c} = \frac{3}{2} J a \mathbb{1}$, and then the tissue stress will be given by

$$\sigma_0 = \frac{N_c A_{c0} \frac{3}{2} J a}{N_c A_{0c}} \mathbb{1} = \frac{3}{2} J a \mathbb{1}, \tag{6.9}$$

which is exactly the zeroth order stress that we obtained in Ch. 3 for a passive tissue, and we already know it represents the stress needed to maintain that configuration. Also, if we assume a sudden change in the actomyosin activity such that $P_{0c} \to (1+\lambda_P)\, P_{0c}$ and $A_{0c} \to (1+\lambda_A)\, A_{0c}$, for every c cell, the stress tensor will look like

$$\sigma_0^{(\mathrm{act})} = \left(-\frac{27}{4} a^4 K_A \lambda_A - 18 a^2 K_P \lambda_P + \frac{3}{2} J a \right) \mathbb{1}, \tag{6.10}$$

which again, is exactly the zeroth order stress that we obtained in Ch. 3 for an active tissue.

6.2 M tensor as a field

Previously, on Ch. 3, we defined the texture matrix of a c cell (Eq. (3.12)) to represent an ellipse shape, from where we can calculate the cellular anisotropy in terms of the flattering parameter. This symmetric matrix has three degrees of freedom that allow to describe the elliptical-shape approximation: the two semi-axes, a and b (with $a > b$), and the orientational angle ϕ. In its diagonal form, its eigenvalues are a^2 and b^2. Since the determinant and the trace are invariant quantities, we have that $|M_c| = a^2 b^2$, and $\mathrm{Tr} M_c = a^2 + b^2$. In the elliptical-shape approximation the cellular area can be written as $A_c = \pi |M_c|^{1/2}$. The expression for the perimeter of an ellipse is complicated. However, a simple expression is valid in the case of $a \approx b$ (with $b/a > 0.7$), in which case the elliptical-shape approximation the cellular perimeter can be written as $P_c = \pi \sqrt{2 \mathrm{Tr} M_c}$.

Now, we can write the vertex model energy functional in terms of M_c, for the case of small anisotropy as

$$E = \sum_c \frac{K_A}{2} \left(\pi |M_c|^{1/2} - A_0 \right)^2 + \frac{K_P}{2} \sum_c \left(\pi \sqrt{2 \mathrm{Tr} M_c} - P_0 \right)^2, \tag{6.11}$$

where we assume the adhesion term to be zero, and that the target parameters are equal for all the cells, for simplicity.

We can perform a coarse-graining over the discrete perspective of the tissue to obtain a smooth symmetric tensor field $M(\mathbf{r})$, which will represent the shape at a tissue scale. We can define a energy density, per unit area, as

$$f(M) = \frac{1}{\pi |M|^{1/2}} \left[\frac{K_A}{2} \left(\pi |M|^{1/2} - A_0 \right)^2 + \frac{K_P}{2} \left(\pi \sqrt{2 \mathrm{Tr} M} - P_0 \right)^2 \right], \tag{6.12}$$

with the total elastic energy now given by $F = \int f\left(M(\mathbf{r})\right) \mathrm{d}\mathbf{r}$, exactly as in Ref. [6]. We follow the ideas from this reference to obtain an elastic stress tensor, and then we analyze the equilibrium solutions that appear when incorporating cellular activity.

In the same direction, in Ref. [58] they use a tensor called Shape Tensor, very similar to the texture matrix M_c, to develop a continuum mean-field theory for motile and non-motile tissues.

Since M is a symmetric tensor, it can be usefully factorized as $M = M_0 \mathrm{e}^{c\Theta}$, where M_0 and c are scalar fields, representing the coarse-grained cell area and anisotropy, respectively, and Θ is a trace-less tensor given by

$$\Theta = \begin{pmatrix} \cos 2\theta & \sin 2\theta \\ \sin 2\theta & -\cos 2\theta \end{pmatrix}, \tag{6.13}$$

that satisfies $\Theta^2 = \mathbb{1}$, where the angle θ represents the direction of the major semi axis of the ellipse-shape approximation. Positive values for c mean elongation along the radial direction, while negative ones mean elongation along the angular direction. Also, $|c|$ and the semi-axes a and b are related by $\cosh(c) = (a^2 + b^2)/(2ab)$, and then $c = 0$ means circular shape.

With these considerations,

$$\begin{aligned} M =& M_0 \sum_{k=0}^{\infty} \frac{c^k}{k!} \Theta^k \\ =& M_0 \sum_{k=0}^{\infty} \frac{c^{(2k)}}{(2k)!} \Theta^{(2k)} + M_0 \sum_{k=0}^{\infty} \frac{c^{(2k+1)}}{(2k+1)!} \Theta^{(2k+1)} \\ =& M_0 \sum_{k=0}^{\infty} \frac{c^{(2k)}}{(2k)!} \mathbb{1} + M_0 \sum_{k=0}^{\infty} \frac{c^{(2k+1)}}{(2k+1)!} \Theta \\ =& M_0 \left[\cosh(c)\, \mathbb{1} + \sinh(c)\, \Theta \right], \end{aligned} \tag{6.14}$$

and then $|M| = M_0^2$ and $\mathrm{Tr}M = 2M_0 \cosh(c)$.

6.3 Elastic stress tensor

We start by calculating how the tensor M changes if there is a displacement field in the system. Let's go back to the discrete perspective of the tissue, and assume a displacement field $\mathbf{u}(\mathbf{r})$, such that a vertex that used to be at $\mathbf{r}$ is now in the position $\mathbf{r}' = \mathbf{r} + \mathbf{u}(\mathbf{r})$. This means that given a displacement field, the center of the cell c changes as $\mathbf{r}_c \to \mathbf{r}'_c$ and its texture matrix M_c changes as

$$M_c \to M'_c = \frac{2}{n_c} \sum_{\mathrm{i} \in c} (\mathbf{r}'_{\mathrm{i}} - \mathbf{r}'_c) \otimes (\mathbf{r}'_{\mathrm{i}} - \mathbf{r}'_c). \tag{6.15}$$

Also, let's consider that $\mathbf{u}(\mathbf{r})$ varies little in the distance between the vertices that define a given cell and its center position. This way, the quantity $\mathbf{r}_{\mathrm{i}} - \mathbf{r}_c$, with i a vertex form the cell c, can be treated as an infinitesimal element $\mathrm{d}\mathbf{r}_{\mathrm{ic}}$, such that it transforms as $\mathrm{d}\mathbf{r}_{\mathrm{ic}} \to \mathrm{d}\mathbf{r}'_{\mathrm{ic}} = (\mathbb{1} + \nabla\mathbf{u})\, \mathrm{d}\mathbf{r}_{\mathrm{ic}}$, , where the term $\nabla\mathbf{u}$ (gradient of a vector) is a 2×2 tensor that in index notation looks like $\partial_j u_{\mathrm{i}} \mathbf{e}_{\mathrm{i}} \otimes \mathbf{e}_j$. With all these considerations, the texture matrix changes as

$$
\begin{aligned}
M_c \to M_c' &= \frac{2}{n_c} \sum_{\mathrm{i}\in c} \mathrm{d}\mathbf{r}'_{\mathrm{i}c} \otimes \mathrm{d}\mathbf{r}'_{\mathrm{i}c} \\
&= \frac{2}{n_c} \sum_{\mathrm{i}\in c} \left[(\mathbb{1} + \nabla\mathbf{u})\, \mathrm{d}\mathbf{r}_{\mathrm{i}c}\right] \otimes \left[(\mathbb{1} + \nabla\mathbf{u})\, \mathrm{d}\mathbf{r}_{\mathrm{i}c}\right] \\
&= M_c + \frac{2}{n_c} \sum_{\mathrm{i}\in c} \left[(\nabla\mathbf{u})\, \mathrm{d}\mathbf{r}_{\mathrm{i}c}\right] \otimes \mathrm{d}\mathbf{r}_{\mathrm{i}c} + \frac{1}{n_c} \sum_{\mathrm{i}\in c} \mathrm{d}\mathbf{r}_{\mathrm{i}c} \otimes \left[(\nabla\mathbf{u})\, \mathrm{d}\mathbf{r}_{\mathrm{i}c}\right] \\
&= M_c + \frac{2}{n_c} \sum_{\mathrm{i}\in c} \left[(\nabla\mathbf{u})\, \mathrm{d}\mathbf{r}_{\mathrm{i}c}\right] \otimes \mathrm{d}\mathbf{r}_{\mathrm{i}c} + \left(\frac{1}{n_c} \sum_{\mathrm{i}\in c} \left[(\nabla\mathbf{u})\, \mathrm{d}\mathbf{r}_{\mathrm{i}c}\right] \otimes \mathrm{d}\mathbf{r}_{\mathrm{i}c}\right)^{\mathrm{T}}, \qquad (6.16)
\end{aligned}
$$

where the term $\left[(\nabla\mathbf{u})\, \mathrm{d}\mathbf{r}_{\mathrm{i}c}\right] \otimes \mathrm{d}\mathbf{r}_{\mathrm{i}c}$ has the shape $(A\mathbf{b}) \otimes \mathbf{b}$, and in index notation

$$
\begin{aligned}
\left[(A\mathbf{b}) \otimes \mathbf{b}\right]_{\mathrm{i}j} &= (A\mathbf{b})_{\mathrm{i}}\, b_j = A_{\mathrm{i}l} b_l b_j, \qquad (6.17) \\
\left[A\,(\mathbf{b} \otimes \mathbf{b})\right]_{\mathrm{i}j} &= A_{\mathrm{i}l}\,(\mathbf{b} \otimes \mathbf{b})_{lj} = A_{\mathrm{i}l} b_l b_j, \qquad (6.18)
\end{aligned}
$$

and hence $\left[(\nabla\mathbf{u})\, \mathrm{d}\mathbf{r}_{\mathrm{i}c}\right] \otimes \mathrm{d}\mathbf{r}_{\mathrm{i}c} = (\nabla\mathbf{u})\left[\mathrm{d}\mathbf{r}_{\mathrm{i}c} \otimes \mathrm{d}\mathbf{r}_{\mathrm{i}c}\right]$, and since M_c is symmetric we obtain

$$
M_c \to M_c' = M_c + (\nabla\mathbf{u})\, M_c + M_c\, (\nabla\mathbf{u})^{\mathrm{T}}. \qquad (6.19)
$$

Is important to remember that this new M_c' is defined with a new cellular center $\mathbf{r}'_c = \mathbf{r}_c + \mathbf{u}(\mathbf{r}_c)$, which means that when performing the coarse-graining, we obtain

$$
M'(\mathbf{r} + \mathbf{u}) = M(\mathbf{r}) + (\nabla\mathbf{u})\, M(\mathbf{r}) + M(\mathbf{r})\, (\nabla\mathbf{u})^{\mathrm{T}}. \qquad (6.20)
$$

By changing $\mathbf{r} + \mathbf{u} \to \mathbf{r}$, and performing a Taylor expansion on the right hand side up to $O(|\nabla\mathbf{u}|)$, we finally obtain

$$
M'(\mathbf{r}) = M(\mathbf{r}) - \mathbf{u} \cdot \nabla M(\mathbf{r}) + (\nabla\mathbf{u})\, M(\mathbf{r}) + M(\mathbf{r})\, (\nabla\mathbf{u})^{\mathrm{T}}. \qquad (6.21)
$$

If there is a displacement field $\mathbf{u}$, then the field M changes ($\delta M = M' - M$), and hence F changes as $\delta F = F(M') - F(M)$. Then, considering the following notation of the scalar inner product of two second order tensors A and B

$$
A : B = (A_{\mathrm{i}j}\mathbf{e}_{\mathrm{i}} \otimes \mathbf{e}_j) : (B_{kl}\mathbf{e}_k \otimes \mathbf{e}_l) = A_{\mathrm{i}j} B_{kl} \delta_{\mathrm{i}k} \delta_{jl} = A_{\mathrm{i}j} B_{\mathrm{i}j}, \qquad (6.22)
$$

we get

$$\begin{aligned}\delta F =& \int \frac{\partial f}{\partial M} : \delta M \mathrm{d}\mathbf{r}, \\ =& \int \frac{\partial f}{\partial M} : \left[-\mathbf{u} \cdot \nabla M(\mathbf{r}) + (\nabla \mathbf{u}) M(\mathbf{r}) + M(\mathbf{r}) (\nabla \mathbf{u})^{\mathrm{T}} \right] \mathrm{d}\mathbf{r}. \end{aligned} \tag{6.23}$$

Now the idea is to write the argument of the integral as $(...) : \nabla \mathbf{u}$, where the left term is going to represent the elastic stress tensor.

We re-write term by term, using index notation, as

$$\begin{aligned}\frac{\partial f}{\partial M} : [-\mathbf{u} \cdot \nabla M] =& - \frac{\partial f}{\partial M_{\mathrm{i}j}} u_k \frac{\partial M_{\mathrm{i}j}}{\partial x_k} = -\frac{\partial f}{\partial x_k} u_k = -\frac{\partial f u_k}{\partial x_k} + f \frac{\partial u_k}{\partial x_k} \\ =& - \nabla \cdot (f\mathbf{u}) + f \delta_{\mathrm{i}j} \frac{\partial u_j}{\partial x_{\mathrm{i}}} = -\nabla \cdot (f\mathbf{u}) + f \mathbb{1} : \nabla \mathbf{u}, \end{aligned} \tag{6.24}$$

$$\frac{\partial f}{\partial M} : [(\nabla \mathbf{u}) M] = \frac{\partial f}{\partial M_{\mathrm{i}j}} \frac{\partial u_{\mathrm{i}}}{\partial x_l} M_{lj} = \frac{\partial f}{\partial M_{\mathrm{i}j}} M^{\mathrm{T}}_{jl} \frac{\partial u_{\mathrm{i}}}{\partial x_l} = \frac{\partial f}{\partial M} M^{\mathrm{T}} : \nabla \mathbf{u}, \tag{6.25}$$

$$\frac{\partial f}{\partial M} : \left[M (\nabla \mathbf{u})^{\mathrm{T}} \right] = \frac{\partial f}{\partial M_{\mathrm{i}j}} M_{\mathrm{i}l} \frac{\partial u_l}{\partial x_j}^{\mathrm{T}} = \frac{\partial f}{\partial M_{j\mathrm{i}}}^{\mathrm{T}} M_{\mathrm{i}l} \frac{\partial u_j}{\partial x_l} = \left(\frac{\partial f}{\partial M} \right)^{\mathrm{T}} M : \nabla \mathbf{u}. \tag{6.26}$$

One can finally write

$$\begin{aligned}\delta F =& \int \frac{\partial f}{\partial M} : \delta M \mathrm{d}\mathbf{r}, \\ =& \int \left[-\nabla \cdot (f\mathbf{u}) + \left(f\mathbb{1} + \frac{\partial f}{\partial M} M^{\mathrm{T}} + \left(\frac{\partial f}{\partial M} \right)^{\mathrm{T}} M \right) : \nabla \mathbf{u} \right] \mathrm{d}\mathbf{r}. \end{aligned} \tag{6.27}$$

The first term vanishes at the boundary of the system, and using the fact that M is symmetric, the elastic stress tensor σ_{e} is given by

$$\sigma_{\mathrm{e}} = f\mathbb{1} + 2 \frac{\partial f}{\partial M} M \tag{6.28}$$

To calculate σ_{e}, we need to previously calculate the following relations

$$\frac{\partial \mathrm{Tr} M}{\partial M} = \frac{\partial \left(M_{11} + M_{22} \right)}{\partial M} = \frac{\partial \left(M_{11} + M_{22} \right)}{\partial M_{\mathrm{i}j}} \mathbf{e}_{\mathrm{i}} \otimes \mathbf{e}_j = \mathbb{1}, \tag{6.29}$$

$$\frac{\partial |M|}{\partial M} = \frac{\partial \left(M_{11} M_{22} - M_{12} M_{21} \right)}{\partial M} = \begin{pmatrix} M_{22} & -M_{21} \\ -M_{12} & M_{11} \end{pmatrix} = \begin{pmatrix} M_{22} & -M_{12} \\ -M_{21} & M_{11} \end{pmatrix} = |M| M^{-1}, \tag{6.30}$$

and then

$$\frac{\partial f}{\partial M} = -\frac{1}{2}\frac{1}{\pi|M|^{1/2}}\left[\frac{K_A}{2}\left(\pi|M|^{1/2}-A_{0c}\right)^2+\frac{K_P}{2}\sum_c\left(\pi\sqrt{2\mathrm{Tr}M}-P_{0c}\right)^2\right]M^{-1} + \frac{K_A}{2}\left(\pi|M|^{1/2}-A_{0c}\right)M^{-1}+\frac{1}{|M|^{1/2}}K_P\left(\pi-\frac{P_{0c}}{\sqrt{2\mathrm{Tr}M}}\right)\mathbb{1} \tag{6.31}$$

$$2\frac{\partial f}{\partial M}M = -\frac{1}{\pi|M|^{1/2}}\left[\frac{K_A}{2}\left(\pi|M|^{1/2}-A_0\right)^2+\frac{K_P}{2}\sum_c\left(\pi\sqrt{2\mathrm{Tr}M}-P_0\right)^2\right]\mathbb{1} + K_A\left(\pi|M|^{1/2}-A_0\right)\mathbb{1}+\frac{2}{|M|^{1/2}}K_P\left(\pi-\frac{P_0}{\sqrt{2\mathrm{Tr}M}}\right)M \tag{6.32}$$

$$\sigma_{\mathrm{e}} = K_A\left(\pi|M|^{1/2}-A_0\right)\mathbb{1}+\frac{2}{|M|^{1/2}}K_P\left(\pi-\frac{P_0}{\sqrt{2\mathrm{Tr}M}}\right)M \tag{6.33}$$

In the Ref. [6] they use a similar form of the previous stress tensor into an hydrodynamic system of equations (force balance, kinematic and cell number balance) of epithelial tissues in which the cells can rearrange. They also include activity phenomenologically using a thermodynamic formalism. They apply the model to study analytically the passive relaxation following an axial stretching with constant rate over an initially homogenous tissue, the deformation of a tissue due to the active internal forces, and the generation of shear flow. In all the applications they assume for simplicity that the two-dimensional tissue is incompressible (M_0 is constant) and spatial homogeneity of all relevant fields. They also compare the steady state found by using their continuum description and simulations using the vertex model, in the case of passive tissues under uniaxial elongations.

In the next sections we consider tissues where the activity is considered as changes in the target parameters, exactly as in the previous sections. We study active epithelial tissues using a continuum description where the activity is related to biological processes at the cellular level. We consider inhomogeneous cellular activity distributions and analyze their steady state and also their temporal evolution, and compare the results with the ones obtained with simulations of the vertex model.

6.4 Centered active force: steady state

We consider a tissue initially at equilibrium characterized by an homogenous M field, with $M_0(\mathbf{r}) = m_0 = A_0/\pi, c(\mathbf{r}) = 0$ and $\Theta = \Theta(\theta = 0)$, which is subject to an active process that changes the target parameters as $A_0 \to A_0\left[1+\alpha_A\kappa(r)\right]$ and $P_0 \to P_0\left[1+\alpha_P\kappa(r)\right]$, where $\kappa(r)$ is a function that describes the inhomogeneity of the cellular activity in the tissue. We will study the new equilibrium state, characterized by new expressions of M_0, c and Θ. We propose the Gaussian function $\kappa(r) = \mathrm{e}^{\frac{-r^2}{2R^2}}$, where R is the standard deviation that represent

the range of the active function. The maximum changes occur at $r = 0$, where $\kappa(r = 0) = 1$, and then the target values are given by $A_0 \to A_0\,(1 + \alpha_A)$ and $P_0 \to P_0\,(1 + \alpha_P)$. Then, α_A and α_P have the interpretation of contractility, and we allow them to take values from -1 to ∞: negative values represent the reduction of the target parameters (contractions), while positive ones represent the increase of them (expansions).

We begin by analyzing the case of medial activity. The total stress tensor σ is given by $\sigma = \sigma_{\rm e} - K_A A_0 \alpha_A \kappa(r) \mathbb{1}$, where the last term corresponds to an isotropic active stress tensor. The mechanical equilibrium will be reached when $\nabla \cdot \sigma = 0$, i.e., when

$$\nabla \cdot \sigma_{\rm e} = K_A A_0 \alpha_A \frac{\partial \kappa(r)}{\partial r} \hat{\mathbf{r}}. \tag{6.34}$$

Given the symmetries of our initial system and the radial force, we expect the displacement field to has the form $\mathbf{u} = u(r)\hat{\mathbf{r}}$, with the coarse-grained orientations, in good approximation, given by the θ-polar angle, and $M_0 = M_0(r)$ and $c = c(r)$. Then, we decide to work in polar coordinates, such that the new representation of M is

$$M = \begin{pmatrix} M_0 {\rm e}^{c} & 0 \\ 0 & M_0 {\rm e}^{-c} \end{pmatrix}, \tag{6.35}$$

and the divergence of the elastic stress tensor $\sigma_{\rm e}$ is given by

$$\nabla \cdot \sigma_{\rm e} = \left(\frac{\partial {\sigma_{\rm e}}^{rr}}{\partial r} + \frac{1}{r} \left[{\sigma_{\rm e}}^{rr} - {\sigma_{\rm e}}^{\theta\theta} \right] \right) \hat{r}. \tag{6.36}$$

Then from Eq. (6.34) we obtain

$$\frac{\partial {\sigma_{\rm e}}^{rr}}{\partial r} + \frac{1}{r} \left({\sigma_{\rm e}}^{rr} - {\sigma_{\rm e}}^{\theta\theta} \right) = - K_A A_0 \alpha {\rm e}^{\frac{-r^2}{2R^2}} r. \tag{6.37}$$

Using in Eq. (6.21) that the initial value of the texture matrix is $M(\mathbf{r}) = m_0 \mathbb{1}$ and that the final value ($M'(\mathbf{r})$) due to the displacement field is given by right hand side of Eq. (6.35), we obtain

$$M_0 \begin{pmatrix} {\rm e}^{c} & 0 \\ 0 & {\rm e}^{-c} \end{pmatrix} = \begin{pmatrix} 1 + 2\frac{{\rm d}u}{{\rm d}r} & 0 \\ 0 & 1 + 2\frac{u}{r} \end{pmatrix}, \tag{6.38}$$

from where we get useful expressions of the scalar fields M_0 and c in terms of the displacement field, given by

$$M_0(r) = m_0 \sqrt{\left(1+\frac{2u}{r}\right)\left(1+2\frac{\mathrm{d}u}{\mathrm{d}r}\right)}, \tag{6.39}$$

$$\cosh\left[c\left(r\right)\right] = \frac{m_0}{M_0(r)}\left(\frac{\mathrm{d}u}{\mathrm{d}r}+\frac{u}{r}+1\right), \tag{6.40}$$

$$\sinh\left[c\left(r\right)\right] = \frac{m_0}{M_0(r)}\left(\frac{\mathrm{d}u}{\mathrm{d}r}-\frac{u}{r}\right). \tag{6.41}$$

We replace the expressions (6.39), (6.40) and (6.41) in Eq. (6.33), and then use it to solve Eq. (6.37) numerically, by imposing that the displacement field is zero at the origin and also at infinity. More specifically, Fig. 6.1 shows the results for the case of $K_A = K_P = 1, R = 1$ and $\alpha_A = \pm 1$, when imposing that $u(r)$ vanishes at $r = 30$.

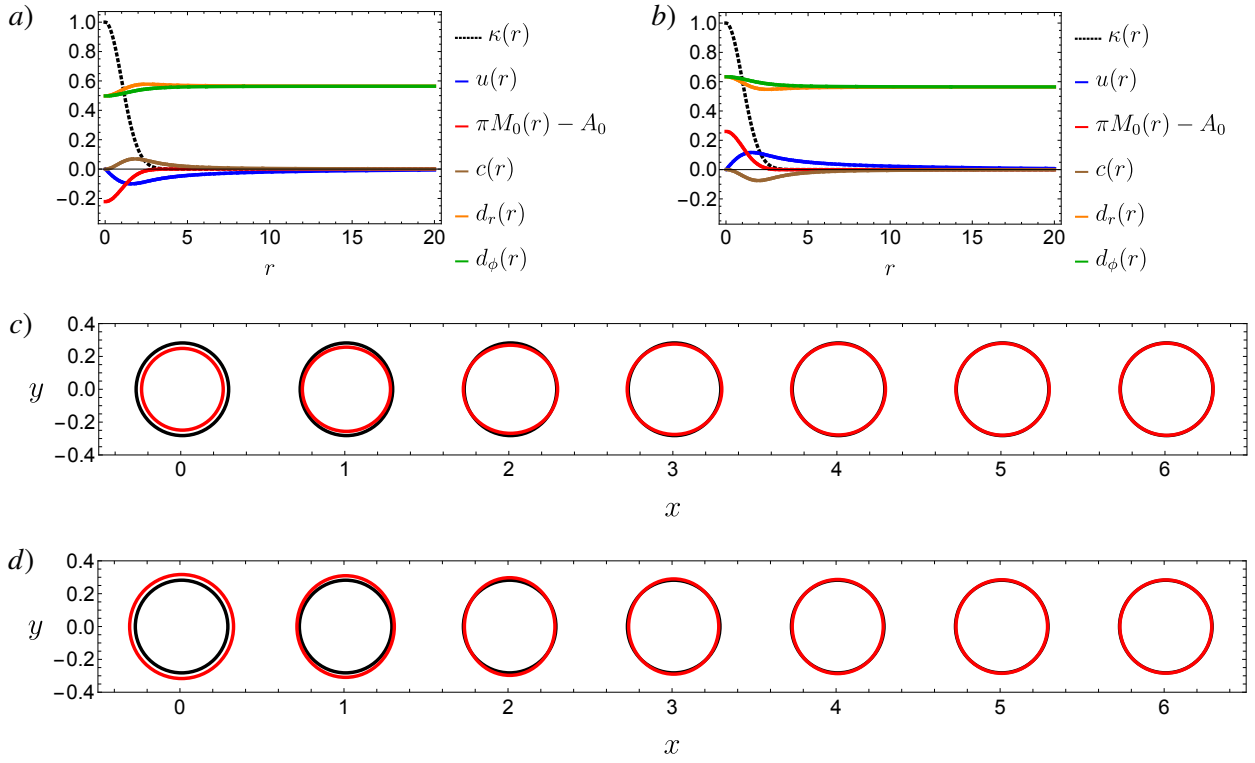

Figure 6.1: Spatial dependence of the active function (κ), displacement field (u), contraction ($\pi M_0 - A_0$), anisotropy (c) and radial and angular semi-axes of M (d_d and d_r, respectively), considering the initially homogeneous system defined by $K_A = K_P = 1, A_0 = 1$, under centered medial activity characterized by $R = 1$, and $\alpha_A = -1$ in a), and $\alpha_A = 1$ in b). In c) and d) are the geometrical representation of the cellular shape for different distances x, derived from the M field, in black (homogeneous initial configuration) and in red (final solution due to activity), for the cases of $\alpha_A = -1$ and $\alpha_A = 1$, respectively. The cells have been shown at half their size to avoid overlapping.

Figure 6.1 shows the expected behavior for the anisotropy: when the active region gets contracted c takes positive values, i.e., cells get elongated in the radial direction; when the

active region gets expanded c takes negative values, i.e., cells get elongated in the angular direction. The contractile response $(\pi M_0 - A_0)$ remains localized in the active region, while the cellular anisotropy c changes in both the active and a small part of the non-active region.

When, instead, we consider perimeter activity, the stress tensor is given by $\sigma = \sigma_{\rm e} - K_P P_0 \alpha_P \left[\kappa(r)/\sqrt{\cosh(c)\, M_0^3}\right] M$, and the equilibrium condition gives

$$\nabla \cdot \sigma_{\rm e} = K_P P_0 \alpha_P \left[\frac{\partial}{\partial r}\left(\frac{\kappa(r)}{\sqrt{\cosh(c)\, M_0}} {\rm e}^c\right) + \frac{2}{r}\frac{\sinh(c)\,\kappa(r)}{\sqrt{\cosh(c)\, M_0}}\right] \hat{\mathbf{r}}, \tag{6.42}$$

and then using the same Gaussian function for $\kappa(r)$ as before, we obtain

$$\frac{\partial {\sigma_{\rm e}}^{rr}}{\partial r} + \frac{1}{r}\left({\sigma_{\rm e}}^{rr} - {\sigma_{\rm e}}^{\theta\theta}\right) = K_P P_0 \alpha_P \left[\frac{\partial}{\partial r}\left(\frac{{\rm e}^{\frac{-r^2}{2R^2}}\left[\cosh(c) + \sinh(c)\right]}{\sqrt{\cosh(c)\, M_0}}\right) + \frac{2}{r}\frac{\sinh(c)\,{\rm e}^{\frac{-r^2}{2R^2}}}{\sqrt{\cosh(c)\, M_0}}\right]. \tag{6.43}$$

We solve Eq. (6.43) numerically, imposing again that $u(r)$ vanishes at zero and at infinity. Fig. 6.2 shows the results for the case of $K_A = K_P = 1, R = 1$ and $\alpha_P = \pm 0.3$, when imposing that $u(r)$ vanishes at $r = 30$.

Figure 6.2 shows the same qualitative behavior of the contraction and anisotropy than the Fig. 6.1 (medial activity). From Figs. 6.1 and 6.2 we obtain that perimeter activity achieves bigger levels of contraction with smaller values of contractility, which is an observation we also reported in Ch. 4, when modeling active contraction pulses in localized epithelial cells using the vertex model.

6.4.1 Comparison with simulations

We compare the solutions of this continuum description with numerical simulations performed using ordered and low-disordered tissues. These systems use a box of size $L_x = 50\sqrt{3}a$ and $L_y = 90a$, and contain 3000 cells. In particular, ordered tissues are made of perfect hexagonal cells of side $a = \sqrt{2/\sqrt{3}}$, such that they have unitary area. That regular lattice defines the equilibrium parameters. Low-disordered tissues are created by adding a 10% of Gaussian noise over the regular shape (Fig. 6.7-A)-up). That configuration defines the equilibrium parameters in this case. However, this is not the state over which we apply the active Gaussian function. First, we perform a relaxation phase, for $t_{\rm relax} = 5$, to obtain the stationary configuration of the tissue (Fig. 6.7-A)-bottom). This relaxed state is the initial condition for the low-ordered tissues simulations.

To consider the same boundary conditions in both descriptions (discrete and continuum), we decide to establish a rigid boundary at $R_{box} = 12\sqrt{2\sqrt{3}}a = 24$, measured from the center of the active region (maximum of the κ-function). In the numerical solution of the ODE this

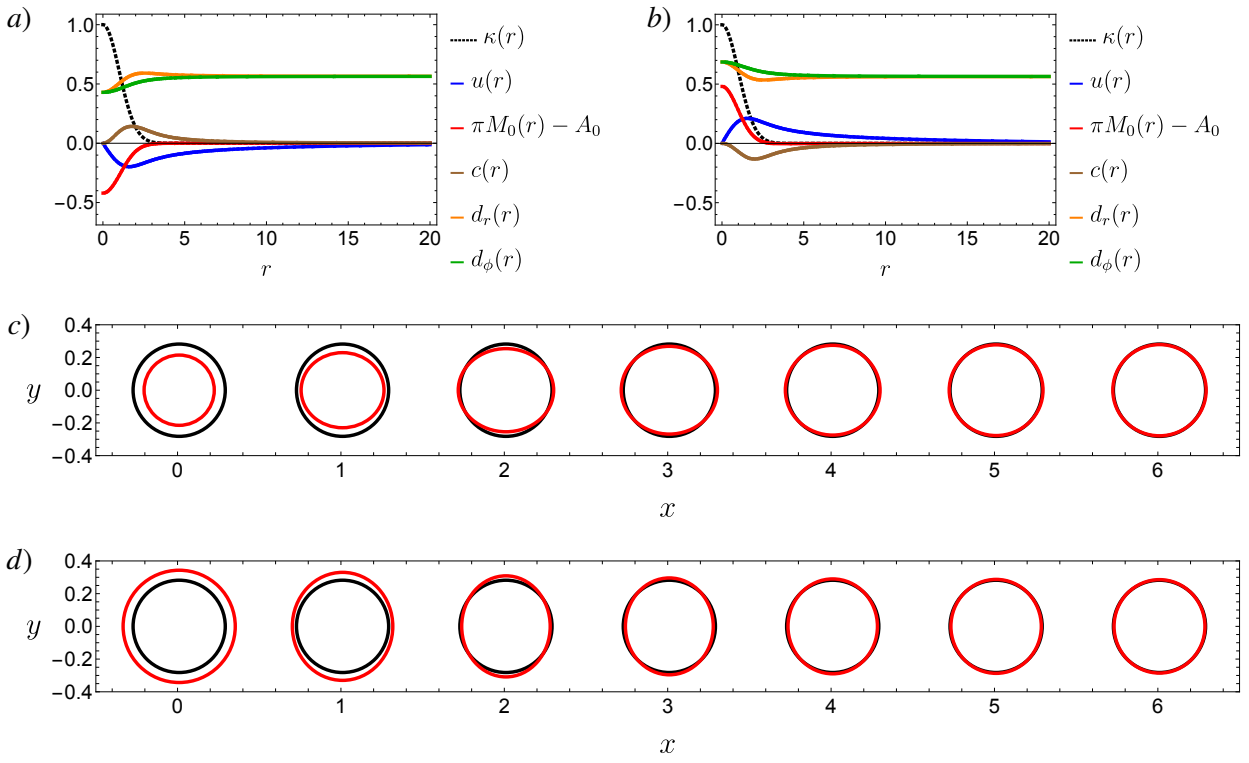

Figure 6.2: Same representation as in Fig. 6.1, with perimeter activity characterized by $\alpha_P = -0.3$ and $\alpha_P = 0.3$.

means we will impose that the displacement $u(r)$ vanishes at $r = R_{box}$. In the simulations using the vertex model, this means we will fix the motion of vertices whose distance from the active center is greater than R_{box}.

In the simulations, the differential equations are integrated using the Euler integration method, fixing units such that $K_A = K_P = J = 1$ and $a = \sqrt{2/\sqrt{3}}$. We include the adhesion term J to avoid instabilities that may arise when considering $J = 0$. To include this term in the ODE solutions, we redefine the equilibrium perimeter as $P_{0c} - J/(2K_P)$, which is a correct decision since there is no plasticity considered in our simulations (as discussed in Ch. 4). The time step was fixed to $dt = 0.01$, and we study the system up to $t = 200$ to ensure that it reaches a steady state. We use values of $\alpha_A = -0.5$ and $\alpha_P = -0.1$, mimicking a contraction in an active region, as in the simulations of Ch. 4. The used values of A_0 and P_0 in the ODE are the ones of the ordered tissue in the vertex model simulations.

Figures 6.3 and 6.4 show the results for the spatial distribution of the displacement u given by the continuum description, the radial and tangential displacements, u_r and u_ϕ, given by the simulations with an ordered tissue, and the change of area ΔA and anisotropy c, for both models, for the cases of medial activity with $\alpha_A = -0.5$ and $\alpha_P = 0$, and perimeter activity with $\alpha_A = 0$ and $\alpha_P = -0.1$, respectively, with $R = 0.4$ and $R = 4$. The areas are calculated directly from M in the continuum framework. In the simulations, we calculate them by using the triangularization method. In the case of anisotropies, in both descriptions, they are calculated from M. We assignee the sign of c in the simulations by considering positive when the orientational angle of a cell is closer to the radial direction than to the angular

one, and negative sign in the other case. We show that the qualitative agreement between both descriptions is excellent, being slightly better for larger values of R. We observe that i) the maximum area change (ΔA_{max}) is reached at $r = 0$, in both descriptions; ii) the change of area changes of sign, meaning that if one region gets contracted, then another one has to get expanded, due to the conservation of the total area of the box, in both descriptions; iii) the anisotropy has a well-defined maximum value in the continuum description, but in the simulations with the ordered tissue it presents noise due to the hexagonal lattice and to the way we decide to calculate c; iv) the averaged tangential displacement in the simulations is null; v) the displacement obtained by solving the ODE has a well-defined minimum. The radial displacement of the simulations has noise due to the hexagonal lattice.

To get a quantitative comparison between the models for different sizes of the active region (different values of R in the κ-function), we calculate three observables: i) the maximum area change (ΔA_{max}), ii) the minimum (radial) displacement (ur_{min}), and iii) the distance at which the (radial) displacement is minimum ($r.ur_{min}$).

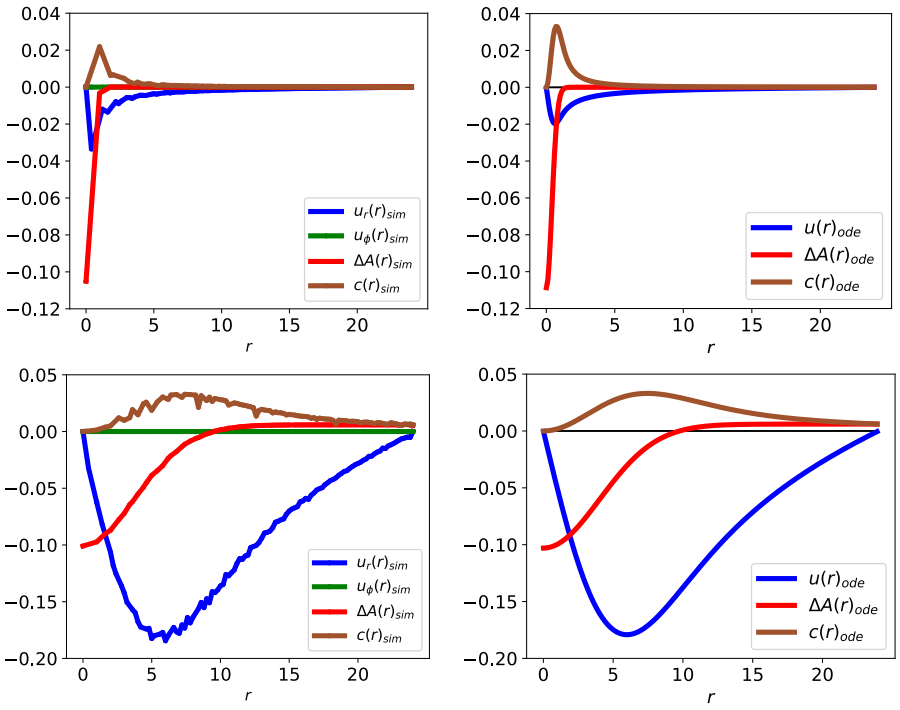

Figure 6.3: Left: Spatial distribution of the radial and tangential displacements, u_r and u_ϕ, the change of area ΔA and anisotropy c obtained with the numerical simulations using the ordered tissue for the case of medial activity with $\alpha_A = -0.5$ and $\alpha_P = 0$, for $R = 0.4$ (up) and $R = 4$ (bottom). Right: Spatial distribution of the displacement u, the change of area ΔA and anisotropy c, obtained by solving the ODE from the continuum description for the same activity cases.

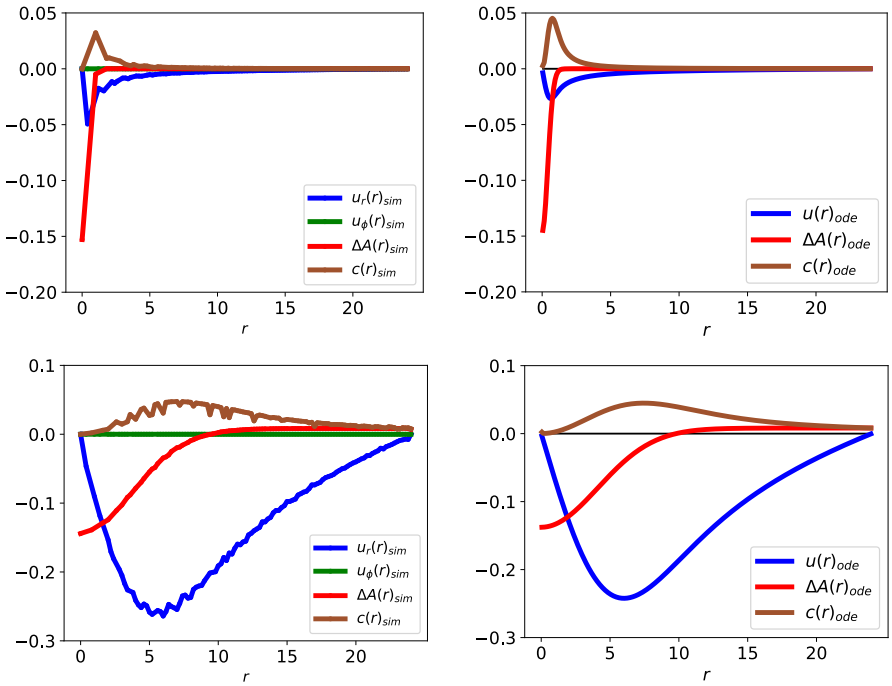

Figure 6.4: Same representation as in Fig. 6.3, when considering perimeter activity with $\alpha_A = 0$ and $\alpha_P = -0.1$.

Figures 6.5 and 6.6-A show the comparison of the three previously mentioned observables, using the numerical simulations results of the ordered tissue, for both medial ($\alpha_A = -0.5$ and $\alpha_P = 0$) and perimeter ($\alpha_A = 0$ and $\alpha_P = -0.1$) activity, respectively.

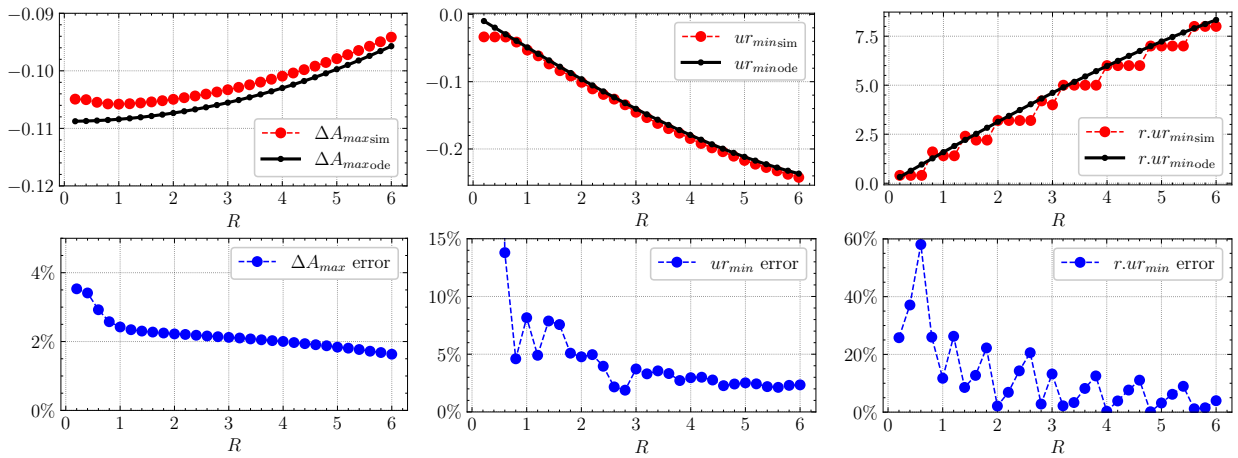

Figure 6.5: Up: Comparison of the maximum area change (ΔA_{max}) (left), the minimum (radial) displacement (ur_{min}) (middle), and the distance at which the (radial) displacement is minimum ($r.ur_{min}$) (right), between the ODE solution (in black) and the numerical simulations using vertex model with the ordered tissue (in red), for the case of medial activity with $\alpha_A = -0.5$ and $\alpha_P = 0$. Bottom: Error for each observable $O = \{\Delta A_{max}, ur_{min}, r.ur_{min}\}$, defined $100|(O_{\mathrm{ode}} - O_{sim})/O_{\mathrm{ode}}|$. The error points of ur_{min} at $R = \{0.2, 0.4\}$ (not shown in the figure) are around 240 and 70%, respectively.

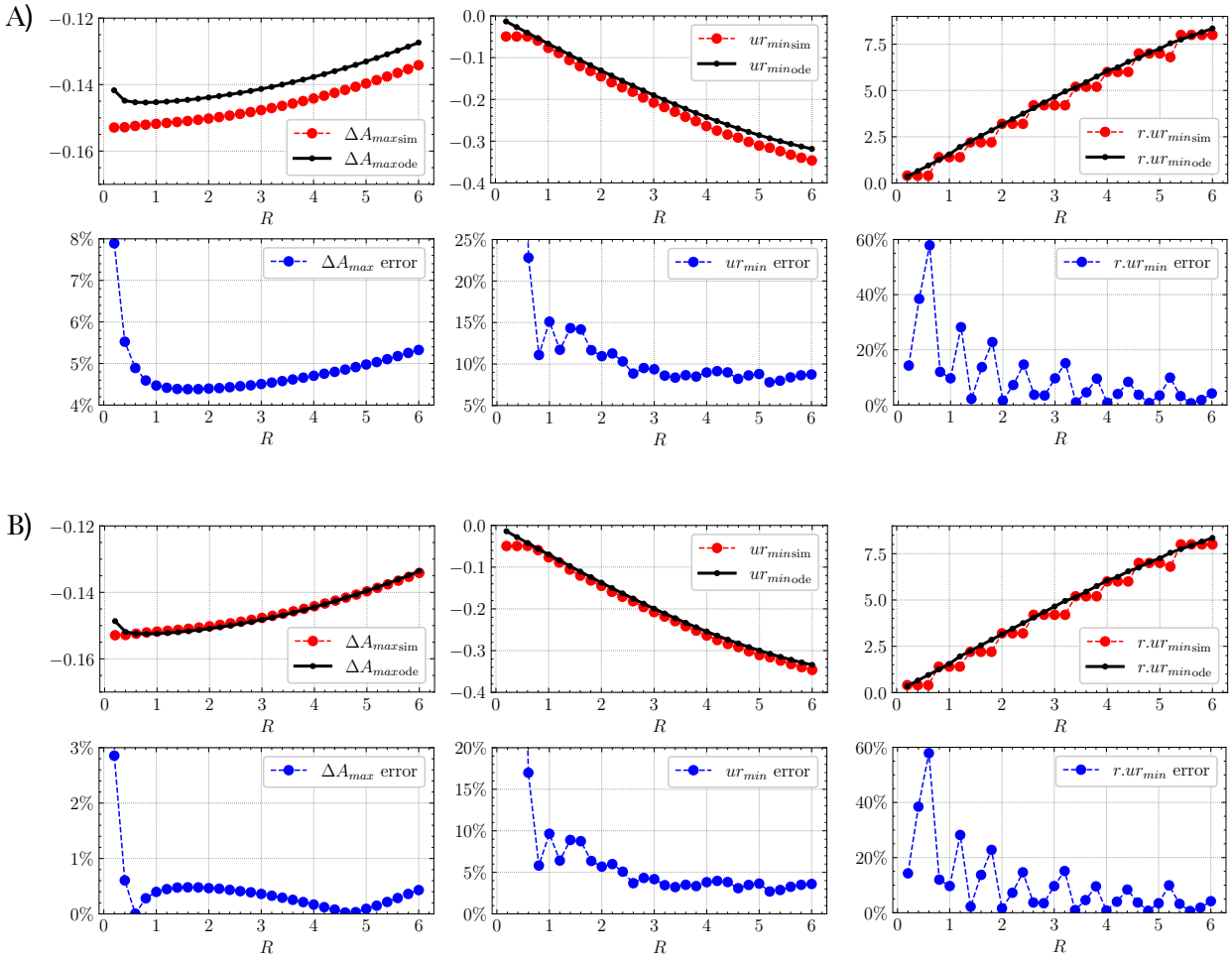

Figure 6.6: Same representation as in Fig. 6.5, for the case of perimeter activity with $\alpha_A = 0$ and $\alpha_P = -0.1$, for both descriptions (A)), and $\alpha_A = 0$ and $\alpha_P = -0.1$ in the simulations and $\alpha_A = 0$ and $\alpha_P = -0.105$ in the ODE (B)). In A), the error points of ur_{min} at $R = \{0.2, 0.4\}$ (not shown in the figure) are around 280 and 80%, respectively. In B), the error points of ur_{min} at $R = \{0.2, 0.4\}$ (not shown in the figure) are around 260 and 80%, respectively.

When the medial region is the active one, the maximum area change (ΔA_{max}) is underestimated by the continuum description by less than 3.6%, for values of $R \in (0.2, 6)$. The error of the distance at which the (radial) displacement is minimum ($r.ur_{min}$), and the error for its value (ur_{min}), decrease in average for larger values of R. For $R > 2$, the error of ur_{min} take values smaller than 5%. For $R > 3$, the error of $r.ur_{min}$ take values smaller than 10%. Then, the continuum description is quantitatively accurate for reproducing the numerical results using the vertex model when studying the steady-state reached by an ordered tissue composed of cells with unitary area, with medial activity in a Gaussian region of size (standard deviation) $R > 3$.

When the cellular perimeter is active, the maximum area change (ΔA_{max}) is overestimated by the continuum description by errors between 4% and 8%, for values of $R \in (0.2, 6)$. As in the case of medial activity, the errors of ur_{min} and $r.ur_{min}$ decrease in average for larger values of R. For $R > 2.5$, the error of ur_{min} take values smaller than 10%. For $R > 3.5$, the error of $r.ur_{min}$ take values smaller than 10%. By inspection, we obtain a better fit between

the two descriptions when we use different parameters of perimeter activity. Fig. 6.6-B shows the comparison of the three observables, obtained from the numerical simulations of an ordered tissue using $\alpha_A = 0$ and $\alpha_{Psim} = -0.1$, and by solving the ODE using $\alpha_A = 0$ and $\alpha_{P\text{ode}} = -0.105$. With this consideration, $r.ur_{min}$ maintain the same values as before, but ΔA_{max} and ur_{min} decrease their errors considerably. For $R > 0.2$, the errors of ΔA_{max} take values smaller than 1%. For $R > 2.5$, the errors of ur_{min} take values smaller than 5%. We conclude that the continuum description is highly accurate, in quantitative terms, in the case of perimeter activity in a Gaussian region of size (standard deviation) $R > 2.5$, when considering different parameters of contractility between both descriptions, with the continuum-contractility being 5% stronger than de discrete one.

We find that the distance at which the (radial) displacement is minimum ($r.ur_{min}$) when using an ordered tissue is independent of the kind of activity and the value of the contractility. In both cases (Figs. 6.5 and 6.6) we obtain the same results. The steps seen in the quantification of this observable are due to the discretization of the space in the numerical calculations.

Figure 6.7-B) shows the results for the spatial distribution of the displacement u, the change of area ΔA and the anisotropy c given by the continuum description, plus the radial and tangential displacements, u_r and u_ϕ, the change of area ΔA and the change of anisotropy Δc, given by the averaged response of 30 different simulations. In each simulation we choose a different origin of the Gaussian function, using the low-disordered tissue, for the cases of medial activity with $\alpha_A = -0.5$ and $\alpha_P = 0$ and perimeter activity with $\alpha_A = 0$, $\alpha_{Psim} = -0.1$ and $\alpha_{P\text{ode}} = \{-0.1, -0.105\}$, with $R = 4$. In the simulations, we define the variations ΔA and Δc with respect to the relaxed state. We obtain a great agreement between both descriptions for medial and perimeter activity as in the ordered tissue. Also, the fit is better when we consider different contractilities for the continuum and the discrete frameworks: 5% bigger the continuum than the discrete one. We show that the change of anisotropy has many deviations from the mean response, as expected for the way we calculate it (just as in the ordered tissue). The change of area and the radial displacement have low variations from the mean responses, and hence the three observables quantified in the ordered tissue are equally interesting here.

Figure 6.8 shows the comparison of the i) the maximum area change (ΔA_{max}), ii) the minimum (radial) displacement (ur_{min}), and iii) the distance at which the (radial) displacement is minimum ($r.ur_{min}$), using the numerical simulations results of the low-disordered tissue, for both medial activity with $\alpha_A = -0.5$ and $\alpha_P = 0$ and perimeter activity with $\alpha_A = 0$, $\alpha_{Psim} = -0.1$ and $\alpha_{P\text{ode}} = \{-0.1, -0.105\}$. The averaged response from the simulations fits the ODE solution excellently when using the change of 5% in the perimeter contractility for the continuum description. We find that the distance at which the (radial) displacement is minimum ($r.ur_{min}$) is independent of the kind of activity, and the value of the contractility, just as for the ordered tissue. Also, the error of the maximum area change (ΔA_{max}) for small R is less than in the ordered tissue.

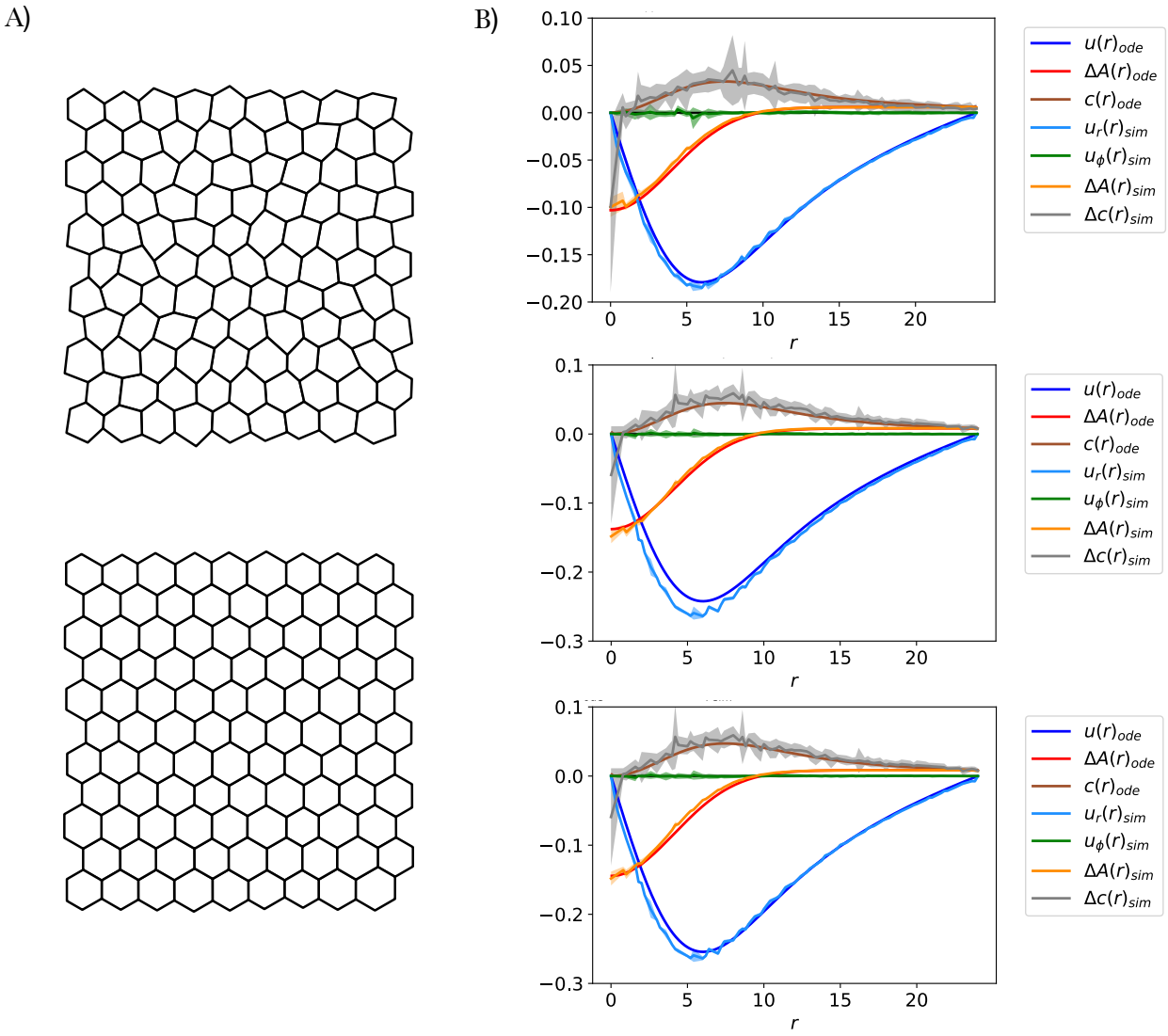

Figure 6.7: A) Section of the low-disordered tissue. Up: the initially disordered state from which we define the values of the equilibrium areas and perimeters. Bottom: relaxed disordered state over which we apply the Gaussian activity, obtained after $t_{\text{relax}} = 5$. B) Spatial distribution of the displacement u, the change of area ΔA and the anisotropy c given by the continuum description, and also the radial and tangential displacements, u_r and u_ϕ, the change of area ΔA and the change of anisotropy Δc, given by the simulations using the averaged response of 30 different simulations changing the origin of the Gaussian function in the low-disordered tissue, for the cases of medial activity with $\alpha_A = -0.5$ and $\alpha_P = 0$ (up), perimeter activity with $\alpha_A = 0$ and $\alpha_P = -0.1$ (middle), and perimeter activity with $\alpha_A = 0$, $\alpha_{P_{sim}} = -0.1$, and $\alpha_{P_{ode}} = -0.105$ (bottom), with $R = 4$.

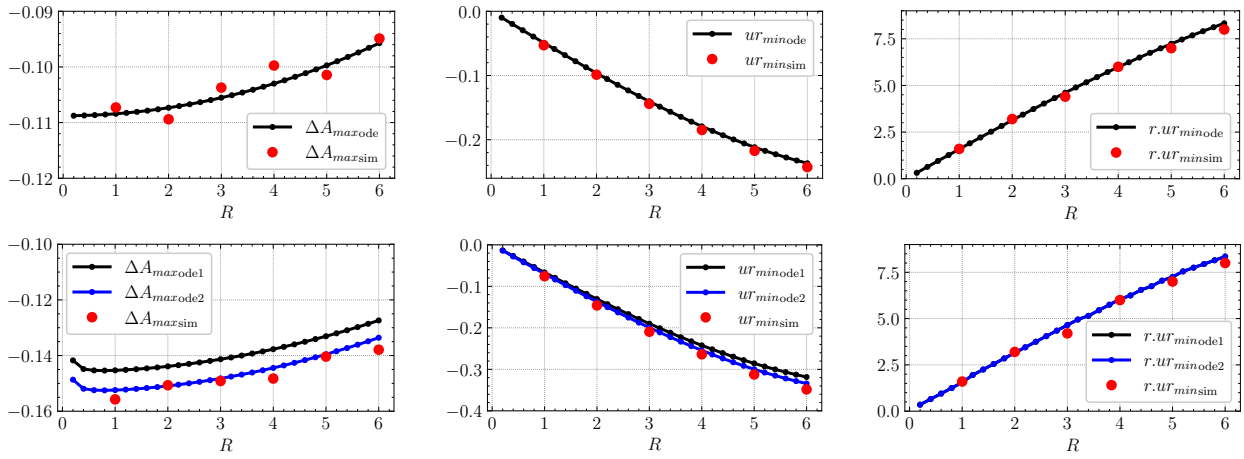

Figure 6.8: Comparison of the maximum area change (ΔA_{max}) (left), the minimum (radial) displacement (ur_{min}) (middle), and the distance at which the (radial) displacement is minimum ($r.ur_{min}$) (right), between the ODE solution (in black and blue) and the mean response of 30 different simulations in which we change the origin of the Gaussian function, using the low-disordered tissue (points in red), for the case of medial activity with $\alpha_A = -0.5$ and $\alpha_P = 0$ (up), and perimeter activity with $\alpha_A = 0$, $\alpha_{P\,sim} = -0.1$, and $\alpha_{P\,\mathrm{ode}} = -0.105$ (bottom).

6.5 Centered active force: temporal evolution

We propose a basic over-dumped dynamical equation for the displacement using the elastic tensor previously found for each case of activity (medial and perimeter), given by

$$\frac{\mathrm{d}u(r,t)}{\mathrm{d}t} = \nabla \cdot \sigma(r,t). \tag{6.44}$$

We solve this equation numerically, using as boundary conditions $u(0,t) = u(r,0) = u(R_{box},t) = 0$, and compare the temporal evolution of the same three observables as in the static case with respect to the vertex model simulations using the ordered tissue, for three different values of R: 4, 5, and 6.

6.5.1 Comparison with simulations

We find that the evolutions in the numerical simulations are slower than the evolutions obtained from solving the ODE for both medial and perimeter activity. We decide to plot the information using different timescales for both descriptions. In particular, Figs. 6.9 and 6.10 change the simulation timescale to $t' = 0.45t$, which is a value found by inspection. In 6.10 we also consider the two different perimeter contractility parameters described in the previous section. The non-smooth behavior of the $r.ur_{min}$ observable is given by the discretization of the space in the calculations. We observe a highly accurate agreement between the evolution of these observables in the two descriptions.

The proposed continuum equation for the temporal evolution of the tissue with an active Gaussian region reproduces with high precision the evolution generated by the numerical simulations of an ordered tissue. Different time-scales are used between the models, with a factor of 0.45, being the continuum description the fastest. We have no explanation for this factor. Also, different parameters of perimeter activity are used, being 5% stronger the active contractility of the continuum description.

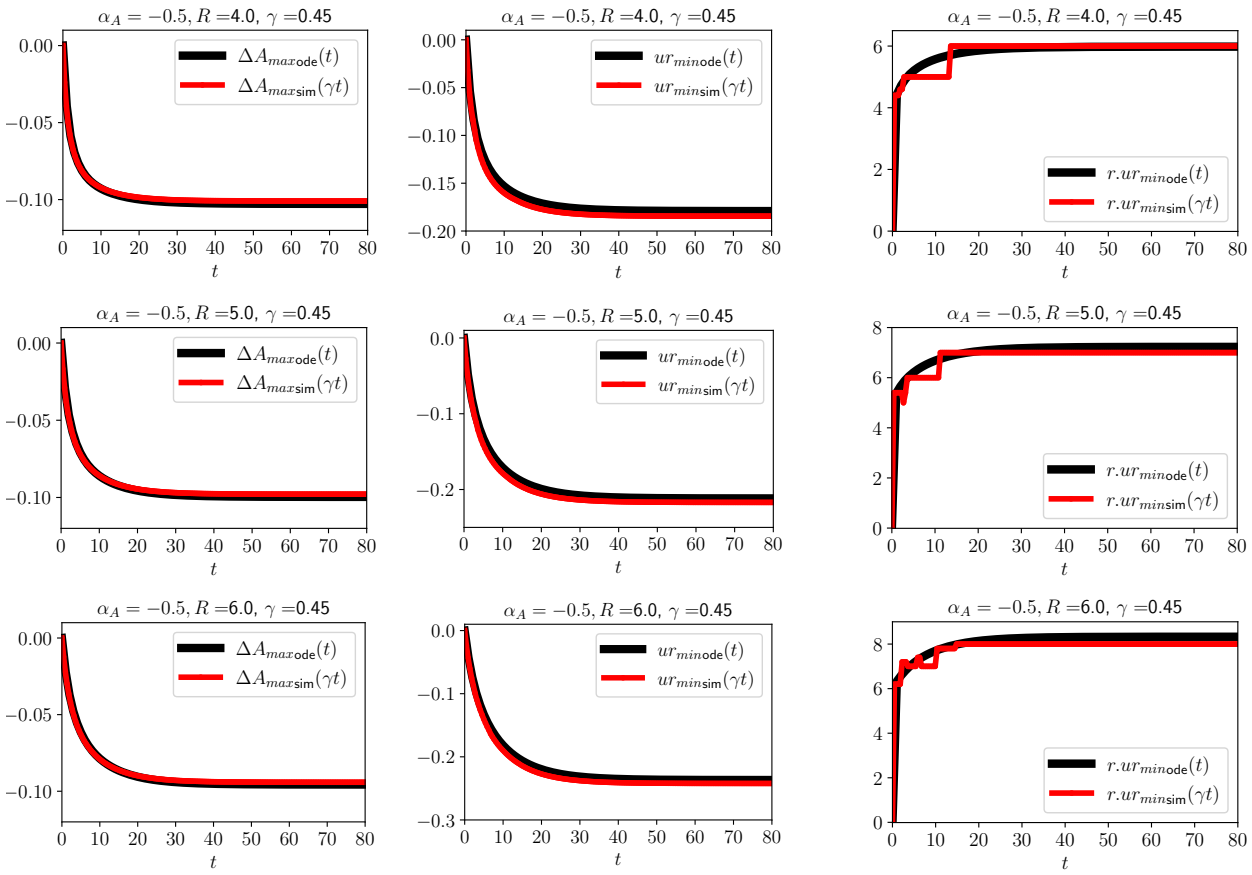

Figure 6.9: Temporal evolution of the maximum area change (ΔA_{max}) (left), the minimum (radial) displacement (ur_{min}) (middle), and the distance at which the (radial) displacement is minimum ($r.ur_{min}$) (right), between the ODE solution (in black) and the numerical simulations using vertex model with the ordered tissue (in red), for the case of medial activity with $\alpha_A = -0.5$ and $\alpha_P = 0$, for $R = 4$ (up), $R = 5$ (middle), and $R = 6$ (bottom). The simulation time-scale is changed to $t' = \gamma t$, with γ=0.45.

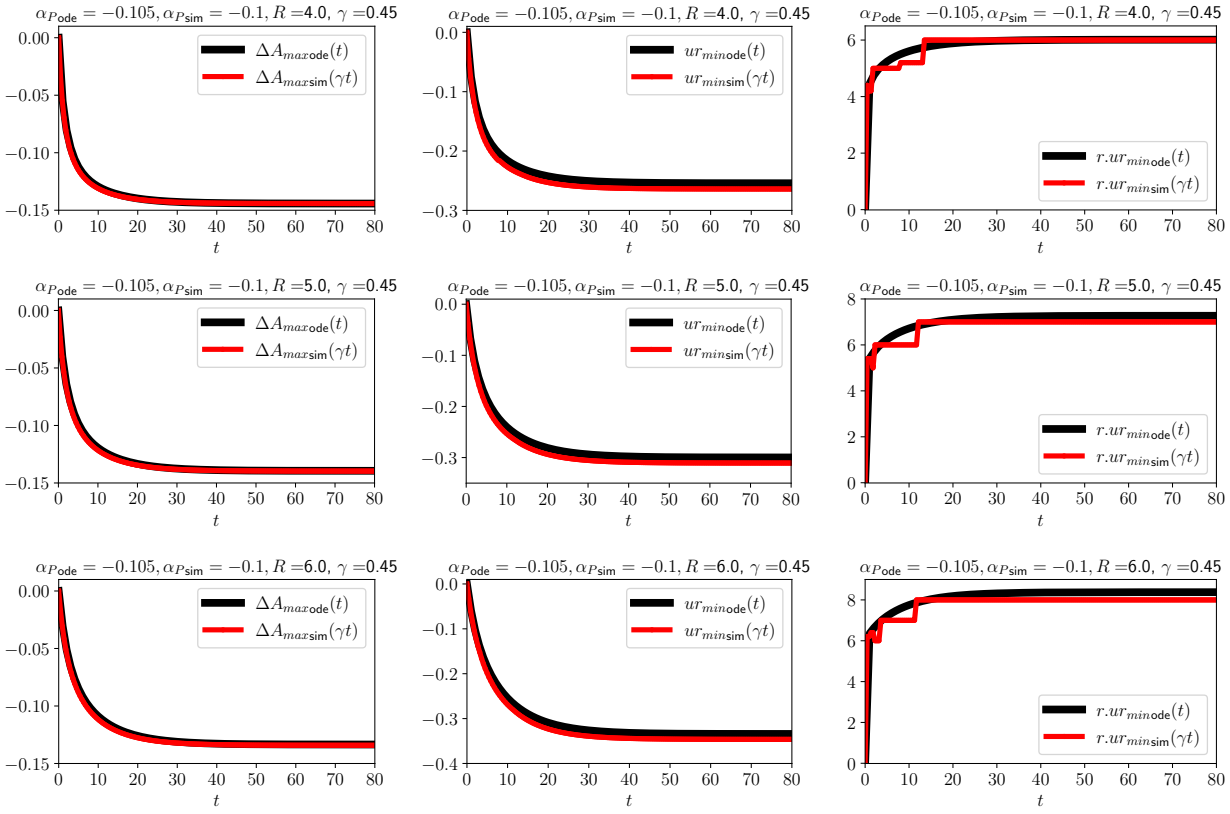

Figure 6.10: Same representation as in Fig. 6.9, when considering perimeter activity with $\alpha_A = 0$ and $\alpha_{Psim} = -0.1$ in the numerical simulations, and $\alpha_A = 0$ and $\alpha_{P\text{ode}} = -0.105$ in the ODE.

Chapter 7

Structure factors in active tissues

With the model described in the earlier sections, we characterize the response of a non-polarized plastic tissue under fluctuations induced by activity introduced at a cellular level. We do not perform any external stress on the system. From numerical simulations using different tissues, we study the behavior of the static structure factor of the velocity field. We find a scale separation, which informs us about the system's hydrodynamic scale, compression waves for the long-wavelength regime, and inverse energy cascade. We also study other structure factors related to the cells' geometrical properties, as contraction, anisotropy, and orientation.

7.1 Static structure factor: velocity field

We define the velocity field as

$$\mathbf{v}\left(\mathbf{r}\right) = \sum_{\mathrm{i}} \mathbf{v}_{\mathrm{i}} \delta\left(\mathbf{r} - \mathbf{r}_{\mathrm{i}}\right), \tag{7.1}$$

where the sum in over all the vertices of the tissue, and $\mathbf{r}_{\mathrm{i}}$ and $\mathbf{v}_{\mathrm{i}}$ correspond to the position and velocity of the vertex i, respectively. In Fourier space, the field is given by

$$\widetilde{\mathbf{v}}\left(\mathbf{k}\right) = \sum_{j} \mathbf{v}_{j} \mathrm{e}^{\mathrm{i}\mathbf{k}\cdot\mathbf{r}_{j}}. \tag{7.2}$$

From the previous expression we can define the parallel and perpendicular terms of this field, also called longitudinal and transverse, with respect to the wave-vector $\mathbf{k}$, as

$$\widetilde{v}_{\parallel}\left(\mathbf{k}\right) = \sum_{j} \left(\mathbf{v}_{j} \cdot \hat{\mathbf{k}}\right) \left[\cos\left(\mathbf{k}\cdot\mathbf{r}_{j}\right) + \mathrm{i}\sin\left(\mathbf{k}\cdot\mathbf{r}_{j}\right)\right], \tag{7.3}$$

$$\widetilde{v}_{\perp}\left(\mathbf{k}\right)=\sum_{j}\left[\mathbf{v}_{j}-\left(\mathbf{v}_{j}\cdot\hat{\mathbf{k}}\right)\hat{\mathbf{k}}\right]\cdot\hat{\mathbf{q}}_{\hat{\mathbf{k}}}\left[\cos\left(\mathbf{k}\cdot\mathbf{r}_{j}\right)+\mathrm{i}\sin\left(\mathbf{k}\cdot\mathbf{r}_{j}\right)\right], \tag{7.4}$$

where $\hat{\mathbf{k}}=\mathbf{k}/|\mathbf{k}|$ and $\hat{\mathbf{q}}_{\hat{\mathbf{k}}}$ is obtained by rotating $\hat{\mathbf{k}}$ in 90°.

Since our tissue is non-polarized, we expect the mean value of the expressions Eqs. (7.3) and (7.4), over different realizations, to be null. However, an interesting quantity – related to the energy of the system – is the mean value of the module squared. This way, we define a parallel and a perpendicular static structure factor for the velocity normalized by the number of vertices N_v, $S_{\parallel}$ and $S_{\perp}$, respectively, given by

$$S_{\parallel}\left(\mathbf{k}\right)=\frac{1}{N_{v}}\left\langle \left[\sum_{\mathrm{i}}\left(\mathbf{v}_{\mathrm{i}}\cdot\hat{\mathbf{k}}\right)\cos\left(\mathbf{k}\cdot\mathbf{r}_{\mathrm{i}}\right)\right]^{2}+\left[\sum_{\mathrm{i}}\left(\mathbf{v}_{\mathrm{i}}\cdot\hat{\mathbf{k}}\right)\sin\left(\mathbf{k}\cdot\mathbf{r}_{\mathrm{i}}\right)\right]^{2}\right\rangle, \tag{7.5}$$

$$\begin{aligned}S_{\perp}\left(\mathbf{k}\right)=&\frac{1}{N_{v}}\left\langle \left[\sum_{\mathrm{i}}\left(\mathbf{v}_{\mathrm{i}}-\left(\mathbf{v}_{\mathrm{i}}\cdot\hat{\mathbf{k}}\right)\hat{\mathbf{k}}\right)\cdot\hat{\mathbf{q}}_{\hat{\mathbf{k}}}\cos\left(\mathbf{k}\cdot\mathbf{r}_{\mathrm{i}}\right)\right]^{2}+\right.\\&\left.\left[\sum_{\mathrm{i}}\left(\mathbf{v}_{\mathrm{i}}-\left(\mathbf{v}_{\mathrm{i}}\cdot\hat{\mathbf{k}}\right)\hat{\mathbf{k}}\right)\cdot\hat{\mathbf{q}}_{\hat{\mathbf{k}}}\sin\left(\mathbf{k}\cdot\mathbf{r}_{\mathrm{i}}\right)\right]^{2}\right\rangle.\end{aligned} \tag{7.6}$$

These quantities are directly related to the kinetic energy of the system. When looking in the wave-vector space or direct space, they inform about the transfer energy between different scales.

7.2 General considerations for the simulations

In this part, we perform numerical simulations to study the response of a non-polarized tissue, with memory (as described in Ch. 2), under fluctuations that enters as creation of equilibrium area and perimeter. We do not perform any deformation or external stress on the system, so we assume that the evolution of the equilibrium perimeters is around the initial values, A_{00c} and P_{00c}, for the area and perimeter, respectively. Then, the equations look like

$$\frac{\mathrm{d}A_{0c}}{\mathrm{d}t}=-\nu_{A}\left(A_{0c}-A_{00c}\right)+\sqrt{2D_{Ac}}\xi_{A_{c}}, \tag{7.7}$$

$$\frac{\mathrm{d}P_{0c}}{\mathrm{d}t}=-\nu_{P}\left(P_{0c}-P_{00c}\right)+\sqrt{2D_{Pc}}\xi_{P_{c}}. \tag{7.8}$$

We define $D_{Ac} = \frac{1}{2}\left(d_A A_{00c}\right)^2$ and $D_{Pc} = \frac{1}{2}\left(d_P P_{00c}\right)^2$, and decide to simplify the system by taking $d_A = d_P = d = 0.1$. We use a fixed set of elastic parameters that represent a stable system, $K_A = 1$, $K_P = 1$ and $J = 1$, keeping $\nu_A = \nu_P = 1$. For the numerical integration we use the Euler method with a $dt = 0.01$.

From the previous chapters, we have seen that the contraction R and the change of anisotropy Q of each cell are important functions to describe the response of the tissue under activity, reason why for every simulation we also show the behavior of them. For a c cell, these quantities are given by

$$R_c = \frac{A_{0c}(t=0) - A_c}{A_{0c}(t=0)}, \tag{7.9}$$

$$Q_c = \frac{b_c(t=0)}{a_c(t=0)} - \frac{b_c}{a_c}, \tag{7.10}$$

where a_c and b_c have the same meaning as in Ch. 3 (Sec. 3.1).

To study the structure factor of the velocity field, we use five tissues (Tab. 7.1): ordered and disordered, with different number of cells. Disordered tissues are created following the procedure specified in Ch. 3. All of them obey periodic boundary conditions. For the analysis we use 40 snapshots, evenly spaced, between $t = 5$ and $t = 25$. The evolution from $t = 0$ to $t = 5$ is considered as a relaxation stage.

Tissue	L_x	L_y	**Nº cells**	**Shape of cells**
T1.1	$19\sqrt{3}$	39	494	Regular hexagons of unitary side
T1.2	$19\sqrt{3}$	39	494	Disordered
T2.1	$50\sqrt{3}$	90	3000	Regular hexagons of unitary side
T2.2	$50\sqrt{3}$	90	3000	Disordered
T3	30	30	900	Squares of unitary side

Table 7.1: Different tissues considered for numerical simulations.

For every tissue, we define the possible wave-vectors as $\mathbf{k} = k_x\hat{\mathbf{x}} + k_y\hat{\mathbf{y}}$, where

$$k_x = \frac{2\pi}{L_x}m, \qquad k_y = \frac{2\pi}{L_y}n \tag{7.11}$$

with $m, n \in \mathbb{Z}$, and L_x and L_y described in Tab. 7.1.

We are interested in the response of the tissue in scales from one cell – where energy is injected – to several cells. This allows us to compute only up to a specific value of k_x and k_y ($k \sim 2\pi$ for squared cells and $k \sim \pi$ for hexagonal cells) since larger ones would tell us about the microscopical network topology.

Figures 7.1, 7.2, 7.3, 7.4, 7.5 show the temporal fluctuations of the two target parameters, and the evolution of the cellular contraction and change on anisotropy of all the cells in the simulations of each tissue (Tab. 7.1). The four quantities fluctuate in limited ranges. The figures also show the spatial distribution of these quantities at $t = 10$.

From the ordered tissues, Figs. 7.6, 7.8 and 7.10 we see that there exists a critical wavevector k^* that separates two regimes: a long-wavelength regime with an isotropic response and a small wavelength regime with an anisotropic response. In the long-wavelength regime there are longitudinal waves (compressional waves). Instead, perpendicular waves are null. Tissues made of regular hexagons that only differ in the number of cells (Figs. 7.6 and 7.8) produce similar results for the structure factors of the velocity fields, with a smoother curve in the bigger tissue (Fig. 7.8). When comparing the results from a tissue made of regular hexagons versus squares, we find that in the intensity of the longitudinal structure factor $S_{\parallel}$ is bigger in the first case (~ 1.67 times the one from the tissue made of squares).

From the disordered tissues, Figs. 7.7 and 7.9, we obtain that both regimes – small and large wavelength – produce isotropic responses. Unlike the ordered case, there are perpendicular waves in the small wavelength regime but always smaller than the compressional waves. The critical wavevector k^* that describes the scale separation is within the range found for the ordered tissue, due to the homogenization induced by the disorder. The results for both disordered tissues are similar, with a smoother curve in the bigger tissue (Fig. 7.9).

In Figs. 7.11-a and b we show, as an approximation, the zone (red zone) covered by the critical wavevector k^* for a tissue made of square and hexagonal cells, respectively. Note that two red circles are shown for each case, giving a range for k^*, due to the non-isotropic geometry of $S_{\parallel}(\mathbf{k})$. In both cases, the red zone is of the order of one cell. Also, in the same figure, the green zones represent, as an approximation, the region covered by the wavelength that produces the maximum intensity of compressional waves. All this information tells us about the presence of an inverse energy cascade. The input of energy on a small scale – one cell – is producing movements with high fluctuations in the velocities on a larger scale. For disordered tissues, the critical wavevector k^* that describe the scale separation is within the range found for the hexagonal ordered tissue, due to the homogenization induced by the disorder. The zone covered by k^* is still of the order of one cell (Fig. 7.11-c), and the green zone remains unchanged.

7.3 Structure factors of cellular fields: S_R, S_Q and S_ϕ

We also study other structure factors, using specific geometrical properties of the cells as the contraction R_c and the change of anisotropy Q_C, previously defined, and the angle of orientation ϕ_c, defined as the angle form by $\hat{\mathbf{x}}$ and $\boldsymbol{a}_c$ (major axis vector). For this part, we use $\mathbf{r}_c$ as the position of the center of the cell c.

We define the following fields,

$$R(\mathbf{r}) = \sum_c R_c \delta(\mathbf{r} - \mathbf{r_c}) \Longrightarrow \tilde{R}(\mathbf{k}) = \sum_c R_c \mathrm{e}^{\mathrm{i}\mathbf{k}\cdot\mathbf{r_c}}, \tag{7.12}$$

$$Q(\mathbf{r}) = \sum_c Q_c \delta(\mathbf{r} - \mathbf{r_c}) \Longrightarrow \tilde{Q}(\mathbf{k}) = \sum_c Q_c \mathrm{e}^{\mathrm{i}\mathbf{k}\cdot\mathbf{r_c}}, \tag{7.13}$$

$$\phi(\mathbf{r}) = \sum_c \mathrm{e}^{2\mathrm{i}\phi_c} \delta(\mathbf{r} - \mathbf{r_c}) \Longrightarrow \tilde{\phi}(\mathbf{k}) = \sum_c \mathrm{e}^{2\mathrm{i}\phi_c} \mathrm{e}^{\mathrm{i}\mathbf{k}\cdot\mathbf{r_c}}, \tag{7.14}$$

where the sums are over the cells c, and we use the factor $\mathrm{e}^{2\mathrm{i}\phi_c}$ since the orientation is defined by an apolar axis, and hence $\phi_c \equiv \phi_c + \pi$.

We study the following structure factors, normalized by the number of cells N_c,

$$S_R(\mathbf{k}) = \frac{1}{N_c} \langle |\tilde{R} - \langle \tilde{R} \rangle|^2 \rangle, \tag{7.15}$$

$$S_Q(\mathbf{k}) = \frac{1}{N_c} \langle |\tilde{Q} - \langle \tilde{Q} \rangle|^2 \rangle, \tag{7.16}$$

$$S_\phi(\mathbf{k}) = \frac{1}{N_c} \langle |\tilde{\phi} - \langle \tilde{\phi} \rangle|^2 \rangle. \tag{7.17}$$

Figure 7.12 shows the results for the regular tissue T2.1. We can see that the contraction structure factor S_R is a random variable, but uniform in average in all the analyzed k-space, which tells us that the correlation function of the net contraction field is a delta function in

r-space. That is to say, the contraction of each cell is an uncorrelated characteristic. S_Q, associated to the anisotropy, has a small and not well-defined peak for small k. At $(k_x, k_y = 0, 0)$ and at some points with $k \sim 4$ the anisotropy structure factor take values of the order of 10^7. This happens since the wavevectors $\mathbf{k}_1 = (0, \pm 4\pi/3)$ and $\mathbf{k}_2 = (\pm 2\pi/\sqrt{3}, \pm 2\pi/3)\}$ are vector of the reciprocal lattice. This can been seen by defining two principal vectors of the lattice that form the cellular centers, $\mathbf{a}_1 = (\sqrt{3}, 0)$ and $\mathbf{a}_2 = (\sqrt{3}/2, 3/2)$. Then, two reciprocal vector are $\mathbf{b}_1 = (2\pi/\sqrt{3})$ and $\mathbf{b}_2 = (0, 4\pi/3)$, i.e., $b_i a_j = 2\pi\delta_{ij}$. Finally, $\mathbf{k}_1$ and $\mathbf{k}_2$ are linear combinations of the style $n_1\mathbf{b}_1 + n_2\mathbf{b}_2$, with n_1, n_2 integers.

In average, it looks uniform from the scale of one cell to several cells. Then, the change of the anisotropy of cells might also be considered as an uncorrelated variable. The orientation structure factor S_ϕ changes from isotropic to anisotropic at $k \sim 1.5$ ($\lambda \sim 4.2$, with λ the wavelength), which is similar to the wavevector at which the intensity of the longitudinal structure factor $S_\parallel$ is maximum. Also, a peak of intensity is obtained at $k \sim 0.9$ ($\lambda \sim 7$).

Figure 7.13 shows the results for the irregular tissue T2.2. Now, S_R has a maximum of intensity for small k, $k \sim 0.2$ ($\lambda \sim 31.4$). S_ϕ remains with a peak for small k, now moved to an even smaller value of k (very similar to the one of S_R). S_Q now has a maximum at $k \sim 4$, which correspond to the cellular characteristic length and, also to the critical wavevector we found in the analysis of the longitudinal structure factor $S_\parallel$. For smaller k, in average, S_Q maintain the uniform character.

Unlike the case of the longitudinal and transversal structure factors that the only difference between the results in ordered and disordered tissues is the smoothness of the curves, the structure factors related with the cellular contraction S_R, the change of cellular anisotropy S_Q, and the cellular orientation S_ϕ, change qualitatively and quantitively.

Taking all the information together, we obtain that in ordered tissues the input of activity at a cellular level causes compression waves in a larger scale. The maximum of kinetic energy is produced with fluctuations characterized by wavevectors around $k \sim 1.5$. The motion of the vertices produces local cellular contractions and changes of cellular anisotropy, with no correlation between cells. However, there is a clear correlation in the cellular orientation, with a characteristic wavevector also around $k \sim 1.5$. In the case of disordered tissues, beside the compression waves with a maximum around $k \sim 1.5$, the input of cellular activity also causes perpendicular waves, with values of one order of magnitud smaller. The correlation in the cellular orientation is still present, but the characteristic wavevector is moved to smaller values ($k \sim 0.2 \iff \lambda \sim 31.4 \iff \sim 17$ cells). For the same wavevector, now appears a correlation in the cellular contraction. The values of S_Q are two orders of magnitude larger than in the ordered tissue, and now this structure factor has a clear correlation at the scale of input of energy. These results conclude that geometrical quantities related to the contraction and orientation are good candidates for being treated as fields in a long-wavelength hydrodynamic theory of our system.

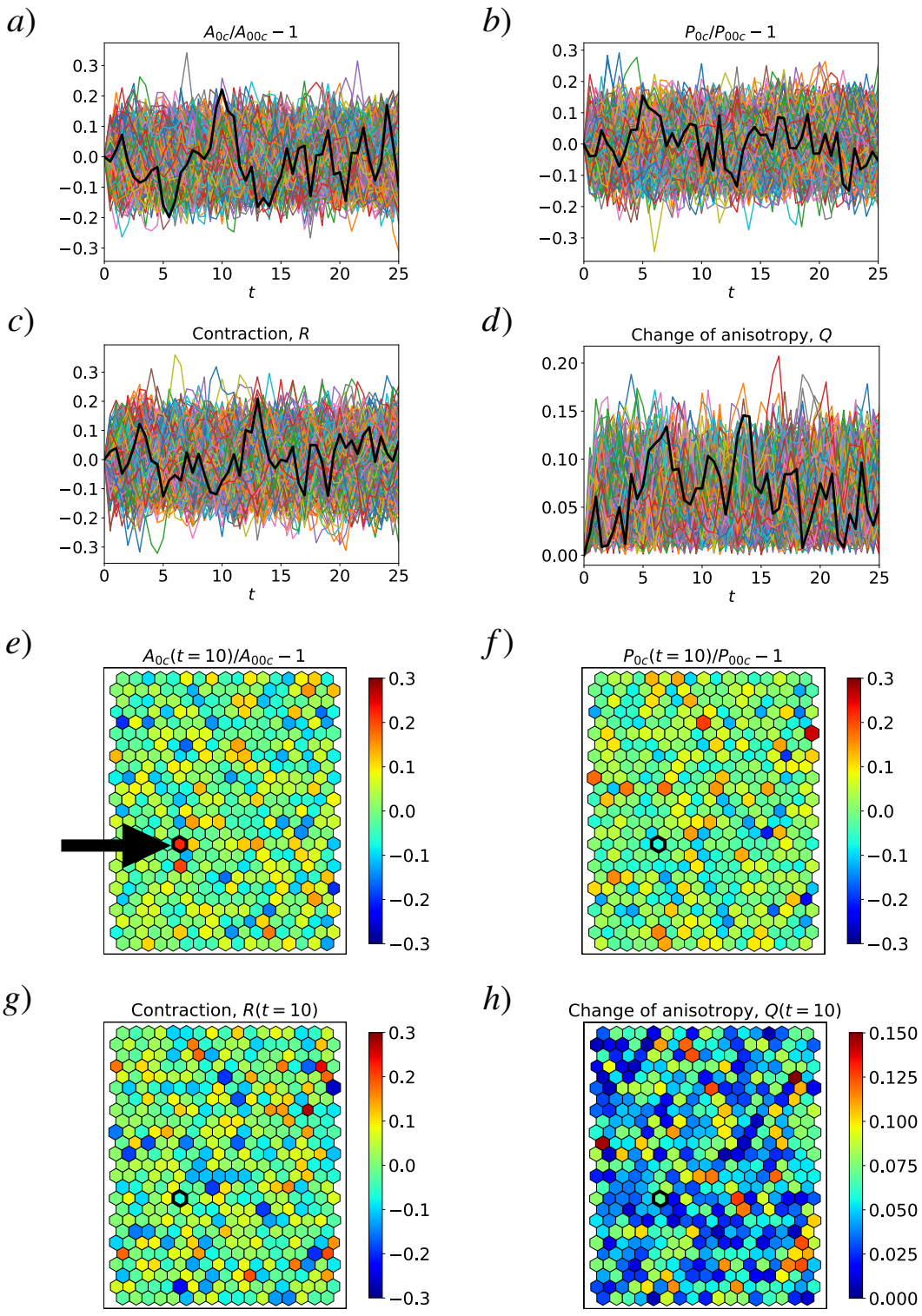

Figure 7.1: Numerical simulations results for the Tissue 1.1, composed of 494 regular hexagonal cells of unitary side, with fluctuations characterized by $d = 0.1$, elastic parameters $K_A = 1, K_P = 1$ and $J = 1$, and memory parameters $\nu_A = \nu_P = 1$. a)-b) Time evolution of the equilibrium areas and perimeters, normalized by their initial values, minus one. c)-d) Time evolution of the contraction R and change of anisotropy Q of each cell. e)-h) Color maps of the quantities shown in a)-d) at $t = 10$. The black thick curves shown in a)-d) correspond to the evolution of the cell pointed with the black arrow in e), that has a thick black contour in e)-h).

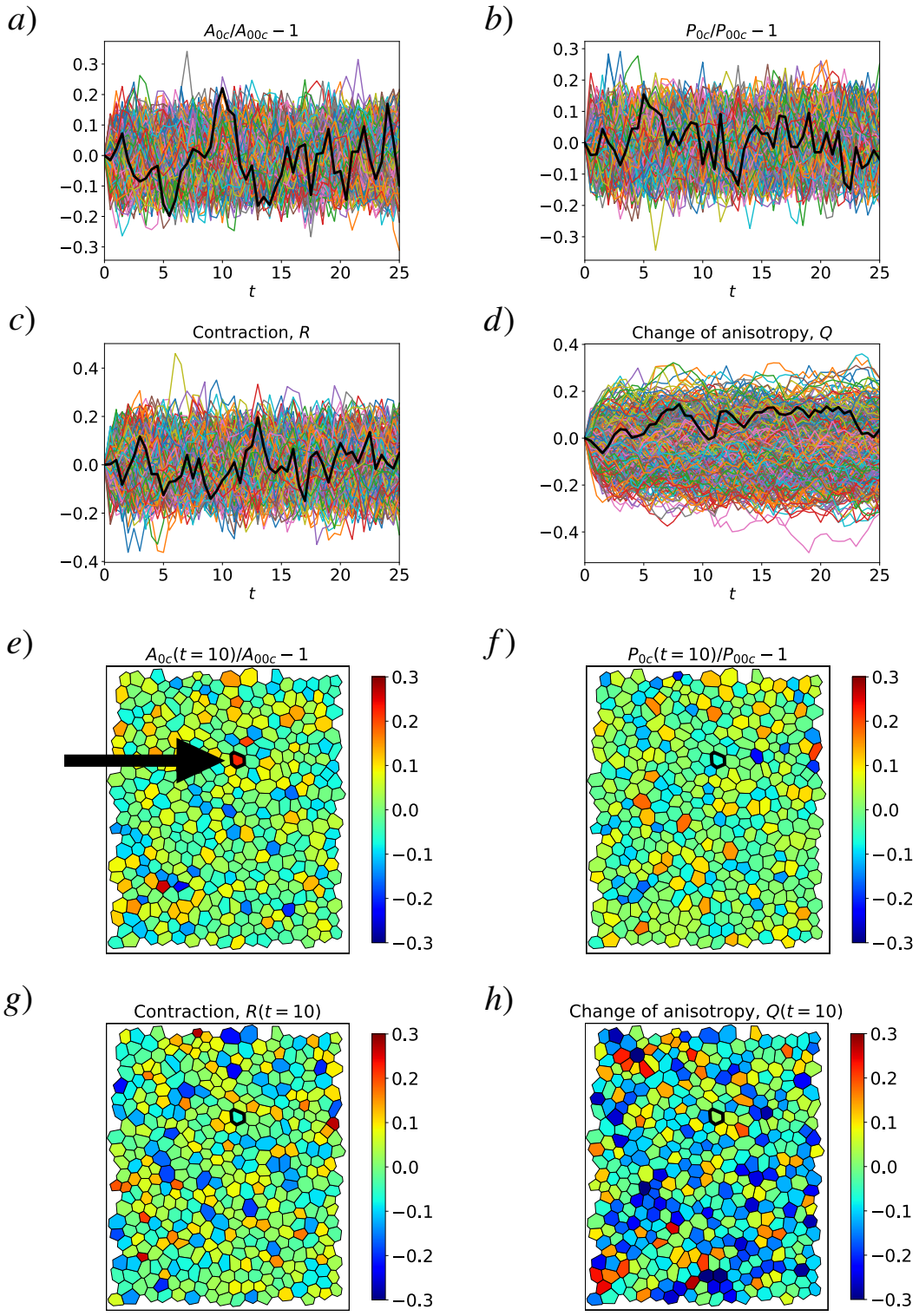

Figure 7.2: Numerical simulations results for the Tissue 1.2, composed of 494 cells of various polygons, with fluctuations characterized by $d = 0.1$, elastic parameters $K_A = 1, K_P = 1$ and $J = 1$, and memory parameters $\nu_A = \nu_P = 1$. Same representation as in Fig.7.1.

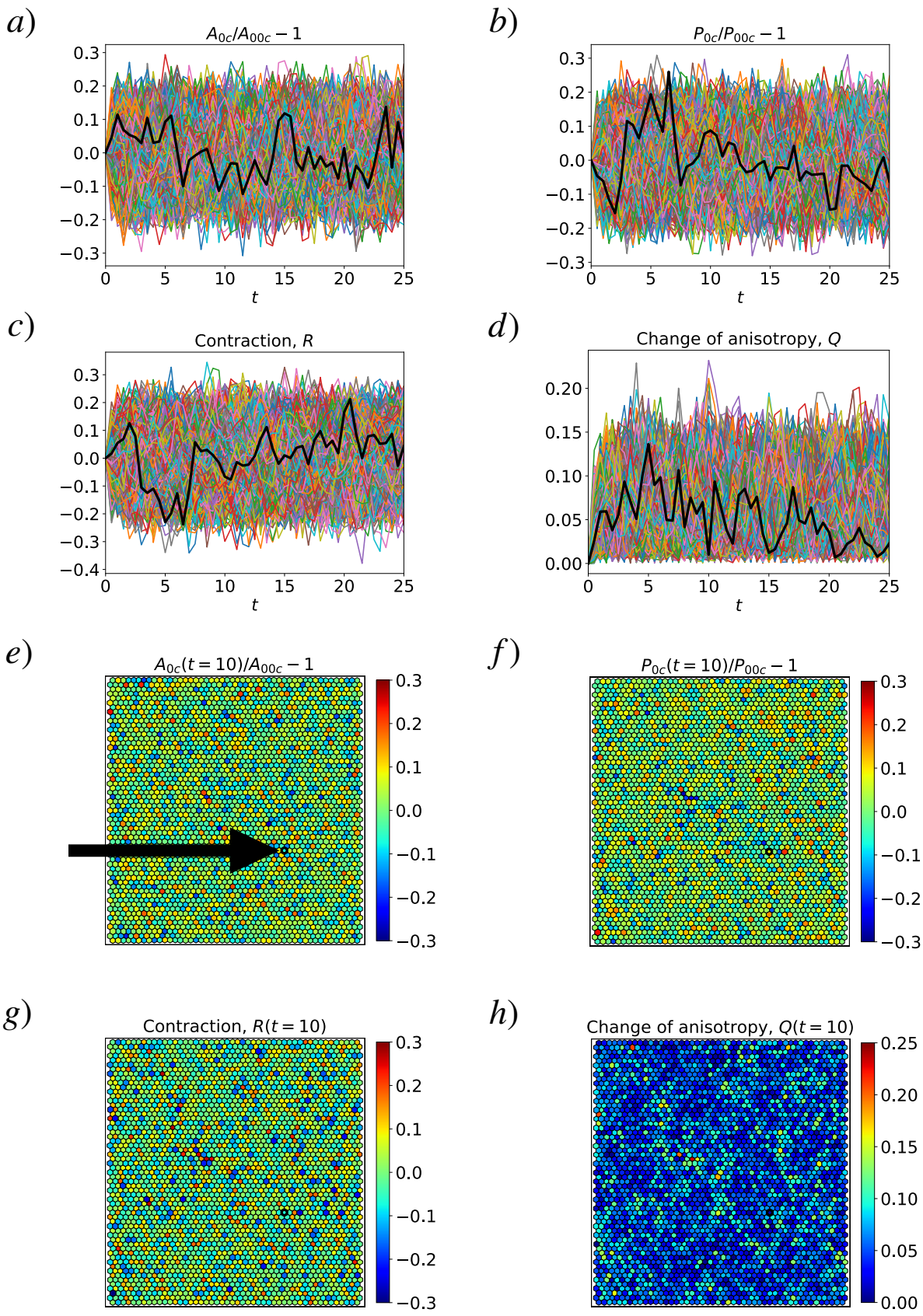

Figure 7.3: Numerical simulations results for the Tissue 2.1, composed of 3000 regular hexagonal cells of unitary side, with fluctuations characterized by $d = 0.1$, elastic parameters $K_A = 1, K_P = 1$ and $J = 1$, and memory parameters $\nu_A = \nu_P = 1$. Same representation as in Fig.7.1.

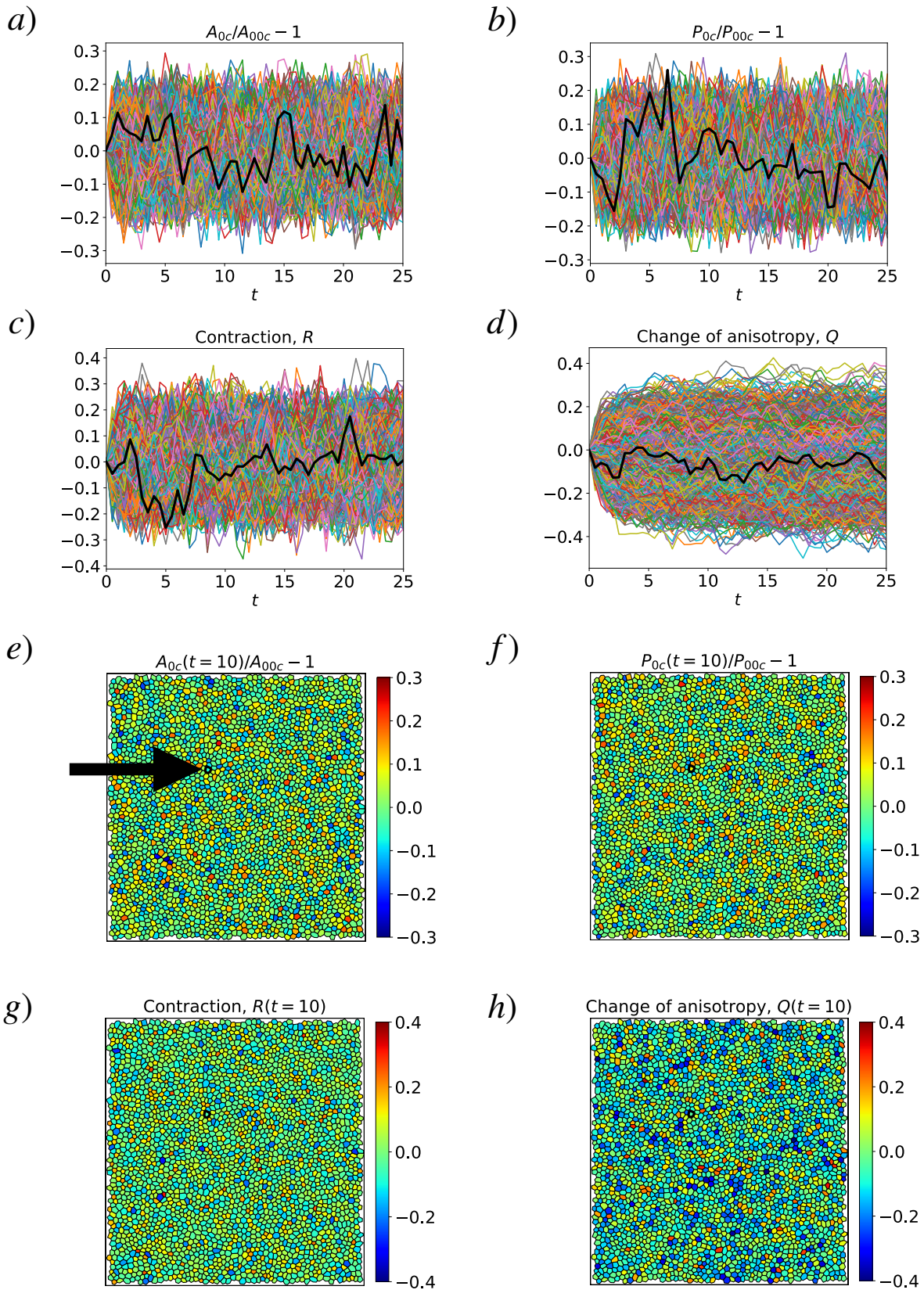

Figure 7.4: Numerical simulations results for the Tissue 2.2, composed of 3000 cells of various polygons, with fluctuations characterized by $d = 0.1$, elastic parameters $K_A = 1, K_P = 1$ and $J = 1$, and memory parameters $\nu_A = \nu_P = 1$. Same representation as in Fig.7.1.

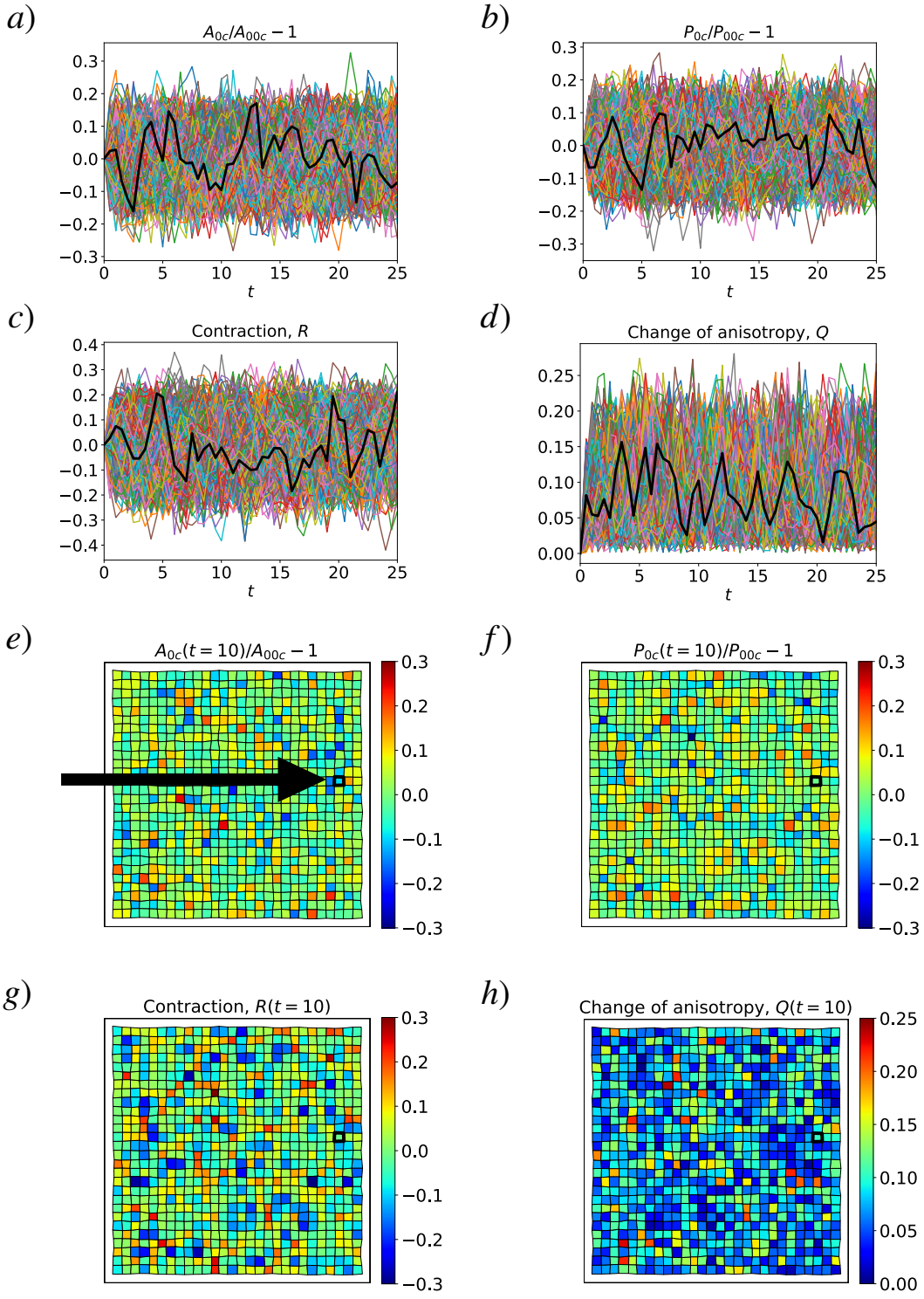

Figure 7.5: Numerical simulations results for the Tissue 3, composed of 900 regular squared cells of unitary side, with fluctuations characterized by $d = 0.1$, elastic parameters $K_A = 1, K_P = 1$ and $J = 1$, and memory parameters $\nu_A = \nu_P = 1$. Same representation as in Fig.7.1.

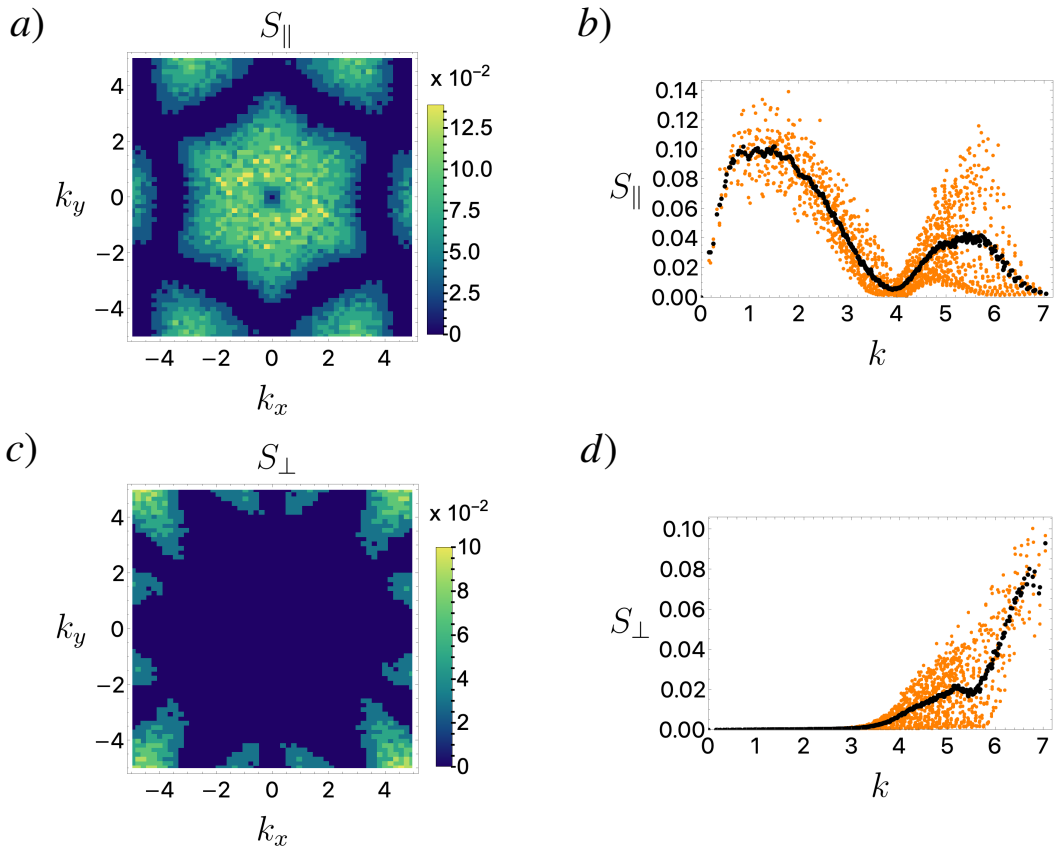

Figure 7.6: Numerical simulations results for the Tissue 1.1, composed of 494 regular hexagonal cells of unitary side, with fluctuations characterized by $d = 0.1$, elastic parameters $K_A = 1, K_P = 1$ and $J = 1$, and memory parameters $\nu_A = \nu_P = 1$. a)-b) Two representations of the parallel component of the static structure factor of the velocity field, calculated using 25 snapshots, evenly spaced, between $t = 5$ and $t = 25$. Black points in b) are the mean value calculated from the orange points, using a moving window of $\Delta k = 0.1$. c)-d) Two representations of the perpendicular component of the static structure factor of the velocity field, following the same protocol as for a)-b).

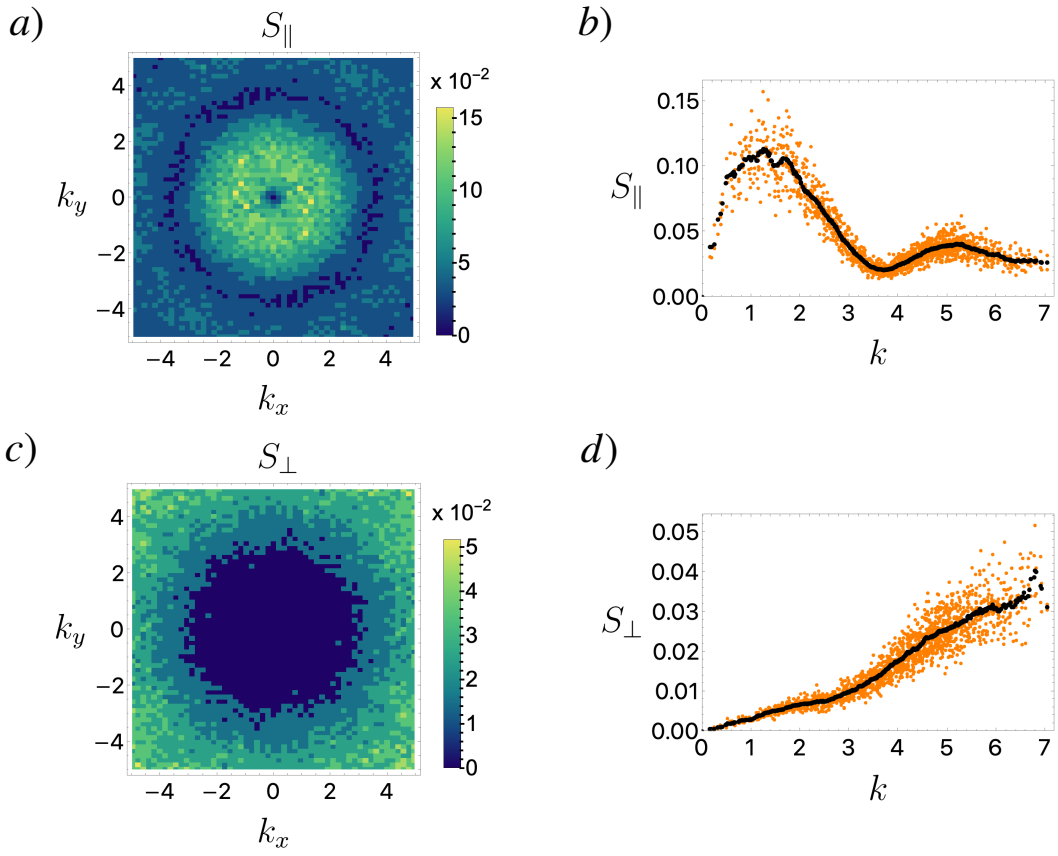

Figure 7.7: Numerical simulations results for the Tissue 1.2, composed of 494 cells of various polygons, with fluctuations characterized by $d = 0.1$, elastic parameters $K_A = 1, K_P = 1$ and $J = 1$, and memory parameters $\nu_A = \nu_P = 1$. Same representation as in Fig.7.6.

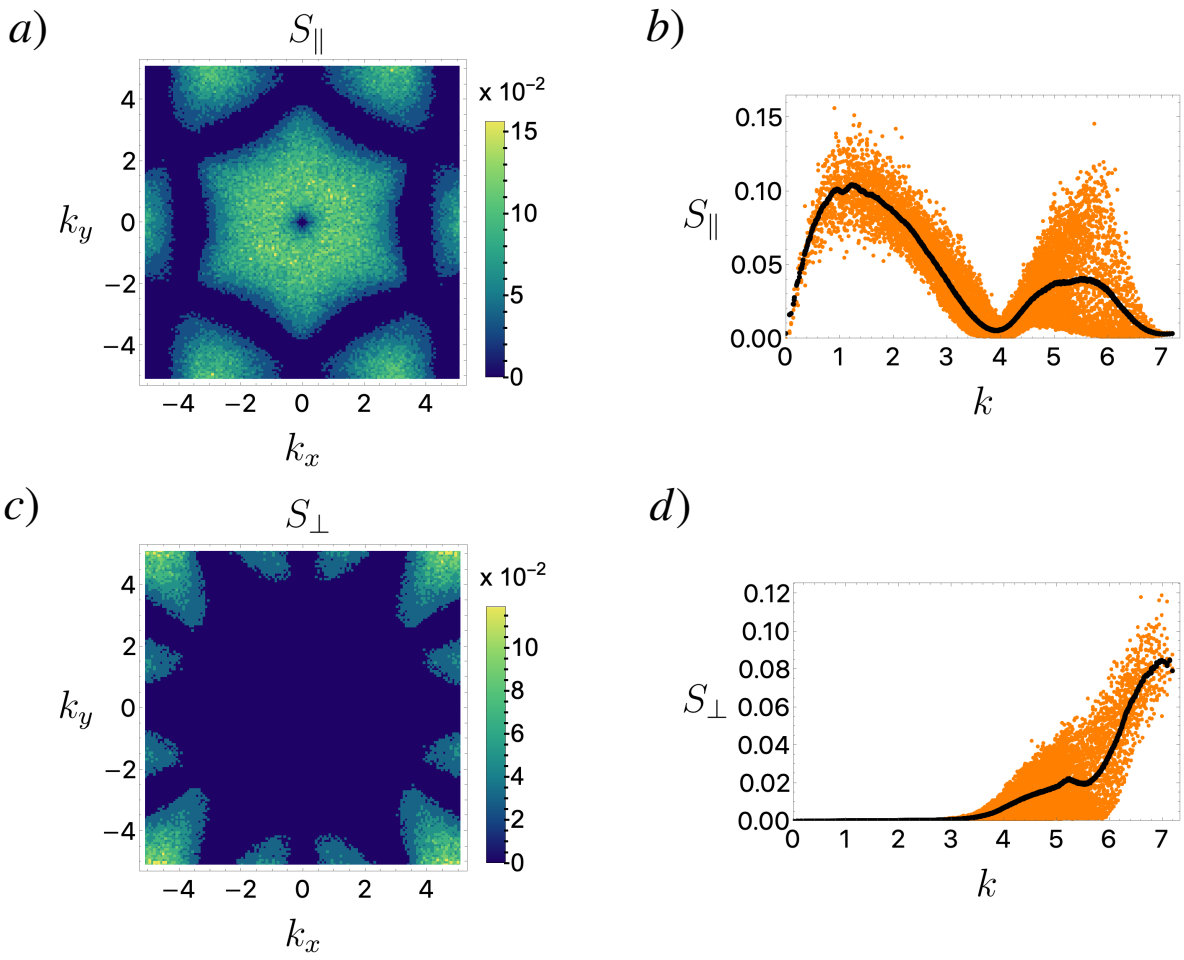

Figure 7.8: Numerical simulations results for the Tissue 2.1, composed of 3000 regular hexagonal cells of unitary side, with fluctuations characterized by $d = 0.1$, elastic parameters $K_A = 1, K_P = 1$ and $J = 1$, and memory parameters $\nu_A = \nu_P = 1$. Same representation as in Fig.7.6.

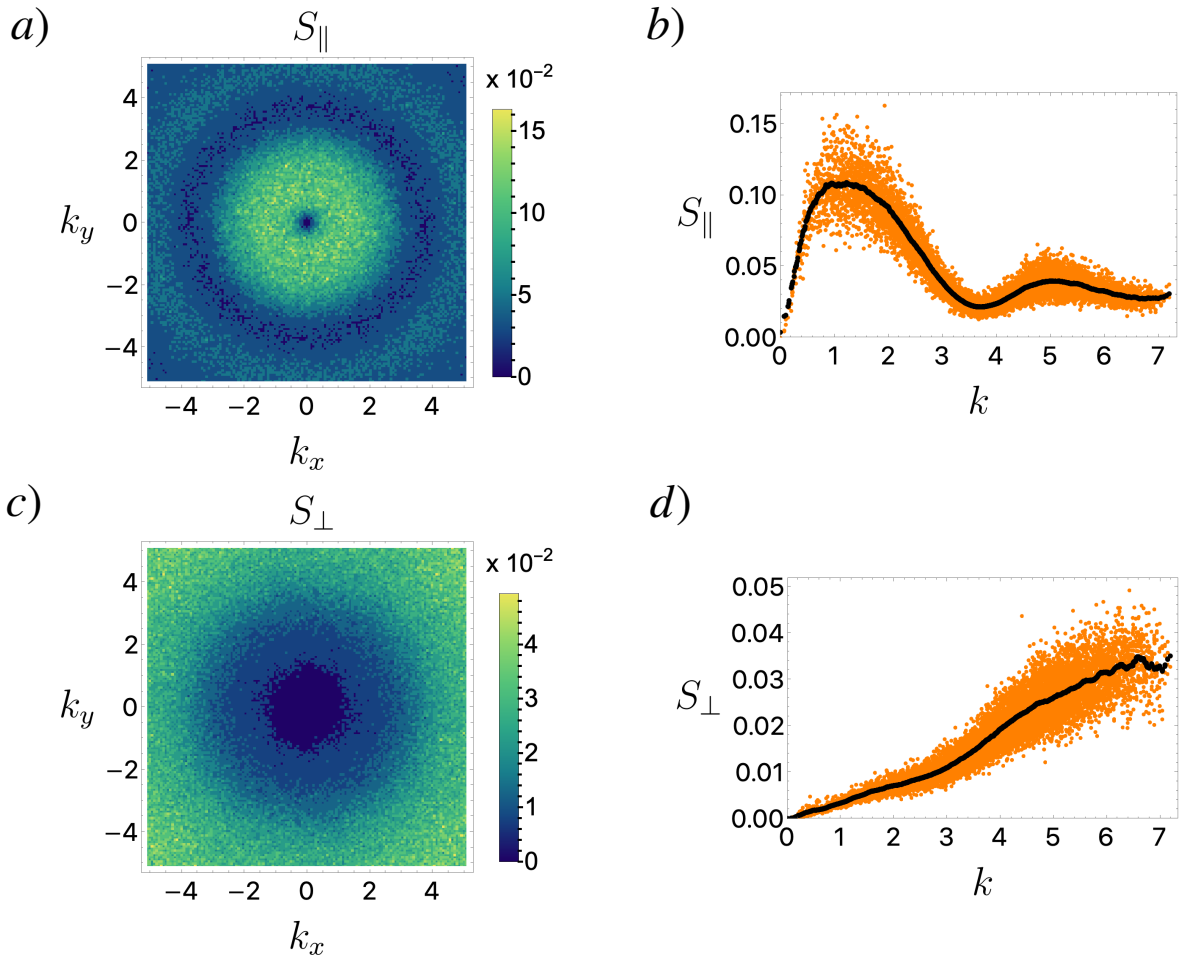

Figure 7.9: Numerical simulations results for the Tissue 2.2, composed of 3000 cells of various polygons, with fluctuations characterized by $d = 0.1$, elastic parameters $K_A = 1, K_P = 1$ and $J = 1$, and memory parameters $\nu_A = \nu_P = 1$. Same representation as in Fig.7.6.

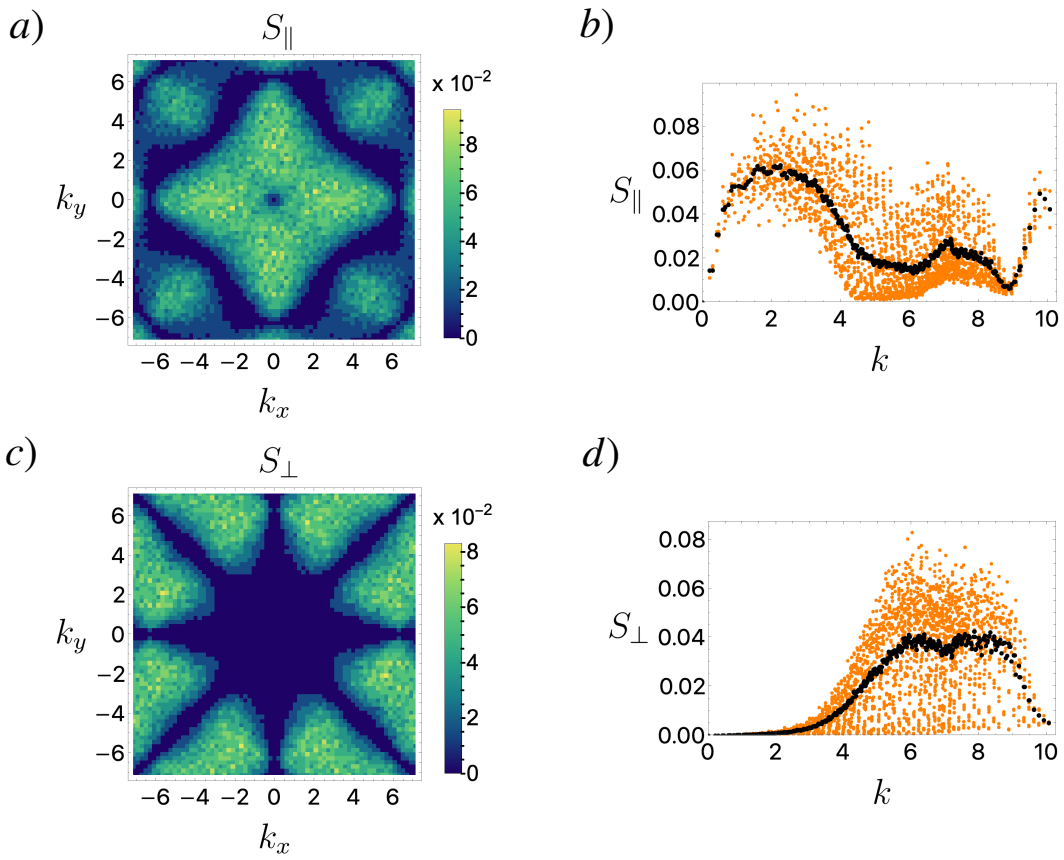

Figure 7.10: Numerical simulations results for the Tissue 3, composed of 900 regular squared cells of unitary side, with fluctuations characterized by $d = 0.1$, elastic parameters $K_A = 1, K_P = 1$ and $J = 1$, and memory parameters $\nu_A = \nu_P = 1$. Same representation as in Fig.7.6.

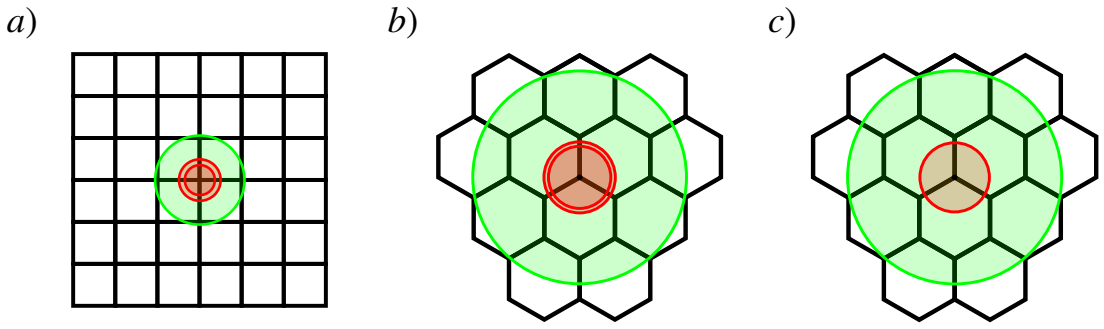

Figure 7.11: A brief summary of the scale separation for the tissues a) T3, b) T2.1, and c) T2.2, described in Tab. 7.1. The red zones indicate the approximate critical wavevector k^* that separates small and long wavelength regimes. For ordered tissues, a) and b), it also separates isotropic from the anisotropic response. The green zones indicate the approximate wavelength at which the intensity of the longitudinal structure factor $S_{\parallel}$ is maximum.

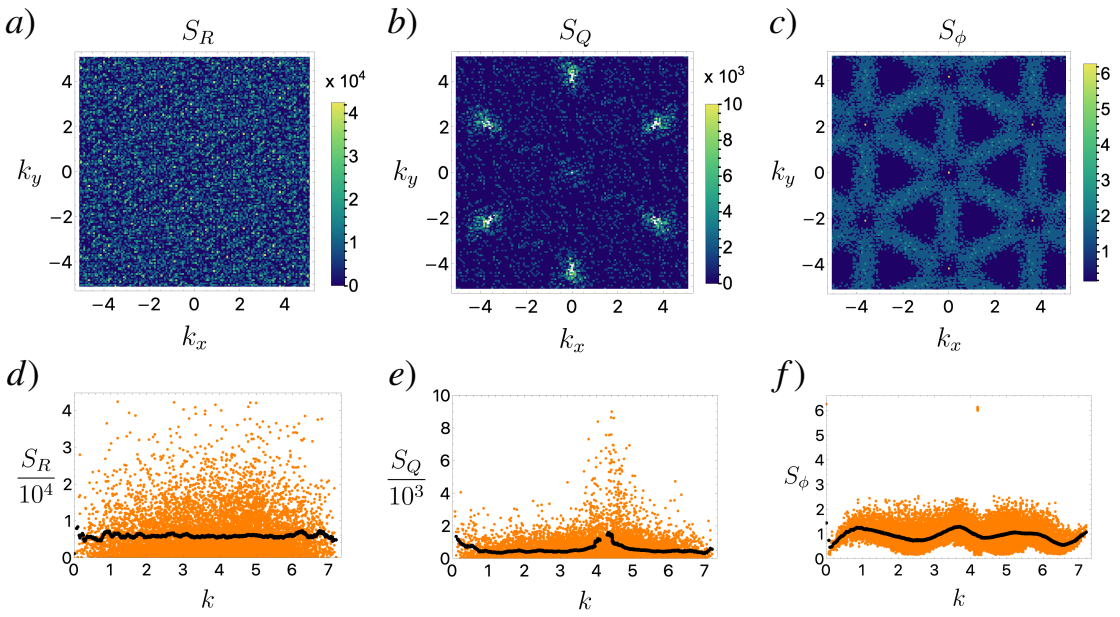

Figure 7.12: Numerical simulations results for the Tissue 2.1, composed of 3000 regular hexagonal cells of unitary side, with fluctuations characterized by d = 0.1, elastic parameters $K_A = 1, K_P = 1$ and $J = 1$, and memory parameters $\nu_A = \nu_P = 1$. a-d) Two representations of the static structure factor of contraction S_R. b-e) Two representations of the static structure factor of anisotropy S_Q. White dots in b) correspond to higher values, of the order of 10^7; the respective **k** correspond to vectors of the reciprocal lattice. Those points are not shown in e). c-f) Two representations of the static structure factor of contraction S_ϕ. For all the figures, the quantities were calculated using 25 snapshots, evenly spaced, between $t = 5$ and $t = 25$.

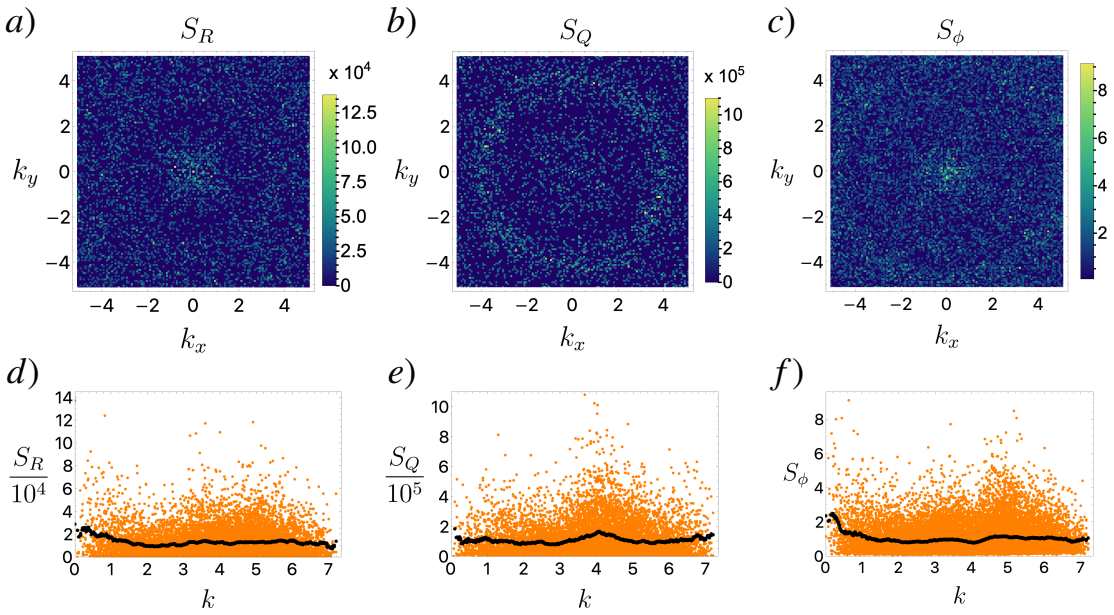

Figure 7.13: Numerical simulations results for the Tissue 2.2, composed of 3000 cells of various polygons, with fluctuations characterized by d = 0.1, elastic parameters $K_A = 1, K_P = 1$ and $J = 1$, and memory parameters $\nu_A = \nu_P = 1$. Same representation as in Fig. 7.12. For $(k_x, k_y) = (0, 0)$, S_Q is of the order of 10^7. That point is shown in white in b) and does not appear in e).

Conclusions

During the last decades epithelial tissues, an example of active matter, have been analyzed using models initially proposed for foams and bubbles in physics. In this thesis we describe two-dimensional planar epithelial tissues physically, using a model in which no direction of motion is imposed, and hence where the activity enters as a scalar quantity. We use a simple system in which neither cell division nor cell rearrangements are considered, which is the case seen in some biological experiments.

Using the vertex model, we showed that when the perimeter region of the cells is active, or the tissue is subject to different external stresses, the tissue becomes unstable with deformations that couple certain modes. When there is no activity in the medial zone, the instability is directly related to a vanishing shear modulus, and we obtain the same threshold reported in literature. We expect that these instabilities will be tested in experiments, as a tool for validating the use of the vertex model to correctly describe these biological systems. These results are published in the article "Vertex model instabilities for tissues subject to cellular activity or applied stresses", Ref. [59]. A natural path to take for expanding our analysis is to remove the planar restriction, giving the tissue the possibility of going into buckling instabilities as a way of releasing stresses.

We considered localized continuous activity in a single cell of a tissue, as seen in several experiment in which apical constrictions occur, and described the local response using geometrical observables that are feasible of measuring in some experiments. If the medial region is active, then the active cell takes an anisotropic shape; if the perimeter is active then the active cell tends to get an isotropic shape. In literature there is also a pulsatile model to describe the mechanism of apical constrictions, that we did not consider. A detailed study using that dynamic is not present in literature. We applied the analysis of the geometrical response to study the active contraction pulses observed in the epithelial tissue of the annual killifish *Austrolebias nigripinnis* during the blastula stage. We were able to discriminate between different models of apical constrictions and also obtained the best fit of all parameters of the vertex model, globals, and specific for each active event. This serves as a motivation for new experiments, with the focus on relating the parameters of our model to biophysical processes of cells and tissues. These methods can be applied to other biological systems as well. These results are published in the article "Modelling of active contraction pulses in epithelial cells using the vertex model", Ref. [60], and are also part of the new version "Geometrical characterisation of active contraction pulses in epithelial cells using the vertex model" (not submitted yet). In some experiments involving epithelial tissues, interfaces between cells are considerably curved. We expect our model can be expanded to study cellular

activity in those systems.

We studied the cases of medial and perimeter activity in an active Gaussian region of the tissue by performing numerical simulations using the vertex model, using ordered and low disordered tissues. We calculated quantities related to contraction and displacement, in the steady state, and showed and excellent agreement with a continuum description that assumes small cellular ellipticity. Besides, we compared the temporal evolution of the same observables for ordered tissues and obtained an excellent agreement when rescaling the time scales. In the case of perimeter activity, a small change (5%) in the activity parameter between both description is needed to obtain a better fit. Current results of simulations using low-disordered and highly-disordered tissues are encouraging. To prepare a manuscript about these findings, we are now testing our results in other active regions (not Gaussian).

With the aim to analyze the self-organization on fluctuating non-polarized active tissues, we performed numerical simulations variating the target parameters of the vertex model, mimicking the continuum reconstruction of the cytoskeleton. Using statistical methods, we showed a scale separation between the micro and macro-scale of the model. We found compression waves in the long-wavelength regime and an inverse energy cascade. We expect this information will be useful to construct a continuum model of fluctuating tissues. An intensive analysis in other regions of the space of parameters in search of other collective motion is needed.

In brief, this particular example of active matter evolves due to interaction between units (cells), and since the system is confluent (there is no empty space between cells), geometry appears as an important tool to characterize it, which is what we did in this theses. Importantly, cellular geometry is easily accessible in several experiments, and therefore we expect some of the results of this theses will be tested in the future.

Bibliography

[1] Tamás Vicsek and Anna Zafeiris. Collective motion. *Physics reports*, 517(3-4):71–140, 2012.

[2] M Cristina Marchetti, Jean-François Joanny, Sriram Ramaswamy, Tanniemola B Liverpool, Jacques Prost, Madan Rao, and R Aditi Simha. Hydrodynamics of soft active matter. *Reviews of Modern Physics*, 85(3):1143, 2013.

[3] Sriram Ramaswamy. Active matter. *Journal of Statistical Mechanics: Theory and Experiment*, 2017(5):054002, 2017.

[4] Étienne Fodor and M Cristina Marchetti. The statistical physics of active matter: From self-catalytic colloids to living cells. *Physica A: Statistical Mechanics and its Applications*, 504:106–120, 2018.

[5] Gerhard Gompper, Roland G Winkler, Thomas Speck, Alexandre Solon, Cesare Nardini, Fernando Peruani, Hartmut Löwen, Ramin Golestanian, U Benjamin Kaupp, Luis Alvarez, et al. The 2020 motile active matter roadmap. *Journal of Physics: Condensed Matter*, 32:193001, 2020.

[6] Shuji Ishihara, Philippe Marcq, and Kaoru Sugimura. From cells to tissue: A continuum model of epithelial mechanics. *Physical Review E*, 96(2):022418, 2017.

[7] Maria Luisa Cordero Rodrigo Soto and Felipe Barra. Millennium nucleus physics of active matter.

[8] Arnab Saha, Masatoshi Nishikawa, Martin Behrndt, Carl-Philipp Heisenberg, Frank Jülicher, and Stephan W Grill. Determining physical properties of the cell cortex. *Biophysical journal*, 110(6):1421–1429, 2016.

[9] Nargess Khalilgharibi, Jonathan Fouchard, Nina Asadipour, Ricardo Barrientos, Maria Duda, Alessandra Bonfanti, Amina Yonis, Andrew Harris, Payman Mosaffa, Yasuyuki Fujita, et al. Stress relaxation in epithelial monolayers is controlled by the actomyosin cortex. *Nature Physics*, 15(8):838–847, 2019.

[10] Tim Hohmann and Faramarz Dehghani. The cytoskeleton—a complex interacting meshwork. *Cells*, 18(4):362, 2019.

[11] Guillaume Salbreux, Guillaume Charras, and Ewa Paluch. Actin cortex mechanics and

cellular morphogenesis. *Trends in cell biology*, 22(10):536–545, 2012.

[12] Tomas Ganz. Epithelia: not just physical barriers. *Proceedings of the National Academy of Sciences*, 99(6):3357–3358, 2002.

[13] Jamie Davies. *Mechanisms of Morphogenesis*. Elsevier Academic Press, 1st edition edition, 2005.

[14] Adam C Martin. Pulsation and stabilization: contractile forces that underlie morphogenesis. *Developmental biology*, 341(1):114–125, 2010.

[15] Universidad de Chile. Laboratory of experimental ontogeny.

[16] Universidad de Chile. Laboratory of scientific image analysis.

[17] Germán Reig, Mauricio Cerda, Néstor Sepúlveda, Daniela Flores, Victor Castañeda, Masazumi Tada, Steffen Härtel, and Miguel L Concha. Extra-embryonic tissue spreading directs early embryo morphogenesis in killifish. *Nature communications*, 8(1):1–14, 2017.

[18] Julia Riedl, Alvaro H Crevenna, Kai Kessenbrock, Jerry Haochen Yu, Dorothee Neukirchen, Michal Bista, Frank Bradke, Dieter Jenne, Tad A Holak, Zena Werb, et al. Lifeact: a versatile marker to visualize f-actin. *Nature methods*, 5(7):605–607, 2008.

[19] Lilianna Solnica-Krezel. Conserved patterns of cell movements during vertebrate gastrulation. *Current biology*, 15(6):R213–R228, 2005.

[20] Sophie Quintin, Christelle Gally, and Michel Labouesse. Epithelial morphogenesis in embryos: asymmetries, motors and brakes. *Trends in genetics*, 24(5):221–230, 2008.

[21] Adam C Martin. The physical mechanisms of drosophila gastrulation: Mesoderm and endoderm invagination. *Genetics*, 214(3):543–560, 2020.

[22] Li He, Xiaobo Wang, Ho Lam Tang, and Denise J Montell. Tissue elongation requires oscillating contractions of a basal actomyosin network. *Nature cell biology*, 12(12):1133–1142, 2010.

[23] Neophytos Christodoulou and Paris A Skourides. Cell-autonomous ca2+ flashes elicit pulsed contractions of an apical actin network to drive apical constriction during neural tube closure. *Cell reports*, 13(10):2189–2202, 2015.

[24] Barry M Gumbiner. Cell adhesion: the molecular basis of tissue architecture and morphogenesis. *Cell*, 84(3):345–357, 1996.

[25] Masatoshi Takeichi. Dynamic contacts: rearranging adherens junctions to drive epithelial remodelling. *Nature reviews Molecular cell biology*, 15(6):397–410, 2014.

[26] Adam C Martin and Bob Goldstein. Apical constriction: themes and variations on a cellular mechanism driving morphogenesis. *Development*, 141(10):1987–1998, 2014.

[27] Nicole Gorfinkiel. From actomyosin oscillations to tissue-level deformations. *Develop-*

mental Dynamics, 245(3):268–275, 2016.

[28] Hui Miao and J Todd Blankenship. The pulse of morphogenesis: actomyosin dynamics and regulation in epithelia. *Development*, 147:17, 2020.

[29] Ann Sutherland and Alyssa Lesko. Pulsed actomyosin contractions in morphogenesis. *F1000Research*, 9, 2020.

[30] John Metzcar, Yafei Wang, Randy Heiland, and Paul Macklin. A review of cell-based computational modeling in cancer biology. *JCO clinical cancer informatics*, pages 1–13, 2019.

[31] Da Weaire and N Rivier. Soap, cells and statistics—random patterns in two dimensions. *Contemporary Physics*, 25(1):59, 1984.

[32] Tohru Okuzono and Kyozi Kawasaki. Intermittent flow behavior of random foams: a computer experiment on foam rheology. *Physical Review E*, 51(2):1246, 1995.

[33] Reza Farhadifar, Jens-Christian Röper, Benoit Aigouy, Suzanne Eaton, and Frank Jülicher. The influence of cell mechanics, cell-cell interactions, and proliferation on epithelial packing. *Current Biology*, 17(24):2095, 2007.

[34] Philipp Spahn and Rolf Reuter. A vertex model of drosophila ventral furrow formation. *PLoS One*, 8(9):e75051, 2013.

[35] Yasuhiro Inoue, Makoto Suzuki, Tadashi Watanabe, Naoko Yasue, Itsuki Tateo, Taiji Adachi, and Naoto Ueno. Mechanical roles of apical constriction, cell elongation, and cell migration during neural tube formation in xenopus. *Biomechanics and modeling in mechanobiology*, 15(6):1733, 2016.

[36] Dapeng Bi, JH Lopez, Jennifer M Schwarz, and M Lisa Manning. A density-independent rigidity transition in biological tissues. *Nature Physics*, 11(12):1074, 2015.

[37] Hisao Honda, Masaharu Tanemura, and Tatsuzo Nagai. A three-dimensional vertex dynamics cell model of space-filling polyhedra simulating cell behavior in a cell aggregate. *Journal of theoretical biology*, 226(4):439–453, 2004.

[38] Edouard Hannezo, Jacques Prost, and Jean-Francois Joanny. Theory of epithelial sheet morphology in three dimensions. *Proceedings of the National Academy of Sciences*, 111(1):27–32, 2014.

[39] Satoru Okuda, Katsuyuki Unoki, Mototsugu Eiraku, and Ken-ichi Tsubota. Contractile actin belt and mesh structures provide the opposite dependence of epithelial stiffness on the spontaneous curvature of constituent cells. *Development, growth & differentiation*, 59(5):455–464, 2017.

[40] Satoru Okuda, Erina Kuranaga, and Katsuhiko Sato. Apical junctional fluctuations lead to cell flow while maintaining epithelial integrity. *Biophysical journal*, 116(6):1159–1170, 2019.

[41] Alexander G Fletcher, Miriam Osterfield, Ruth E Baker, and Stanislav Y Shvartsman. Vertex models of epithelial morphogenesis. *Biophysical journal*, 106(11):2291, 2014.

[42] C Yu Jessica and Rodrigo Fernandez-Gonzalez. Quantitative modelling of epithelial morphogenesis: integrating cell mechanics and molecular dynamics. In *Seminars in cell & developmental biology*, volume 67, page 153. Elsevier, 2017.

[43] Douglas B Staple, Reza Farhadifar, J-C Röper, Benoit Aigouy, Suzanne Eaton, and Frank Jülicher. Mechanics and remodelling of cell packings in epithelia. *The European Physical Journal E*, 33(2):117, 2010.

[44] Alexander Nestor-Bergmann, Emma Johns, Sarah Woolner, and Oliver E Jensen. Mechanical characterization of disordered and anisotropic cellular monolayers. *Physical Review E*, 97(5):052409, 2018.

[45] Hisao Honda. Description of cellular patterns by dirichlet domains: the two-dimensional case. *Journal of theoretical biology*, 72(3):523–543, 1978.

[46] Sara Kaliman, Christina Jayachandran, Florian Rehfeldt, and Ana-Sunčana Smith. Limits of applicability of the voronoi tessellation determined by centers of cell nuclei to epithelium morphology. *Frontiers in physiology*, 7:551, 2016.

[47] Nebojsa Murisic, Vincent Hakim, Ioannis G Kevrekidis, Stanislav Y Shvartsman, and Basile Audoly. From discrete to continuum models of three-dimensional deformations in epithelial sheets. *Biophysical journal*, 109(1):154–163, 2015.

[48] Yukitaka Ishimoto and Yoshihiro Morishita. Bubbly vertex dynamics: a dynamical and geometrical model for epithelial tissues with curved cell shapes. *Physical Review E*, 90(5):052711, 2014.

[49] François Graner and James A Glazier. Simulation of biological cell sorting using a two-dimensional extended potts model. *Physical review letters*, 69(13):2013, 1992.

[50] Adrian R. Noppe, Anthony P Roberts, Alpha S Yap, Guillermo A Gomez, and Zoltan Neufeld. Modelling wound closure in an epithelial cell sheet using the cellular potts model. *Integrative Biology*, 7(10):1253–1264, 2015.

[51] Marco Scianna, Luigi Preziosi, and Katarina Wolf. A cellular potts model simulating cell migration on and in matrix environments. *Mathematical Biosciences & Engineering*, 10(1):235, 2013.

[52] James A Glazier and François Graner. Simulation of the differential adhesion driven rearrangement of biological cells. *Physical Review E*, 47(3):2128, 1993.

[53] Soma Sanyal and James A Glazier. Viscous instabilities in flowing foams: A cellular potts model approach. *Journal of Statistical Mechanics: Theory and Experiment*, 2006(10):P10008, 2006.

[54] Dapeng Bi, Xingbo Yang, M Cristina Marchetti, and M Lisa Manning. Motility-driven

glass and jamming transitions in biological tissues. *Physical Review X*, 6(2):021011, 2016.

[55] Daniel M Sussman and Matthias Merkel. No unjamming transition in a voronoi model of biological tissue. *Soft matter*, 14(17):3397–3403, 2018.

[56] Daniel L Barton, Silke Henkes, Cornelis J Weijer, and Rastko Sknepnek. Active vertex model for cell-resolution description of epithelial tissue mechanics. *PLoS computational biology*, 13(6):e1005569, 2017.

[57] Jacques Prost, Frank Jülicher, and Jean-François Joanny. Active gel physics. *Nature physics*, 11(2):111–117, 2015.

[58] Michael Czajkowski, Dapeng Bi, M Lisa Manning, and M Cristina Marchetti. Hydrodynamics of shape-driven rigidity transitions in motile tissues. *Soft Matter*, 14(27):5628–5642, 2018.

[59] Fernanda Pérez-Verdugo, Jean-Francois Joanny, and Rodrigo Soto. Vertex model instabilities for tissues subject to cellular activity or applied stresses. *Physical Review E*, 102(5):052604, 2020.

[60] Fernanda Pérez-Verdugo, Germán Reig, Mauricio Cerda, Miguel L Concha, and Rodrigo Soto. Modelling of active contraction pulses in epithelial cells using the vertex model. *arXiv preprint arXiv:2106.00824*, 2021.

[61] Jennifer A Zallen and Richard Zallen. Cell-pattern disordering during convergent extension in drosophila. *Journal of Physics: Condensed Matter*, 16(44):S5073, 2004.

[62] Andrew R Harris, Loic Peter, Julien Bellis, Buzz Baum, Alexandre J Kabla, and Guillaume T Charras. Characterizing the mechanics of cultured cell monolayers. *Proceedings of the National Academy of Sciences*, 109(41):16449–16454, 2012.

[63] Aziza Merzouki, Orestis Malaspinas, and Bastien Chopard. The mechanical properties of a cell-based numerical model of epithelium. *Soft Matter*, 12(21):4745–4754, 2016.

[64] L. D. Landay and E. M. Lifshitz. *Theory of Elasticity*. Pergamon Press, second revised and enlarged edition edition, 1970.

[65] Matteo Rauzi, Pascale Verant, Thomas Lecuit, and Pierre-François Lenne. Nature and anisotropy of cortical forces orienting drosophila tissue morphogenesis. *Nature cell biology*, 10(12):1401, 2008.

[66] Yanlan Mao, Alexander L Tournier, Paul A Bates, Jonathan E Gale, Nicolas Tapon, and Barry J Thompson. Planar polarization of the atypical myosin dachs orients cell divisions in drosophila. *Genes & development*, 25(2):131, 2011.

[67] Maria Leptin and Barbara Grunewald. Cell shape changes during gastrulation in drosophila. *Development*, 110(1):73, 1990.

[68] Raphaël Etournay, Marko Popović, Matthias Merkel, Amitabha Nandi, Corinna Blasse, Benoît Aigouy, Holger Brandl, Gene Myers, Guillaume Salbreux, Frank Jülicher, et al. Interplay of cell dynamics and epithelial tension during morphogenesis of the drosophila pupal wing. *Elife*, 4:e07090, 2015.

[69] Teruyoshi Koshihara, Kenichi Matsuzaka, Toru Sato, and Takashi Inoue. Effect of stretching force on the cells of epithelial rests of malassez in vitro. *International Journal of Dentistry*, 2010.

[70] Bo Li, Yan-Ping Cao, Xi-Qiao Feng, and Huajian Gao. Mechanics of morphological instabilities and surface wrinkling in soft materials: a review. *Soft Matter*, 8(21):5728–5745, 2012.

[71] Celeste M Nelson. On buckling morphogenesis. *Journal of biomechanical engineering*, 138(2), 2016.

[72] Adam C Martin, Matthias Kaschube, and Eric F Wieschaus. Pulsed contractions of an actin–myosin network drive apical constriction. *Nature*, 457(7228):495–499, 2009.

[73] Frank M Mason, Shicong Xie, Claudia G Vasquez, Michael Tworoger, and Adam C Martin. Rhoa gtpase inhibition organizes contraction during epithelial morphogenesis. *Journal of Cell Biology*, 214(5):603–617, 2016.

[74] Jonathan B Michaux, François B Robin, William M McFadden, and Edwin M Munro. Excitable rhoa dynamics drive pulsed contractions in the early c. elegans embryo. *Journal of Cell Biology*, 217(12):4230–4252, 2018.

[75] F Backouche, L Haviv, D Groswasser, and A Bernheim-Groswasser. Active gels: dynamics of patterning and self-organization. *Physical biology*, 3(4):264, 2006.

[76] Jean-François Joanny and Jacques Prost. Active gels as a description of the actin-myosin cytoskeleton. *HFSP journal*, 3(2):94–104, 2009.

[77] Xingbo Yang, Dapeng Bi, Michael Czajkowski, Matthias Merkel, M Lisa Manning, and M Cristina Marchetti. Correlating cell shape and cellular stress in motile confluent tissues. *Proceedings of the National Academy of Sciences*, 114(48):12663–12668, 2017.

[78] Rodrigo Soto. *Kinetic theory and transport phenomena*, volume 25. Oxford University Press, 2016.

Appendix A

Vertex model: Equations of motion

The energy functional of the vertex model is given by

$$E = \sum_c \frac{K_A}{2} \left(A_c - A_{0c}\right)^2 + \frac{K_P}{2} \sum_c \left(P_c - P_{0c}\right)^2 + J \sum_{\langle \mathrm{i},j \rangle} l_{\mathrm{i}j}, \tag{A.1}$$

and the equations of motion for each vertex position $\mathbf{r}_\mathrm{i}$ are

$$\frac{\mathrm{d}\mathbf{r}_\mathrm{i}}{\mathrm{d}t} = -\gamma \frac{\partial E}{\partial \mathbf{r}_\mathrm{i}}. \tag{A.2}$$

We can write

$$\frac{\mathrm{d}\mathbf{r}_\mathrm{i}}{\mathrm{d}t} = \frac{\mathrm{d}\mathbf{r}_\mathrm{i}}{\mathrm{d}t}^{(A)} + \frac{\mathrm{d}\mathbf{r}_\mathrm{i}}{\mathrm{d}t}^{(P)} + \frac{\mathrm{d}\mathbf{r}_\mathrm{i}}{\mathrm{d}t}^{(J)}, \tag{A.3}$$

where each term is the one proportional to K_A, K_P and J, respectively.

Assuming a polygon of N vertices, we calculate its area using the triangularization method

with respect to the vertex v_1.

$$\begin{aligned} A_c &= -\sum_{j=2}^{N-1} \frac{1}{2}\hat{\mathbf{z}} \cdot (\mathbf{r}_{j,1} \times \mathbf{r}_{j+1,1}) , \\ &= -\sum_{j=2}^{N-1} \frac{1}{2}\hat{\mathbf{z}} \cdot [(\mathbf{r}_j - \mathbf{r}_1) \times (\mathbf{r}_{j+1} - \mathbf{r}_1)] , \\ &= \sum_{j=2}^{N-1} \frac{1}{2}\hat{\mathbf{z}} \cdot [-\mathbf{r}_j \times \mathbf{r}_{j+1} + \mathbf{r}_1 \times (\mathbf{r}_{j+1} - \mathbf{r}_j)] , \\ &= \sum_{j=2}^{N-1} \frac{1}{2}\hat{\mathbf{z}} \cdot [-\mathbf{r}_j \times \mathbf{r}_{j+1}] + \frac{1}{2}\hat{\mathbf{z}} \cdot [\mathbf{r}_1 \times (\mathbf{r}_N - \mathbf{r}_2)] , \end{aligned} \tag{A.4}$$

where we used that the tissue is in the x-y plane, with the vertices in each cell ordered clockwise, and we defined $\mathbf{r}_{\mathrm{i},j} = \mathbf{r}_\mathrm{i} - \mathbf{r}_j$ and $r_{\mathrm{i},j} = |\mathbf{r}_{\mathrm{i},j}|$. To compute the energy gradients, it is convenient to use this expression considering any vertex as the chosen one to make the triangularization, i.e., we replace $\mathbf{r}_1 \to \mathbf{r}_\mathrm{i}$, $\mathbf{r}_2 \to \mathbf{r}_{\mathrm{i}+1}$ and $\mathbf{r}_N \to \mathbf{r}_{\mathrm{i}-1}$ (cyclic vertex numbering is used, i.e. $N+1 \equiv 1$ and $-1 \equiv N$),

$$A_c = \sum_{j\neq \mathrm{i}}^{N-1} \frac{1}{2}\hat{\mathbf{z}} \cdot [-\mathbf{r}_j \times \mathbf{r}_{j+1}] + \frac{1}{2}\hat{\mathbf{z}} \cdot [\mathbf{r}_\mathrm{i} \times (\mathbf{r}_{\mathrm{i}-1} - \mathbf{r}_{\mathrm{i}+1})] . \tag{A.5}$$

Then,

$$\nabla_\mathrm{i} A_c = \frac{1}{2}\nabla_\mathrm{i} \left(\hat{\mathbf{z}} \cdot [\mathbf{r}_\mathrm{i} \times (\mathbf{r}_{\mathrm{i}-1} - \mathbf{r}_{\mathrm{i}+1})]\right) = \frac{1}{2}\nabla_\mathrm{i} \left[x_\mathrm{i} (y_{\mathrm{i}-1} - y_{\mathrm{i}+1}) - y_\mathrm{i} (x_{\mathrm{i}-1} - x_{\mathrm{i}+1})\right] , \tag{A.6}$$

$$= \frac{1}{2} (y_{\mathrm{i}-1} - y_{\mathrm{i}+1})\, \hat{\mathbf{x}} - \frac{1}{2} (x_{\mathrm{i}-1} - x_{\mathrm{i}+1})\, \hat{\mathbf{y}} = \frac{1}{2}\mathbf{r}_{\mathrm{i}-1,\mathrm{i}+1} \times \hat{\mathbf{z}}. \tag{A.7}$$

Also, the perimeter and its gradient with respect to the position of the vertex i of the same polygon are given by

$$P_c = \sum_{j=1}^{N} |\mathbf{r}_{j+1,j}|, \tag{A.8}$$

$$\begin{aligned} \nabla_\mathrm{i} P_c &= \nabla_\mathrm{i} \left(|\mathbf{r}_{\mathrm{i}+1,\mathrm{i}}| + |\mathbf{r}_{\mathrm{i}-1,\mathrm{i}}|\right) , \\ &= -\frac{\mathbf{r}_{\mathrm{i}+1,\mathrm{i}}}{r_{\mathrm{i}+1,\mathrm{i}}} - \frac{\mathbf{r}_{\mathrm{i}-1,\mathrm{i}}}{r_{\mathrm{i}-1,\mathrm{i}}}. \end{aligned} \tag{A.9}$$

Finally, the length in the third term and its gradient are

$$l_{\mathrm{i}j} = |\mathbf{r}_{j,\mathrm{i}}|, \tag{A.10}$$

$$\nabla_\mathrm{i} l_{ij} = \nabla_\mathrm{i} |\mathbf{r}_{j,\mathrm{i}}|, \tag{A.11}$$

$$= -\frac{\mathbf{r}_{j,\mathrm{i}}}{r_{j,\mathrm{i}}}. \tag{A.12}$$

Then, the different terms in Eq. (A.3) are

$$\begin{aligned}
\frac{\mathrm{d}\mathbf{r}_{\mathrm{i}}}{\mathrm{d}t}^{(A)} &= -\sum_{c} K_A \left(A_c - A_{0c}\right) \nabla_{\mathrm{i}} A_c, \\
&= -\sum_{c} K_A \left(A_c - A_{0c}\right) \frac{1}{2} \left(\mathbf{r}_{\mathrm{i}_c-1,\mathrm{i}_c+1} \times \hat{\mathbf{z}}\right), \\
&= \sum_{c} K_A \left(A_c - A_{c0}\right) \frac{1}{2} \left(\mathbf{r}_{\mathrm{i}_c+1,\mathrm{i}_c-1} \times \hat{\mathbf{z}}\right), \qquad \text{(A.13)} \\
\frac{\mathrm{d}\mathbf{r}_{\mathrm{i}}}{\mathrm{d}t}^{(P)} &= -\sum_{c} K_P \left(P_c - P_{0c}\right) \nabla_{\mathrm{i}} P_c, \\
&= \sum_{c} K_P \left(P_c - P_{0c}\right) \left(\frac{\mathbf{r}_{\mathrm{i}_c+1,\mathrm{i}}}{r_{\mathrm{i}_c+1,\mathrm{i}}} + \frac{\mathbf{r}_{\mathrm{i}_c-1,\mathrm{i}}}{r_{\mathrm{i}_c-1,\mathrm{i}}}\right), \qquad \text{(A.14)} \\
\frac{\mathrm{d}\mathbf{r}_{\mathrm{i}}}{\mathrm{d}t}^{(J)} &= -\sum_{\langle \mathrm{i},j \rangle} J \nabla_{\mathrm{i}} l_{\mathrm{i}j}, \\
&= \sum_{\langle \mathrm{i},j \rangle} J \frac{\mathbf{r}_{j,\mathrm{i}}}{r_{j,\mathrm{i}}}, \qquad \text{(A.15)}
\end{aligned}$$

where Eqs. (A.13) and (A.14) consider a sum over the cells to which the vertex i belongs to, and $\mathrm{i}_c + 1$ and $\mathrm{i}_c - 1$ refer to the next and previous vertex to i, in clockwise counting, belonging to cell c. Also, (A.15) considers a sum over the vertices j that are adjacent to the vertex i.

It is important to note that when we assume that the system obeys periodic boundary conditions, the term given by (A.15) can also be written as a sum over the cells at which the vertex i belongs to,

$$\begin{aligned}
\frac{\mathrm{d}\mathbf{r}_{\mathrm{i}}}{\mathrm{d}t}^{(J)} &= -\sum_{c} \frac{J}{2} \nabla_{\mathrm{i}} P_c, \\
&= \sum_{c} \frac{J}{2} \left(\frac{\mathbf{r}_{\mathrm{i}_c+1,\mathrm{i}}}{r_{\mathrm{i}_c+1,\mathrm{i}}} + \frac{\mathbf{r}_{\mathrm{i}_c-1,\mathrm{i}}}{r_{\mathrm{i}_c-1,\mathrm{i}}}\right). \qquad \text{(A.16)}
\end{aligned}$$

If the tissue is made of hexagonal cells, then each sum described above is over three cells. For the case of square cells is over fours cells.

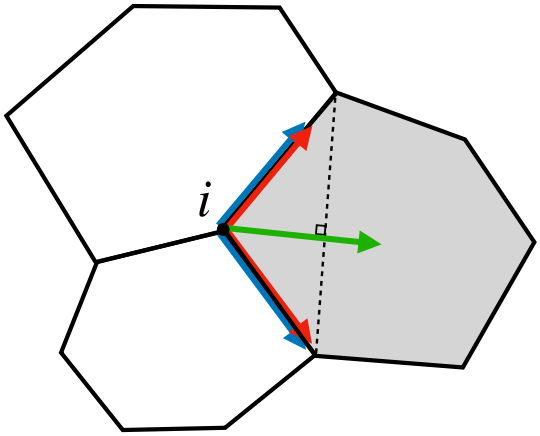

Figure A.1: Direction of the forces over the vertex i due to changes in the area and perimeter of the shaded cell, in green and blue arrows, respectively. In red are the directions of the force due to changes in the length of the shared borders of the shaded cell with the unshaded ones.

Appendix B

Models of viscoelasticity

During this thesis, two different models of viscoelasticity for the target parameters of the vertex model are used: the Maxwell model and the Kelvin model. This means that A_{0c} and P_{0c} have properties of elasticity (at short times) and viscosity (at longer times). The representation of both models can be seen in Fig. B.1. The Maxwell (Kelvin) model is represented by a viscous dashpot defined by a damping coefficient γ connected in series (in parallel) with an elastic spring defined by an elastic constant k and a natural length l_0. In the case of the Maxwell model we will use that $l_0 = 0$. In the next, we will write the equations for A_{0c}, but analogous equations are valid for P_{0c}.

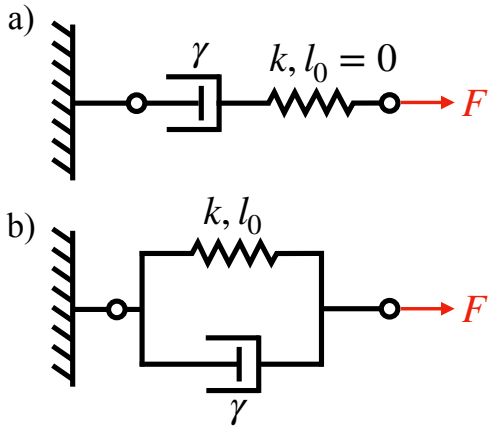

Figure B.1: Diagrams two models of viscoelasticity: a) Maxwell model, and b) Kelvin model. The dashpot are defined by a damping coefficient γ, and the elastic springs by an elastic constant k and a natural length l_0. In a) we consider $l_0 = 0$. In both cases, the system is attached in the left end, and a force F is acting in the right end.

B.0.1 Maxwell model

At the moment of applying the force F in the right end of the system in Fig. B.1-a), the spring will elongate fast. Instead, the elongation of the dashpot will be slowly. We will call x the position of a particular point q between the dashpot and the spring, and y to the position where F is applied. The initial elongation of the spring will induce a force that

will compensate F, given by $F_1 = -k(y-x)$. Over q there will be acting the elastic force $F_2 = k(y-x)$ to the right, and a viscous force $F_3 = -\gamma\dot{x}$ to the left. With these forces, and considering that the inertial effects are neglected, we obtain

$$\begin{aligned} \gamma\dot{x} =& k(y-x), \\ \dot{x} =& -\frac{k}{\gamma}(y-x). \end{aligned} \tag{B.1}$$

Performing the following changes $x \to A_{0c}, y \to A_c$ and $k/\gamma \to \nu_A$, we obtain

$$\frac{\mathrm{d}A_{0c}}{\mathrm{d}t} = -\nu_A \left(A_{0c} - A_c\right), \tag{B.2}$$

which is the model of plasticity described in Ch. 2.

If the force F is maintained over time, the system is plastically deformed.

B.0.2 Kelvin model

At the moment of applying the force F in the right end of the system in Fig. B.1-b), the elastic spring and the viscous dashpot elongate the same. Calling x to the elongation, the forces done by the spring and the dashpot during the elongation are given by $F_1 = -k(x-l_0)$ and $F_2 = -\gamma\dot{x}$, respectively. Considering that the inertial effects are neglected, we obtain

$$\begin{aligned} 0 =& -\gamma\dot{x} - k(x-l_0) + F, \\ \dot{x} =& -\frac{k}{\gamma}(x-l_0) + \frac{F}{\gamma}. \end{aligned} \tag{B.3}$$

Performing the following changes $x \to A_{0c}, l_0 \to A_{00c}, k/\gamma \to \nu_A$, and $F/\gamma \to \widetilde{F}$, we obtain

$$\frac{\mathrm{d}A_{0c}}{\mathrm{d}t} = -\nu_A \left(A_{0c} - A_{00c}\right) + \widetilde{F}, \tag{B.4}$$

which is the model of memory described in Ch. 2, with $\widetilde{F}$ mimicking the effects of the temporal activity function $f_{A_c}(t)$ or the cellular fluctuations.

If we consider that while the system is elongated, F suddenly stops acting on the system, which would be the case in a non-fluctuating system were the temporal activity functions are already finished, then two forces act on the right end: $F_1 = -k(x-l_0)$ and $F_2 = -\gamma\dot{x}$. Then, the temporal evolution of x is given by

$$\begin{aligned} \dot{x} =& -\frac{k}{\gamma}(x-l_0), \\ x(t) =& l_0 + A\mathrm{e}^{-(k/\gamma)t}, \end{aligned} \tag{B.5}$$

from where we see that if $t \to \infty$, then $x(t) \to l_0$.

Appendix C

Energy expressions for fluctuation tissues

For the analytic calculations, we consider a regular tissue composed of N identical regular hexagonal cells of side a, for which the target cell area and perimeter for all cells are $A_{0c} = 3\sqrt{3}a^2/2$ and $P_{0c} = 6a$, respectively.

C.1 Tissue under cell activity

Cell activity is included as homogeneous modifications of the equilibrium perimeters, $P_{0c} \to (1 + \lambda_P) P_{0c}$ and equilibrium areas $A_{0c} \to (1 + \lambda_A) A_{0c}$, with $\lambda_P, \lambda_A > 0$ for expansions and $\lambda_P, \lambda_A < 0$ for contractions.

We define $A_c^{(1)}$ as the area of the cell c with fluctuations characterized by the matrix U,

$$A_c^{(1)} = \left(1 + \varepsilon \mathrm{tr}\,(U) + \varepsilon^2 \det(U)\right) A_{0c}. \tag{C.1}$$

Then, when considering an activity modulated by λ_A, the term of the energy proportional to K_A is given by

$$\begin{aligned} E_A &= \sum_c \frac{K_A}{2} \left[A_c^{(1)} - (1 + \lambda_A) A_{0c}\right]^2, \\ &= \sum_c \frac{K_A}{2} A_{0c}^2 \left[-\lambda_A + \varepsilon \mathrm{tr}\,(U) + \varepsilon^2 \det(U)\right]^2. \end{aligned} \tag{C.2}$$

Hence, the zeroth, first, and second order terms of E_A are

$$E_A^{(0)} = \sum_c \frac{K_A}{2} A_{0c}^2 \lambda_A^2, \tag{C.3}$$

$$E_A^{(1)} = -\sum_c K_A A_{0c}^2 \mathrm{tr}\,(U)\, \lambda_A, \tag{C.4}$$

$$E_A^{(2)} = \sum_c \frac{K_A}{2} A_{0c}^2 \left[\mathrm{tr}\,(U)^2 - 2\det(U)\, \lambda_A\right]. \tag{C.5}$$

We define $P_c^{(1)}$ as the perimeter of the cell c with fluctuations characterized by the matrix U,

$$P_c^{(1)} = \left[1 + \frac{1}{2}\varepsilon \mathrm{tr}\left(U\right) + \frac{1}{8}\varepsilon^2 \mathrm{det}\left(U\right) + \frac{3}{16}\varepsilon^2 \mathrm{tr}\left(U^T U\right) - \frac{1}{8}\varepsilon^2 \mathrm{tr}\left(U\right)^2\right] P_{0c}. \tag{C.6}$$

Then, when considering an activity modulated by λ_P, the term of the energy proportional to K_P is given by

$$\begin{aligned} E_P =& \sum_c \frac{K_P}{2}\left[P_c^{(1)} - \left(1+\lambda_P\right) P_{0c}\right]^2, \\ =& \sum_c \frac{K_P}{2} P_{0c}^2 \left[-\lambda_P + \frac{1}{2}\varepsilon \mathrm{tr}\left(U\right) + \frac{1}{8}\varepsilon^2 \mathrm{det}\left(U\right) + \frac{3}{16}\varepsilon^2 \mathrm{tr}\left(U^T U\right) - \frac{1}{8}\varepsilon^2 \mathrm{tr}\left(U\right)^2\right]^2. \end{aligned} \tag{C.7}$$

The zeroth, first, and second order terms of E_P are therefore given by

$$E_P^{(0)} = \sum_c \frac{K_P}{2} P_{0c}^2 \lambda_P^2, \tag{C.8}$$

$$E_P^{(1)} = -\sum_c \frac{K_P}{2} P_{0c}^2 \mathrm{tr}\left(U\right) \lambda_P, \tag{C.9}$$

$$E_P^{(2)} = \sum_c \frac{K_P}{8} P_{0c}^2 \left[\left(1+\lambda_P\right) \mathrm{tr}\left(U\right)^2 - \lambda_P \mathrm{det}\left(U\right) - \frac{3}{2}\lambda_P \mathrm{tr}\left(U^T U\right)\right]. \tag{C.10}$$

Finally, the adhesion contribution to the energy is

$$E_J = \sum_c \frac{J}{2} P_c^{(1)}, \tag{C.11}$$

where $P_c^{(1)}$ is given in Eq. (C.6). As a result, the zeroth, first, and second order terms of E_J are given by

$$E_J^{(0)} = \sum_c \frac{J}{4} P_{0c}, \tag{C.12}$$

$$E_J^{(1)} = \sum_c \frac{J}{4} P_{0c} \mathrm{tr}\left(U\right), \tag{C.13}$$

$$E_J^{(2)} = \sum_c \frac{J}{16} P_{0c} \left[\mathrm{det}\left(U\right) + \frac{3}{2}\mathrm{tr}\left(U^T U\right) - \mathrm{tr}\left(U\right)^2\right]. \tag{C.14}$$

Eqs. (C.1) and (C.6) can be obtained using Mathematica.

C.2 Tissue under stress

Now, we study the same energy contributions, but when the tissue is subject to a homogeneous strain, such that all the vertices change their position as $\mathbf{r}_\mathrm{i}^{[0]} \to \Lambda \mathbf{r}_\mathrm{i}^{[0]}$, where Λ is a 2×2 matrix that gives account of the pre-deformation.

In a similar way as in the previous section we can define $A_c^{(1)}$ and $P_c^{(1)}$, representing the area and perimeter of the cell c, that was initially a regular hexagon with area A_{0c} and perimeter P_{0c}, which is now subject to a given strain characterized by the matrix Λ. Then, we define $A_c^{(2)}$ and $P_c^{(2)}$ as the values when we allow fluctuations, modulated by the matrix U, in the system.

$$A_c^{(1)} = \det(\Lambda)\, A_{0c}, \tag{C.15}$$

$$A_c^{(2)} = \left[1 + \varepsilon \mathrm{tr}(U) + \varepsilon^2 \det(U)\right] A_c^{(1)}. \tag{C.16}$$

The expressions for $P_c^{(1)}$ and $P_c^{(2)}$ are more complicated to write in terms of the matrices Λ and U. In general terms, considering that the six vertices of the hexagon have positions $\mathbf{r}_\mathrm{i}$, we obtain:

$$P_c^{(1)} = \sum_{\mathrm{i}=1}^{6} P_{c_\mathrm{i}}^{(1)}, \tag{C.17}$$

$$P_{c_\mathrm{i}}^{(1)} = \sqrt{\alpha_\mathrm{i}^2 + \beta_\mathrm{i}^2}, \tag{C.18}$$

$$P_c^{(2)} = P_c^{(1)} + \varepsilon M_c^{(1)} + \varepsilon^2 M_c^{(2)}, \tag{C.19}$$

with

$$\alpha_\mathrm{i} = \lambda_{xx} {x_{\mathrm{i}+1,\mathrm{i}}}^{(0)} + \lambda_{xy} {y_{\mathrm{i}+1,\mathrm{i}}}^{(0)}, \tag{C.20}$$

$$\beta_\mathrm{i} = \lambda_{yx} {x_{\mathrm{i}+1,\mathrm{i}}}^{(0)} + \lambda_{yy} {y_{\mathrm{i}+1,\mathrm{i}}}^{(0)}, \tag{C.21}$$

where we use $\mathbf{r}_{\mathrm{i}+1,1} = \mathbf{r}_{\mathrm{i}+1} - \mathbf{r}_\mathrm{i}$, assuming the vertices ordered clockwise. The terms $M_c^{(1)}$ and $M_c^{(2)}$ are given by

$$M_c^{(1)} = \sum_{\mathrm{i}=1}^{6} \frac{1}{P_{c_\mathrm{i}}^{(1)}} \left[\alpha_\mathrm{i}^2 u_{xx} + \beta_\mathrm{i}^2 u_{yy} + \alpha_\mathrm{i}\beta_\mathrm{i}\left(u_{xy} + u_{yx}\right)\right], \tag{C.22}$$

$$\begin{aligned} M_c^{(2)} = \sum_{\mathrm{i}=1}^{6} \frac{1}{P_{c_\mathrm{i}}^{(1)}} \Bigg[& u_{xx}^2 \left(\frac{\alpha_\mathrm{i}^2}{2} - \frac{\alpha_\mathrm{i}^4}{2P_{c_\mathrm{i}}^{(1)^2}}\right) + u_{yy}^2 \left(\frac{\beta_\mathrm{i}^2}{2} - \frac{\beta_\mathrm{i}^4}{2P_{c_\mathrm{i}}^{(1)^2}}\right) \\ & + u_{xy}^2 \left(\frac{\beta_\mathrm{i}^2}{2} - \frac{\alpha_\mathrm{i}^2\beta_\mathrm{i}^2}{2P_{c_\mathrm{i}}^{(1)^2}}\right) + u_{yx}^2 \left(\frac{\alpha_\mathrm{i}^2}{2} - \frac{\alpha_\mathrm{i}^2\beta_\mathrm{i}^2}{2P_{c_\mathrm{i}}^{(1)^2}}\right) \\ & + u_{xx}u_{xy} \left(\alpha_\mathrm{i}\beta_\mathrm{i} - \frac{\alpha_\mathrm{i}^3\beta_\mathrm{i}}{P_{c_\mathrm{i}}^{(1)^2}}\right) + u_{yy}u_{yx} \left(\alpha_\mathrm{i}\beta_\mathrm{i} - \frac{\alpha_\mathrm{i}\beta_\mathrm{i}^3}{P_{c_\mathrm{i}}^{(1)^2}}\right) \\ & + u_{xx}u_{yx} \left(-\frac{\alpha_\mathrm{i}^3\beta_\mathrm{i}}{P_{c_\mathrm{i}}^{(1)^2}}\right) + u_{yy}u_{xy} \left(-\frac{\alpha_\mathrm{i}^3\beta_\mathrm{i}}{P_{c_\mathrm{i}}^{(1)^2}}\right) \\ & + u_{xx}u_{yy} \left(-\frac{\alpha_\mathrm{i}^2\beta_\mathrm{i}^2}{P_{c_\mathrm{i}}^{(1)^2}}\right) + u_{xy}u_{yx} \left(-\frac{\alpha_\mathrm{i}^2\beta_\mathrm{i}^2}{P_{c_\mathrm{i}}^{(1)^2}}\right)\Bigg]. \end{aligned} \tag{C.23}$$

Now, following a similar procedure as in the previous section we can compute all the

energy contributions. The contribution proportional to K_A is

$$\begin{aligned} E_A &= \sum_c \frac{K_A}{2} \left(A_c^{(2)} - A_{0c}\right)^2, \\ &= \sum_c \frac{K_A}{2} A_{0c}^2 \left[\left(1 + \varepsilon \mathrm{tr}\left(U\right) + \varepsilon^2 \mathrm{det}\left(U\right)\right) \det\left(\Lambda\right) - 1\right]^2, \\ &= \sum_c \frac{K_A}{2} A_{0c}^2 \left[\det\left(\Lambda\right) - 1 + \left(\varepsilon \mathrm{tr}\left(U\right) + \varepsilon^2 \mathrm{det}\left(U\right)\right) \det\left(\Lambda\right)\right]^2, \end{aligned} \tag{C.24}$$

where we obtain that the zeroth, first, and second order terms of E_A are given by

$$E_A^{(0)} = \sum_c \frac{K_A}{2} A_{0c}^2 \left(\det\left(\Lambda\right) - 1\right)^2, \tag{C.25}$$

$$E_A^{(1)} = \sum_c K_A A_{0c}^2 \mathrm{det}\left(\Lambda\right) \left[\det\left(\Lambda\right) - 1\right] \mathrm{tr}\left(U\right), \tag{C.26}$$

$$E_A^{(2)} = \sum_c \frac{K_A}{2} A_{0c}^2 \left[\det\left(\Lambda\right)^2 \mathrm{tr}\left(U\right)^2 + 2\mathrm{det}\left(\Lambda\right) \left(\det\left(\Lambda\right) - 1\right) \det\left(U\right)\right]. \tag{C.27}$$

Similarly, for the term proportional to K_P,

$$\begin{aligned} E_P &= \sum_c \frac{K_P}{2} \left(P_c^{(2)} - P_{0c}\right)^2, \\ &= \sum_c \frac{K_P}{2} \left(P_c^{(1)} - P_{0c} + \varepsilon M_c^{(1)} + \varepsilon^2 M_c^{(2)}\right)^2, \end{aligned} \tag{C.28}$$

and the zeroth, first, and second order terms of E_P are given by

$$E_P^{(0)} = \sum_c \frac{K_P}{2} \left(P_c^{(1)} - P_{0c}\right)^2, \tag{C.29}$$

$$E_P^{(1)} = \sum_c K_P \left(P_c^{(1)} - P_{0c}\right) M_c^{(1)}, \tag{C.30}$$

$$E_P^{(2)} = \sum_c \frac{K_P}{2} \left[2 \left(P_c^{(1)} - P_{0c}\right) M_c^{(2)} + {M_c^{(1)}}^2\right]. \tag{C.31}$$

Finally, the zeroth, first, and second order terms of E_J are

$$E_J^{(0)} = \sum_c \frac{J}{2} P_c^{(1)}, \qquad E_J^{(1)} = \sum_c \frac{J}{2} M_c^{(1)}, \qquad E_J^{(2)} = \sum_c \frac{J}{2} M_c^{(2)}. \tag{C.32}$$

Appendix D

Vertex model: Isolated active hexagonal cell

We consider a single regular hexagonal cells of side a, for which the preferred and initial cell area and perimeter are $A_{\rm i} = A_0 = 3\sqrt{3}a^2/2$ and $P_{\rm i} = P_0 = 6a$, respectively. Activity is included as modifications of the target parameters, $A_0 \to (1-\lambda_A)\,A_0$ and $P_0 \to (1-\lambda_P)\,P_0$, with $\lambda_A, \lambda_P \in [0,1]$. By using the energy functional of the vertex model, Eq. (A.1), we get an initial value of the energy

$$E_{\rm i} = \frac{1}{2}K_A\lambda_A^2 A_0^2 + \frac{1}{2}K_P\lambda_P^2 P_0^2 + \frac{1}{2}JP_0, \tag{D.1}$$

where we have kept the adhesion term (half of it, inspired in Eq. (A.16)) even when we are considering an isolated cell to allow the system to have equilibrium perimeter values different from P_0.

Later, we allow the cell to deform, such that new vertex positions are given by $(I+U)\,\mathbf{r}_{\rm i}^{[0]}$, where U is a general 2×2 matrix of components $u_{{\rm i}k}$, and $\mathbf{r}_{\rm i}^{[0]}$ are the position of the vertices of the regular hexagon. We can write U as a linear combination:

$$U = \sum_{\rm i=1}^{4} v_{\rm i} U_{\rm i}, \tag{D.2}$$

where $U_{\rm i}$ correspond to one of the four deformation modes

$$U_1 = \frac{1}{\sqrt{2}}\begin{pmatrix} -1 & 0 \\ 0 & 1 \end{pmatrix}\text{[deviatoric]}, \qquad U_2 = \frac{1}{\sqrt{2}}\begin{pmatrix} 0 & 1 \\ 1 & 0 \end{pmatrix}\text{[pure shear]}, \tag{D.3}$$

$$U_3 = \frac{1}{\sqrt{2}}\begin{pmatrix} 0 & -1 \\ 1 & 0 \end{pmatrix}\text{[rotation]}, \qquad U_4 = \frac{1}{\sqrt{2}}\begin{pmatrix} -1 & 0 \\ 0 & -1 \end{pmatrix}\text{[contraction]},$$

and v_{i} are the amplitudes.

With these considerations, the new area and perimeter of the cell are given by

$$A_f = \frac{3\sqrt{3}a^2}{4}\left(2 - v_1^2 - v_2^2 + v_3^2 - 2\sqrt{2}v_4 + v_4^2\right), \tag{D.4}$$

$$\begin{aligned} P_f = {} & \frac{a}{2}\left(\sqrt{\left(2 - \sqrt{2}\left[v_1 + v_4\right] - \sqrt{6}\left[v_2 - v_3\right]\right)^2 + \left(2\sqrt{3} - \sqrt{2}\left[v_2 + v_3\right] - \sqrt{6}\left[v_4 - v_1\right]\right)^2}\right) \\ & + \frac{a}{2}\left(\sqrt{\left(2 - \sqrt{2}\left[v_1 + v_4\right] - \sqrt{6}\left[v_3 - v_2\right]\right)^2 + \left(2\sqrt{3} + \sqrt{2}\left[v_2 + v_3\right] - \sqrt{6}\left[v_4 - v_1\right]\right)^2}\right) \\ & + \sqrt{2}a\sqrt{2 - 2\sqrt{2}\left(v_1 + v_4\right) + \left(v_1 + v_4\right)^2 + \left(v_2 + v_3\right)^2}. \end{aligned} \tag{D.5}$$

A final energy, considering the deformed cellular shape, can be computed as

$$\begin{aligned} E_f &= \frac{1}{2}K_A\left(A_f - A_0\left[1 - \lambda_A\right]\right)^2 + \frac{1}{2}K_P\left(P_f - P_0\left[1 - \lambda_P\right]\right)^2 + \frac{1}{2}JP_f \\ &= \frac{1}{2}K_A\left(\left[A_f - A_0\right] + A_0\lambda_A\right)^2 + \frac{1}{2}K_P\left(\left[P_f - P_0\right] + P_0\lambda_P\right)^2 + \frac{1}{2}JP_f \\ &= \frac{1}{2}K_A\left(A_f - A_0\right)^2 + K_A\left(A_f - A_0\right)A_0\lambda_A + \frac{1}{2}K_P\left(P_f - P_0\right)^2 + K_P\left(P_f - P_0\right)P_0\lambda_P \end{aligned} \tag{D.6}$$

$$+ E_{\mathrm{i}} + \frac{1}{2}J\left(P_f - P_0\right). \tag{D.7}$$

The variation of the energy can be written as $\Delta E = E_f - E_{\mathrm{i}}$,

$$\begin{aligned} \Delta E = {} & \frac{1}{2}K_A\left(A_f - A_0\right)^2 + \frac{1}{2}K_P\left(P_f - P_0\right)^2 + \frac{1}{2}J\left(P_f - P_0\right) \\ & + K_A\left(A_f - A_0\right)A_0\lambda_A + K_P\left(P_f - P_0\right)P_0\lambda_P. \end{aligned} \tag{D.8}$$

The right hand side of Eq. (D.8) is a function of the amplitudes v_{i}, with $\mathrm{i} = \{1, 2, 3, 4\}$, and then can be written as $\Delta E = \hat{E}\mathrm{e}\left(v_1, v_2, v_4, v_3\right)$, with $\hat{E} = K_A A_0^2/2$, as shown in the following

$$\Delta E = \frac{1}{2}K_A A_0^2 \left[\left(\frac{A_f}{A_0} - 1 \right)^2 + \frac{K_P P_0^2}{K_A A_0^2} \left(\frac{P_f}{P_0} - 1 \right)^2 + \frac{J P_0}{K_A A_0^2} \left(\frac{P_f}{P_0} - 1 \right) \right] + \frac{1}{2}K_A A_0^2 \left[2 \left(\frac{A_f}{A_0} - 1 \right) \lambda_A + \frac{2K_P P_0^2}{K_A A_0^2} \left(\frac{P_f}{P_0} - 1 \right) \lambda_P \right] \tag{D.9}$$

Using that $A_0 = 3\sqrt{3}a^2/2$ and $P_0 = 6a$,

$$P_0/A_0^2 = 8/(9a^3), \tag{D.10}$$
$$P_0^2/A_0^2 = 16/(3a^2), \tag{D.11}$$

and the definition of the dimensionless parameters $p = K_P/(a^2 K_A)$ and $j = J/(a^3 K_A)$, we have

$$\Delta E = \hat{E} \left[\left(\frac{A_f}{A_0} - 1 \right)^2 + \frac{16}{3} p \left(\frac{P_f}{P_0} - 1 \right)^2 + \frac{8}{9} j \left(\frac{P_f}{P_0} - 1 \right) \right] + \hat{E} \left[2 \left(\frac{A_f}{A_0} - 1 \right) \lambda_A + \frac{32}{3} p \left(\frac{P_f}{P_0} - 1 \right) \lambda_P \right]. \tag{D.12}$$

Finally, the function e that we minimize in the main text is given by

$$\mathrm{e} = \left(\frac{A_f}{A_0} - 1 \right)^2 + \frac{16}{3} p \left(\frac{P_f}{P_0} - 1 \right)^2 + \frac{8}{9} j \left(\frac{P_f}{P_0} - 1 \right) + 2 \left(\frac{A_f}{A_0} - 1 \right) \lambda_A + \frac{32}{3} p \left(\frac{P_f}{P_0} - 1 \right) \lambda_P, \tag{D.13}$$

with A_f and P_f given by Eqs. (D.4) and (D.5).

We can separate e as the sum of three terms,

$$\mathrm{e}_A = 2\lambda_A \left(\frac{A_f}{A_0} - 1 \right) + \left(\frac{A_f}{A_0} - 1 \right)^2, \tag{D.14}$$
$$\mathrm{e}_P = \frac{32}{3} p \lambda_P \left(\frac{P_f}{P_0} - 1 \right) + \frac{16}{3} p \left(\frac{P_f}{P_0} - 1 \right)^2, \tag{D.15}$$
$$\mathrm{e}_J = \frac{8}{9} j \left(\frac{P_f}{P_0} - 1 \right), \tag{D.16}$$

where e_A and e_P have an active and a passive term. We can see that there will be a competition between medial, perimeter, and adhesion terms to reach the final cellular shape. The three components act with similar order of energy when $1 \sim j \sim 10p$ ($j \sim 1$ and $p \sim 0.1$).

We choose to use $p \in [0.01, 1]$ and $j \in [0.01, 1]$ (in logarithmic scales), such that the effect of the adhesion is never dominant (to avoid instabilities of the energy functional). In the region $j \in [0.01, 0.1]$ the medial terms dominate and in $j \in [0.1, 1]$ the perimeter terms dominate.

Appendix E

Vertex active model: Linear order equations of motion

Considering a tissue that obeys periodic boundary conditions, formed by cells with preferred areas and perimeters given by A_{0c} and P_{0c}, respectively, and with the position of the vertices $\mathbf{r}_{\mathrm{i}}^{[0]}$ initially in an equilibrium configuration (and $A_c^{[0]}$ and $P_c^{[0]}$ the initial area and perimeter, respectively), we study the linear order equation of the vertices forming the system when assuming that the equilibrium parameters changes as $A_{0c} \to A_{0c}+\varepsilon A_{1c}$ and $P_{0c} \to P_{0c}+\varepsilon P_{1c}$, and hence the positions get modified as $\mathbf{r}_{\mathrm{i}}^{[0]} + \varepsilon \mathbf{u}_{\mathrm{i}}$ with $\mathbf{u}_{\mathrm{i}}$ characterizing the displacement of the vertex i. We write the equation of motions derivated from the vertex model (Eqs. (A.13), (A.14) and (A.15)) at $O(\varepsilon)$. Since the initial configuration is an equilibrium one, the zeroth order is cancelled automatically.

In the following calculations the ε will not be included, for simplicity.

Starting from the second line in Eq. (A.4), taking $1 \to \mathrm{i}$, and considering $\mathbf{u}_{\mathrm{i}} = v_{\mathrm{i}}\hat{\mathbf{x}}+w_{\mathrm{i}}\hat{\mathbf{y}}$,we write the area of the c cell up to first order in the displacements,

$$
\begin{aligned}
A_c =& -\sum_{j=2}^{N-1} \frac{1}{2}\hat{\mathbf{z}} \cdot \left[(\mathbf{r}_j - \mathbf{r}_{\mathrm{i}}) \times (\mathbf{r}_{j+1} - \mathbf{r}_{\mathrm{i}})\right], \\
=& -\sum_{j=2}^{N-1} \frac{1}{2}\hat{\mathbf{z}} \cdot \left[\left(\mathbf{r}_{j,\mathrm{i}}^{[0]} + \mathbf{u}_{j,\mathrm{i}}\right) \times \left(\mathbf{r}_{j+1,\mathrm{i}}^{[0]} + \mathbf{u}_{j+1,\mathrm{i}}\right)\right] \\
=& A_c^{[0]} - \sum_{j=2}^{N-1} \frac{1}{2}\hat{\mathbf{z}} \cdot \left[\mathbf{r}_{j,\mathrm{i}}^{[0]} \times \mathbf{u}_{j+1,\mathrm{i}} + \mathbf{u}_{j,\mathrm{i}} \times \mathbf{r}_{j+1,\mathrm{i}}^{[0]}\right] \\
=& A_c^{[0]} - \sum_{j=2}^{N-1} \frac{1}{2}\left[x_{j,\mathrm{i}}^{[0]} w_{j+1,\mathrm{i}} - y_{j,\mathrm{i}}^{[0]} v_{j+1,\mathrm{i}} + v_{j,\mathrm{i}} y_{j+1,\mathrm{i}}^{[0]} - w_{j,\mathrm{i}} x_{j+1,\mathrm{i}}^{[0]}\right] \\
=& A_c^{[0]} - \sum_{j=2}^{N-1} \frac{1}{2}\left[-v_{\mathrm{i}} y_{j+1,j}^{[0]} + w_{\mathrm{i}} x_{j+1,j}^{[0]} + v_j y_{j+1,\mathrm{i}}^{[0]} - v_{j+1} y_{j,\mathrm{i}}^{[0]} - w_j x_{j+1,\mathrm{i}}^{[0]} + w_{j+1} x_{j,\mathrm{i}}^{[0]}\right]. \qquad \text{(E.1)}
\end{aligned}
$$

On the other hand, the Eq. (A.7) is now given

$$\begin{aligned}\nabla_{\mathrm{i}} A_c =& \frac{1}{2}\left[\mathbf{r}^{[0]}_{\mathrm{i}-1,\mathrm{i}+1} + \mathbf{u}_{\mathrm{i}-1,\mathrm{i}+1}\right] \times \hat{\mathbf{z}} \\ =& \frac{1}{2}\left[y^{[0]}_{\mathrm{i}-1,\mathrm{i}+1} + w_{\mathrm{i}-1,\mathrm{i}+1}\right]\hat{\mathbf{x}} - \frac{1}{2}\left[x^{[0]}_{\mathrm{i}-1,\mathrm{i}+1} + v_{\mathrm{i}-1,\mathrm{i}+1}\right]\hat{\mathbf{y}}. \end{aligned} \tag{E.2}$$

Finally, the equation of motion proportional to K_A at $O(\varepsilon)$ is given by

$$\begin{aligned}\frac{\mathrm{d}\mathbf{r}_{\mathrm{i}}}{\mathrm{d}t}^{(A)} =& -\sum_c K_A \left(A_c - A_{0c} - A_{1c}\right)\nabla_{\mathrm{i}} A_c, \\ =& -\sum_c K_A \left(A_c - A_{0c}\right)\nabla_{\mathrm{i}} A_c + \sum_c K_A A_{1c} \nabla_{\mathrm{i}} A_c, \\ =& -\sum_c \frac{K_A}{2}\left(A^{[0]}_c - A_{0c}\right)\left[\left(w_{\mathrm{i}-1} - w_{\mathrm{i}+1}\right)\hat{\mathbf{x}} - \left(v_{\mathrm{i}-1} - v_{\mathrm{i}+1}\right)\hat{\mathbf{y}}\right] \\ & -\sum_c \frac{K_A}{4}\sum_{j=2}^{N-1}\left[v_{\mathrm{i}} y^{[0]}_{j+1,j} - w_{\mathrm{i}} x^{[0]}_{j+1,j} - v_j y^{[0]}_{j+1,\mathrm{i}} + v_{j+1} y^{[0]}_{j,\mathrm{i}} + w_j x^{[0]}_{j+1,\mathrm{i}} - w_{j+1} x^{[0]}_{j,\mathrm{i}}\right] \\ & \left[y^{[0]}_{\mathrm{i}-1,\mathrm{i}+1}\hat{\mathbf{x}} - x^{[0]}_{\mathrm{i}-1,\mathrm{i}+1}\hat{\mathbf{y}}\right] + \sum_c \frac{K_A}{2} A_{1c}\left[y^{[0]}_{\mathrm{i}-1,\mathrm{i}+1}\hat{\mathbf{x}} - x^{[0]}_{\mathrm{i}-1,\mathrm{i}+1}\hat{\mathbf{y}}\right]. \end{aligned} \tag{E.3}$$

Now, let's see from Eq. (A.8) how the perimeter of the cell c changes,

$$\begin{aligned} P_c =& \sum_{j=1}^{N} |\mathbf{r}_{j+1,j}| = \sum_{j=1}^{N} |\mathbf{r}^{[0]}_{j+1,j} + \mathbf{u}_{j+1,j}|, \\ =& \sum_{j=1}^{N} \sqrt{\left(x^{[0]}_{j+1,j} + v_{j+1,j}\right)^2 + \left(y^{[0]}_{j+1,j} + w_{j+1,j}\right)^2}, \\ =& \sum_{j=1}^{N} \sqrt{{r^{[0]}_{j+1,j}}^2 + 2x^{[0]}_{j+1,j} v_{j+1,j} + 2y^{[0]}_{j+1,j} w_{j+1,j} + {v_{j+1,j}}^2 + {w_{j+1,j}}^2}, \\ =& \sum_{j=1}^{N} r^{[0]}_{j+1,j}\left(1 + \frac{x^{[0]}_{j+1,j} v_{j+1,j}}{{r^{[0]}_{j+1,j}}^2} + \frac{y^{[0]}_{j+1,j} w_{j+1,j}}{{r^{[0]}_{j+1,j}}^2}\right), \\ =& P^{[0]}_c + \sum_{j=1}^{N}\left(\frac{x^{[0]}_{j+1,j} v_{j+1,j}}{r^{[0]}_{j+1,j}} + \frac{y^{[0]}_{j+1,j} w_{j+1,j}}{r^{[0]}_{j+1,j}}\right), \\ =& P^{[0]}_c + \sum_{j=1}^{N}\left(-v_j\left[\frac{x^{[0]}_{j+1,j}}{r^{[0]}_{j+1,j}} + \frac{x^{[0]}_{j-1,j}}{r^{[0]}_{j-1,j}}\right] - w_j\left[\frac{y^{[0]}_{j+1,j}}{r^{[0]}_{j+1,j}} + \frac{y^{[0]}_{j-1,j}}{r^{[0]}_{j-1,j}}\right]\right). \end{aligned} \tag{E.4}$$

The gradient of the perimeter, Eq. (A.9), is be given by

$$\begin{aligned}\nabla_{\mathrm{i}} P_c &= -\left(\frac{\mathbf{r}^{[0]}_{\mathrm{i+1,i}}}{r^{[0]}_{\mathrm{i+1,i}}} + \frac{\mathbf{r}^{[0]}_{\mathrm{i-1,i}}}{r^{[0]}_{\mathrm{i-1,i}}}\right) - \left(\frac{\mathbf{u}_{\mathrm{i+1,i}}}{r^{[0]}_{\mathrm{i+1,i}}} + \frac{\mathbf{u}_{\mathrm{i-1,i}}}{r^{[0]}_{\mathrm{i-1,i}}}\right) \\ &= -\left(\frac{\mathbf{r}^{[0]}_{\mathrm{i+1,i}}}{r^{[0]}_{\mathrm{i+1,i}}} + \frac{\mathbf{r}^{[0]}_{\mathrm{i-1,i}}}{r^{[0]}_{\mathrm{i-1,i}}}\right) + \mathbf{u}_{\mathrm{i}}\left(\frac{1}{r^{[0]}_{\mathrm{i+1,i}}} + \frac{1}{r^{[0]}_{\mathrm{i-1,i}}}\right) - \mathbf{u}_{\mathrm{i-1}}\frac{1}{r^{[0]}_{\mathrm{i-1,i}}} - \mathbf{u}_{\mathrm{i+1}}\frac{1}{r^{[0]}_{\mathrm{i+1,i}}} \end{aligned} \tag{E.5}$$

Hence, the equation of motion proportional to K_P at $O(\varepsilon)$ is given by

$$\begin{aligned}\frac{\mathrm{d}\mathbf{r}_{\mathrm{i}}}{\mathrm{d}t}^{(P)} &= -\sum_c K_P\left(P_c - P_{0c} - P_{1c}\right)\nabla_{\mathrm{i}} P_c, \\ &= -\sum_c K_P\left(P_c - P_{0c}\right)\nabla_{\mathrm{i}} P_c + \sum_c K_P P_{1c}\nabla_{\mathrm{i}} P_c, \\ &= \sum_c K_P\left(P^{[0]}_c - P_{0c}\right)\left(-\mathbf{u}_{\mathrm{i}}\left[\frac{1}{r^{[0]}_{\mathrm{i+1,i}}} + \frac{1}{r^{[0]}_{\mathrm{i-1,i}}}\right] + \mathbf{u}_{\mathrm{i-1}}\frac{1}{r^{[0]}_{\mathrm{i-1,i}}} + \mathbf{u}_{\mathrm{i+1}}\frac{1}{r^{[0]}_{\mathrm{i+1,i}}}\right) \\ &+ \sum_c\sum_{j=1}^{N} -\left(v_j\left[\frac{x^{[0]}_{j+1,j}}{r^{[0]}_{j+1,j}} + \frac{x^{[0]}_{j-1,j}}{r^{[0]}_{j-1,j}}\right] + w_j\left[\frac{y^{[0]}_{j+1,j}}{r^{[0]}_{j+1,j}} + \frac{y^{[0]}_{j-1,j}}{r^{[0]}_{j-1,j}}\right]\right)\left(\frac{\mathbf{r}^{[0]}_{\mathrm{i+1,i}}}{r^{[0]}_{\mathrm{i+1,i}}} + \frac{\mathbf{r}^{[0]}_{\mathrm{i-1,i}}}{r^{[0]}_{\mathrm{i-1,i}}}\right) \\ &- \sum_c K_P P_{1c}\left(\frac{\mathbf{r}^{[0]}_{\mathrm{i+1,i}}}{r^{[0]}_{\mathrm{i+1,i}}} + \frac{\mathbf{r}^{[0]}_{\mathrm{i-1,i}}}{r^{[0]}_{\mathrm{i-1,i}}}\right). \end{aligned} \tag{E.6}$$

Similarly, the force proportional to J, in a system that obeys periodic boundary conditions Eq. (A.16), at $O(\varepsilon)$ is given by,

$$\begin{aligned}\frac{\mathrm{d}\mathbf{r}_{\mathrm{i}}}{\mathrm{d}t}^{(J)} &= -\sum_c \frac{J}{2}\nabla_{\mathrm{i}} P_c, \\ &= \sum_c \frac{J}{2}\left(-\mathbf{u}_{\mathrm{i}}\left[\frac{1}{r^{[0]}_{\mathrm{i+1,i}}} + \frac{1}{r^{[0]}_{\mathrm{i-1,i}}}\right] + \mathbf{u}_{\mathrm{i-1}}\frac{1}{r^{[0]}_{\mathrm{i-1,i}}} + \mathbf{u}_{\mathrm{i+1}}\frac{1}{r^{[0]}_{\mathrm{i+1,i}}}\right). \end{aligned} \tag{E.7}$$